國 立 交 通 大 學

光 電 工 程 研 究 所

博 士 論 文

高效率近紫外光發光二極體元件製作

Fabrication of High Efficiency Near-Ultraviolet

Light Emitting Devices

研 究 生：涂博閔　　Student：Po-Min Tu

指導教授：張俊彥 教授　　Advisor：Prof. Chun-Yen Chang

冉曉雯 教授　　Prof. Hsiao-Wen Zan

中 華 民 國 一 百 零 一 年 六 月

高效率近紫外光發光二極體元件製作

Fabrication of High Efficiency Near-Ultraviolet Light Emitting Devices

研　究　生：涂博閔　　　Student：Po-Min Tu

指導教授：張俊彥　教授　　　Advisor：Prof. Chun-Yen Chang

冉曉雯　教授　　　Prof. Hsiao-Wen Zan

國立交通大學

光電工程研究所

博士論文

A dissertation

Submitted to Institute of Electro-Optical Engineering

College of Electrical Engineering and Computer Science

National Chiao-Tung University

in Partial Fulfillment of the Requirements

for the Degree of

Doctor of Philosophy

in

Electro-Optical Engineering

June 2012

Hsinchu, Taiwan, Republic of China

中華民國一百零一年六月

高效率近紫外光發光二極體元件製作

研究生：凃博閔　　　　　　　　　　指導教授: 張俊彥 教授

冉曉雯 教授

國立交通大學光電工程研究所

摘要

近年來，由於氮化鎵近紫外光發光二極體(near-UV LED)具有非常大的發展潛力及廣泛應用，如驗鈔、光觸媒除臭、空氣淨化器等紫外光光源的使用，因此越來越多的團隊開始研究高效率元件的製作及使用近紫外光於固態照明與螢光粉轉換光源之應用。

然而，低銦含量下的發光二極體其內部量子效率(IQE)驟降迅速，晶格品質與氮化鎵自我吸收的問題更導致製作高效率近紫外光發光二極體是相當困難的。文獻指出低銦含量氮化銦鎵(InGaN)量子井設計中，使用氮化鋁鎵(AlGaN)的位障來提高載子局限能力是必須的；但由於此兩材料氮化銦鎵(InGaN)及氮化鋁鎵(AlGaN)最佳化的成長溫度大不相同，因此深深的影響了兩者的晶格品質及其元件效率的表現。

此外，由於相對低價格及高品質的優點，藍寶石(Sapphire)是目前最廣泛使用於氮化鎵材料的磊晶基板，但由於其導電性及導熱性差的特性致使元件的表現及設計處處受限。近年來，許多研究團隊致力於發展雷射剝離 laser lift-off (LLO)技術，及使用氮化鉻(CrN)、氧化鋅(ZnO)及矽摻雜氮化鎵(Si:GaN)等犧牲層來實現化學剝離 chemical lift-off (CLO)技術，來實現獨立的氮化鎵薄膜及垂直式發光二極體元件製作，以提升更高的光電元件品質與效率。然而，高溫的雷射剝離製程將導致氮化鎵/藍寶石(GaN/sapphire)界面及保護層因熱衝擊而受損，進而造成元件漏電及低良率等問題；化學剝離製程雖然能避免雷射

瞬間高溫加熱元件造成傷害，卻也造成後續蝕刻傷害及使用犧牲層造成晶格品質的問題。

本論文中，我們利用氮化鋁鎵銦(InAlGaN)來取代原本的氮化鋁鎵(AlGaN)的位障以實現高效率的近紫外光發光二極體，並開發一種使用倒六角錐結構 Hexagonal Inversed Pyramid (HIP)來實現機械式剝離 mechanical lift-off (MLO)製程以製作高品質氮化鎵垂直式發光二極體(Vertical-LED)，此外效率驟降的物理意義、剝離的機制及其光電特性分析也將與本論文中有詳細的量測及調查。

首先，我們調查量子井中以氮化鋁鎵(AlGaN)及氮化鋁鎵銦(InAlGaN)為位障之氮化銦鎵(InGaN)近紫外光發光二極體效率驟降的表現，電致發光(Electroluminescence)結果顯示使用四元化合物材料(quaternary)的 LED 發光強度於 350 mA 及 1000 mA 電流操作下分別提升了 25 %及 55 %，更進一步的物理模擬顯示使用四元化合物材料的 LED 於高電流注入下提升了 62 %的輻射再結合率及 13 %較少的效率驟降，推測這些改善來自於載仔濃度的提升及載仔更均勻的重新分佈。

再者，我們使用倒六角錐結構來實現機械式剝離製程以製作高品質氮化鎵垂直式發光二極體，倒六角錐結構的製作採用高溫氫氧化鉀(KOH)濕蝕刻其氮化鎵/藍寶石基板的界面來完成，TEM 分析結果顯示平均的線缺陷密度估計從 2×10^{9} 降低至 1×10^{8} cm^{-2}，拉曼(Raman)光譜也揭露出使用倒六角錐結構的氮化鎵磊晶層之壓應力能有效的被釋放，最後我們成功的使用倒六角錐結構為犧牲層並於晶片鍵合降溫過程中實現了機械式剝離製程，其中剝離的物理機制、材料及元件的光電特性也將於本論文中詳細探討。

Fabrication of High Efficiency Near-Ultraviolet Light Emitting Devices

Student : Po-Min Tu　　Advisor : Prof. Chun-Yen Chang

Prof. Hsiao-Wen Zan

Department of photonics & Institute of Electro-Optical Engineering

National Chiao-Tung University

Abstract

GaN-based near-ultraviolet light emitting devices (LEDs) have attracted great attention in last few years due to its potential applications in photo-catalytic deodorizing such as air conditioner, and there have been interests in solid-state lighting by using near-UV LEDs light for the phosphor-converting source. However, it is difficult to fabricate near-UV LEDs with high efficiency, because the internal quantum efficiency (IQE) decreases drastically under the low indium composition.

Moreover, crystalline quality and light absorption of GaN are significant for short wavelength near-UV LEDs. It's well known that in low indium content InGaN QWs, AlGaN barrier is necessary for carrier confinement. But the two materials of AlGaN and InGaN are very different in growth temperature which affects strongly on the quality of material and device performances.

In addition, the sapphire is the most commonly used substrate because of its relative low cost, but it also limits the devices performance due to its poor electrical and thermal conductivity. During the last decade of years, the techniques of laser lift-off (LLO) and chemical lift-off (CLO) which use CrN layer, ZnO layer, and Si-doped n-GaN layer as the sacrificial layer have been adopted to fabricate the freestanding GaN membrane and the vertical LEDs (V-LEDs) for the purpose of high performance optoelectronic devices.

However, the LLO process may induce some possible damages under high temperature in the GaN/sapphire interface. And even though the CLO can prevent the GaN layer from the laser damage during the laser lift-off process, but it also makes another chemical etching damages and reduce the crystal quality. Hence, we study the fabrication of mechanical lift-off (MLO) for high quality GaN-based V-LEDs with Hexagonal Inversed Pyramid (HIP) structures.

In this study, we demonstrate high efficient near-UV LEDs by replacing AlGaN by InAlGaN barrier in active region and mechanical lift-off technology. Furthermore, the efficiency droop characteristics, theoretical analysis of lift-off process, and optoelectronic properties of high efficient near-UV LEDs have been measured and investigated.

First, the efficiency droop in InGaN-based near-UV LED with AlGaN and InAlGaN barrier is investigated. Electroluminescence results indicate that the light performance of quaternary LEDs can be enhanced by 25 % and 55 % at 350 mA and 1000mA, respectively. Furthermore, simulations show that quaternary LEDs exhibit 62 % higher radiative recombination rate and low efficiency degradation of 13 % at a high injection current. We attribute this improvement to increasing of carrier concentration and more uniform redistribution of carriers.

Second, we report the fabrication of mechanical lift-off high quality GaN-based V-LED with HIP structures. The HIP GaN/air/Sapphire structures were formed at the GaN/sapphire substrate interface under high temperature during KOH wet etching process. The average threading dislocation density (TDD) was estimated by transmission electron microscopy (TEM) and found the reduction about one order. Raman spectroscopy revealed that the compressive stress of GaN epilayer was effectively relieved in the GaN-based LED with HIP structures. Finally, the mechanical lift-off process is claimed to be successful by using the HIP structures as a sacrificial layer during wafer bonding process. Furthermore, theoretical analysis of lift-off process, and optoelectronic properties of devices have been investigated.

誌謝

時光荏苒,一轉眼我在交大已經過了四年多的研究生活,終於畢業這一刻即將來臨，穿上博士畢業服那一刻，心情頓時百感交集。

首先，我要感謝張俊彥校長和冉曉雯教授的細心指導，謝謝老師提供了很好的研究環境與機會，總是在我最無助的時候給了我一股正向的力量，讓我勇敢往前進，持續做對的事情。謝謝冉老師給予我研究上最大的空間與自由度，並感謝張校長帶著我走過人生中最精彩的每一刻，重新賦予我生命的彩度。

研究生涯中，我遇到了許多的貴人：感謝楊宗熺博士的鼓勵與支持，讓我有機會完成博士學位;感謝郭浩中老師無私奉獻所學及研究資源全力相挺,讓我的研究非常順利，這一切我會銘記在心；感謝程育人老師教導我嚴謹的研究態度，還有善解人意與追根究柢的精神讓人深感佩服；感謝林建中老師細心指導，並且不厭其煩的修改論文與研究方向；感謝盧廷昌老師在研究中給予正確的研究方向與實驗靈感。

更要謝謝實驗室曾經幫助我的同學及學弟妹:感謝張哲榮同學從資格考開始一路陪著我成長、漫漫長夜的討論與促膝長談至今仍然懷念，你對實驗室的付出與關懷，讓我代表全實驗室說聲“謝謝”；感謝張世邦同學一句話情義相挺至今,犧牲奉獻陪著大家一起努力做好研究；感謝凱麟、祐誠、昀瑾、婉儀、祥修、國斌、盈臻、小杜、芝羽、柏君、江耀、博文，我的博士研究生涯因為有你們而變得豐富寬廣。還要感謝邱鏡學同學，總是陪我一起熬夜考試、趕做報告、研究討論，幫我扛了很多繁雜的工作…這個博士學位應當分你一半；還有李鎮宇博士、羅明華博士、陳士偉博士、李金釵博士、邱清華博士、陳振昌博士、黃延儀博士、許世杰博士、江松柏、宋兆峯、洪誌彰、黃彥棠，與你們一起研究的生活真的很精彩。

還要感謝榮創能源(股)公司：徐智鵬副總於實驗上的支持及給予的自由度，讓我無

後顧之憂能全心投入做研究；感謝黃世晟處長嚴謹與細心的教導，並將畢生磊晶的功力傳授給我，在此說聲“謝謝師父”；感謝每一位同事及同學在我攻讀博士期間能體諒與支持，謝謝順貴、梓健、佳輝、雅雯、鈺如、嘉宏、雅文、宜庭、美玲、亞琦、振安、凌帆、穎超、芃逸、文禹、馬哥、宗民、慶昌、范文郎博士、范文忠博士、陳永翔博士；還要感謝前輩照顧:詹世雄博士、曾堅信博士、張忠民博士、孫健仁博士、謝于誠副總。

另外，也感謝口試期間給予細心指導的蘇炎坤校長、張翼教授、張守進教授、黃建璋教授，這些寶貴的建議將使本論文更加完整。

最後，感謝我的家人：阿嬤、父母、姐姐、姑姑，因為有你們精神上的支持，讓我能全心全力的完成博士學位，真的很感謝你們。另外，這本書也獻給默默陪伴著我最愛的怡汶及關心我支持我的每一個人，沒有你們，我是無法獨自完成這本論文，衷心的謝謝你們。

涂博閔 于 101 年 6 月 28 日

交通大學光電工程研究所

Eco-Electronics Research Group

ECO ELECTRONICS
NATIONAL CHIAO TUNG UNIVERSITY

Contents

Abstract (in Chinese) i

Abstract (in English) iii

Acknowledgement (in Chinese) v

Contents vii

List of Figures x

List of Tables xv

Chapter 1 Introduction 1

1.1 Wide Bandgap Ⅲ-Nitride Materials 1

1.2 GaN-based Near-Ultraviolet Light-Emitting Diodes (Near-UV LEDs) 2

1.3 Content of Dissertation 9

Chapter 2 Properties of InGaN-based Near-UV LEDs 11

2.1 Structure of InGaN-based Near-UV LEDs 11

2.1.1 Epitaxy Structure of InGaN-based Near-UV LED 11

2.1.2 Chip Structure of Near-UV LEDs 14

2.2 The Physical Definition of Efficiencies 17

2.3 The Basic Concept of Efficiency Droop 19

Chapter 3 Experimental Instruments and Physical Models 21

3.1 Metal-organic Chemical Vapor Deposition System (MOCVD) 21

3.2 Materials and devices analysis 23

3.2.1 Photoluminescence (PL) 23

3.2.2 Atomic Force Microscopy (AFM) 25

3.2.3 Double Crystal X-ray Diffraction (DCXRD) 26

3.2.4 Scanning Electron Microscopy (SEM) 29

3.2.5 Transmission Electron Microscopy (TEM) 30

3.2.6 Electroluminescence (EL) 32

3.3 Advanced Physical Models of Semiconductor Devices (APSYS) 33

3.3.1 Theoretical Model 33

3.3.2 Bandgap Energy of Ⅲ-Nitride Alloys 35

3.3.3 Band Offset Ratio of Ⅲ-Nitride Alloys 37

3.3.4 Carrier Transportation in Ⅲ-Nitride Alloys 37

Chapter 4 Investigation of Efficiency Droop for InGaN-Based Near-UV Light-Emitting Diodes with InAlGaN Barrier 41

4.1 Introduction 41

4.2 Sample Structures and Fabrication Methods 41

4.3 Investigation of Optical Property and Surface Morphology 44

4.3.1 Optical Properties 44

4.3.2 Surface Morphology 45

4.3.3 Compositions and Thicknesses Analysis 47

4.4 Current-dependent Intensity and Efficiency 50

4.5 Theoretical Analysis 59

4.6 Summary 60

Chapter 5 High Quality GaN-based Vertical LED with Hexagonal Inversed Pyramid by Means of the Mechanical Lift-off 61

5.1 Introduction 61

5.2 Sample Structures and Fabrication Methods 62

5.2.1 Fabrication the Hexagonal Inversed Pyramid (HIP) Structure 62

5.2.2 Regrowth LED Structure and Wafer Bonding Process 63

5.2.3 Mechanical Lift-off by using HIP structure 63

5.3 Characteristics of GaN-based V-LED with HIP Structure 64

5.3.1 HIP Structure 64

5.3.2 Interface Morphologies 65

5.3.3 Vertical LED Structure and Surface Morphology 67

5.3.4 Raman Spectroscopy Analysis 68

5.3.5 Electrical and Optical Properties 70

5.4 Theoretical Analysis of Mechanical Lift-off 72

5.5 Summary 73

Chapter 6 Conclusions and Future Work 75

References 79

Publication list 87

Vita 92

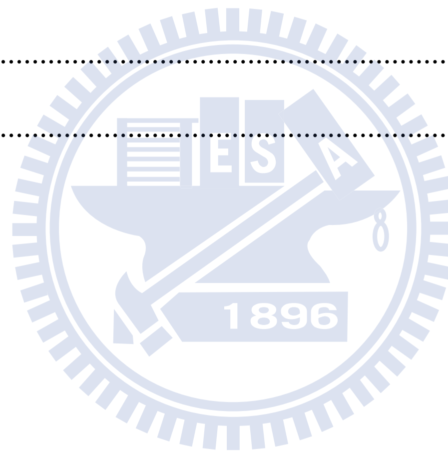

List of Figures

Fig. 1.1.1. Bandgap energy versus lattice constant of III-V nitride semiconductors at room temperature. 1

Fig. 1.2.1. X-ray rocking curve for (0006) diffraction from GaN grown at 970 ℃ with the AlN buffer layer. Dotted line shows data obtained by HVPE. 3

Fig. 1.2.2. Photoluminescence spectra of GaN:Mg (b) before and (a) after the electron beam treatment. The ratio of the two peaks is 100. 3

Fig. 1.2.3. The Hall mobility and carrier concentration measured at 77 K and 300 K as a function of the thickness of the GaN buffer layer. 4

Fig. 1.2.4. Resistivity of GaN:Mg after annealing at various temperatures. 5

Fig. 1.2.5. Structure of III-Nitride light emitting diodes (LEDs). 6

Fig. 1.2.6. Applications of Near-UV LEDs. 6

Fig. 1.2.7. Benchmark of UVA LED in the wavelength range from 320 to 410 nm. 8

Fig. 2.1.1. Schematic of nitride-based near-UV LED of Nichia. 12

Fig. 2.1.2. Absorption coefficient of a semiconductor with bandgap Eg versus energy. 13

Fig. 2.1.3. Schematic of GaN-based mesa-type chip. 15

Fig. 2.1.4. Schematic of a UV LED flip-chip mounted onto a heat sink substrate. 16

Fig. 2.1.5. Schematic of a GaN-based vertical chip. 16

Fig. 2.2.1. Illustration of radiative and non-radiative transition in a semiconductor. 17

Fig. 2.3.1. Efficiency droop of GaN-based LEDs 19

Fig. 3.1.1. III-N based MOCVD system (Nippon Sanso SR-4000). 22

Fig. 3.1.2. Scheme of metal-organic chemical vapor deposition (MOCVD) growth. 22

Fig. 3.2.1. Schematic band diagrams for the photoluminescence processes in a direct gap material. 24

Fig. 3.2.2. The schematic of experimental Photoluminescence setup. 25

Fig. 3.2.3 Concept of AFM and the optical lever: (a) a cantilever touching a sample (b) illustration of the meaning of "spring constant" as applied to cantilevers (c) the optical lever (d) AFM cantilever image. 26

Fig. 3.2.4. The photograph and the schematic setup of DCXRD system. 27

Fig. 3.2.5. Bragg diffraction from (a) a symmetric plane and (b) an asymmetric plane. 28

Fig. 3.2.6. Geometry for x-ray rocking curve. The angle movement for the detector is twice that of the sample. 29

Fig. 3.2.7. Schematic diagram of a SEM. 30

Fig. 3.2.8. Ray diagram showing two basic operations of TEM. 31

Fig. 3.2.9. The schematic of electroluminescence setup. 32

Fig. 3.2.10. The photograph of electroluminescence measure system. 32

Fig. 4.2.1. Schematic of InGaN/AlGaN and InGaN/InAlGaN MQWs structures. 43

Fig. 4.2.2. Schematic of AlGaN and InAlGaN single heteroepitaxial layers. 44

Fig. 4.3.1. Room-temperature PL spectra of AlGaN and InAlGaN single heteroepitaxial layers. 45

Fig. 4.3.2. Shows surface morphology AFM over 5×5 μm2 of AlGaN (RMS:0.813 nm) and InAlGaN (RMS:0.595 nm) layer with thickness about 50 nm. 46

Fig. 4.3.3. Surface morphology of top-view AFM images over 5×5 μm^2 of LT GaN, AlGaN, and InAlGaN layer. 47

Fig. 4.3.4. HRXRD (ω-2θ) curves in the (a) (004) and (b) (105) reflections of GaN, AlGaN, and InAlGaN single heteroepitaxial layers. 48

Fig. 4.3.5. HRXRD (105) RSM of GaN, AlGaN, and InAlGaN single heteroepitaxial layers. 48

Fig. 4.3.6. HRXRD (ω-2θ) curves in the (002) reflections of InGaN/AlGaN and InGaN/InAlGaN MQWs. 49

Fig. 4.3.7. Cross-sectional TEM images of (a) InGaN/AlGaN and (b) InGaN/InAlGaN MQWs. The diffraction condition is g0002. 49

Fig. 4.3.8. Cross-sectional TEM images of (a) InGaN/AlGaN and (b) InGaN/InAlGaN LED structures. Inset in Fig. 4.3.8 shows ternary and quaternary MQWs structure. 50

Fig. 4.4.1. (a) 2-inch near-UV LED epi-wafer under 100 mA, (b) the mesa-type near-UV chip and (c) chip image under 350 mA driving current. 51

Fig. 4.4.2. L-I-V curves of the LEDs with AlGaN (dash) and InAlGaN (solid) barrier. 51

Fig. 4.4.3. Normalized Efficiency curves of experimental (open circles) and simulated (solid lines). 52

Fig. 4.4.4. EL spectra for InGaN/AlGaN and InGAN/InAlGaN MQWs under (a) (b) CW current and (c) (d) pulsed current with 100 μs and a 1 % duty cycle. 53

Fig. 4.4.5. EL peak energy of the (top) near-UV and (bottom) green LEDs as a function of the CW and pulsed modes. 54

Fig. 4.4.6. EL spectra for the near-UV LED (top) with increasing (a) CW current and (b) pulsed current, and green LED (bottom) with increasing (c) CW current and (d) pulsed current with a duty cycle of 1 %. 55

Fig. 4.4.7. Bandgap (dashed-line contours) and total polarization charge (solid-line contours) of AlGaInN as a function of Al and In compositions. 56

Fig. 4.4.8. Schematic of band diagram and band-offset ratio from 6:4 (InGaN/AlGaN) to 7:3 (InGaN/InAlGaN). 57

Fig. 4.4.9. Normalized IQE of InGaN/InAlGaN near-UV LED with different band-offset ratio from 5:5, 6:4 to 7:3. Inset in Fig. 4.4.9 shows the L-I curves of the InGaN/InAlGaN LEDs. 57

Fig. 4.4.10. Simulation results of normalized IQE under different carrier mobility. 58

Fig. 4.5.1. Distribution of (a) Electron (b) Hole concentrations, and (c) Radiative recombination

rates concentrations of the LEDs with AlGaN and InAlGaN barrier under a high forward current den sity of 100 A/cm^2. 59

Fig. 5.2.1. Schematic of (a) ud-GaN/Sapphire (b) top-down etching (c) lateral etching (d) HIP GaN/air/Sapphire structure. 62

Fig. 5.2.2. The process flowchart for fabrication of GaN-based vertical LED: (a) GaN on Sapphire; (b) The HIP GaN/air/Sapphire structure; (c) GaN-based LED structure on HIP GaN/air/Sapphire template; (d)Wafer bonding process; (e) Remove sapphire substrate by mechanical lift-off during cooling process. 64

Fig. 5.3.1. (a) The tilted SEM image of the HIP structure; (b) SEM image of the etched GaN surface. Inset in Fig. 5.3.1 show the zoom in view images of the HIP structure. 65

Fig. 5.3.2. Cross-sectional SEM images of (a) The regrowth HIP GaN/air/Sapphire interface; (b) Zoom in view of the interface. 66

Fig. 5.3.3. Cross-sectional TEM images of (a) GaN-based LED structure grown on HIP GaN/air/Sapphire template (b) The regrowth HIP GaN/air/Sapphire boundary. The diffraction condition is g0002. 67

Fig. 5.3.4. Cross-sectional SEM image of the vertical LED structure after mechanical lift-off GaN LED/Silicon from sapphire substrate. Inset in Fig. 5.3.4 shows top-view SEM image of the HIP surface morphology after lift-off from sapphire substrate. 68

Fig. 5.3.5. Room temperature Raman spectrum of GaN epilayer regrowth on HIP structure and mechanical lift-off by HIP structure. 69

Fig. 5.3.6. (a) EL spectra of Ref-LED and V-LED in normal direction at 20mA. (b) The peak wavelength shift of the LEDs. Inset in Fig. 5.3.6 (a) shows the schematic of the Ref-LED and V-LED. 70

Fig. 5.3.7. L-I-V characteristics of the two fabricated LEDs. 71

Fig. 5.3.8. (a) An image of V-LED/Si wafer after lift-off process from sapphire substrate. (b)

The light emitting image of near-UV V-LED is observed at 20 mA operating currents. (c) OM image of 380×380 μm^2 V-LED chip at a 1 mA current injection. 71

Fig. 5.4.1. Schematic of mechanical lift-off process. 73

Fig. 6.1. Schematic structures of 365 nm UV LEDs with (a) $Al_{0.15}Ga_{0.85}N$ barrier and (b) $In_{0.02}Al_{0.18}Ga_{0.8}N$ barrier. 77

Fig. 6.2. The process flowchart for fabrication of V-LEDs by using the porous SiO_2/GaN nanorod array. 78

List of Tables

Table 3.1. Material parameters of the binary semiconductors GaN, AlN, and InN at room temperature. 34

Table 3.2. Bandgap energy of GaN, AlN and InN related-temperature parameters. 36

Table 3.3. Mobility parameters of GaN, AlN and InN. 40

Table 4.1. Growth parameters of the InAlGaN, AlGaN, and InGaN MQWs 43

Table 4.2. Simulation parameters in band-offset ratio and carrier mobility. 59

Table 5.1. The Raman shift of E_2 (high) mode and strain value. 69

Chapter 1

Introduction

1.1 Wide Bandgap Ⅲ-Nitride Materials

In recent decades, the III-Nitrides materials (InN, GaN, and AlN related alloys) become an interesting class of wide bandgap materials and play an important role in semiconductor devices [1-6]. Wide direct bandgap nitride materials have attracted great attention due to their promising potential for the applications of optoelectronic devices such as backlight of display, competing storage technologies, automobiles, general lighting, and biotechnology [7-10]. The bandgap of III-nitrides material cover a very wide range, from 0.7 eV for InN, to 3.4 eV for GaN, and to 6.1 eV for AlN [11, 12], which represents the emission wavelength from infrared (IR) region to deep ultraviolet (UV). Fig. 1.1.1 shows the bandgaps of various alloys of III-Nitrides [13].

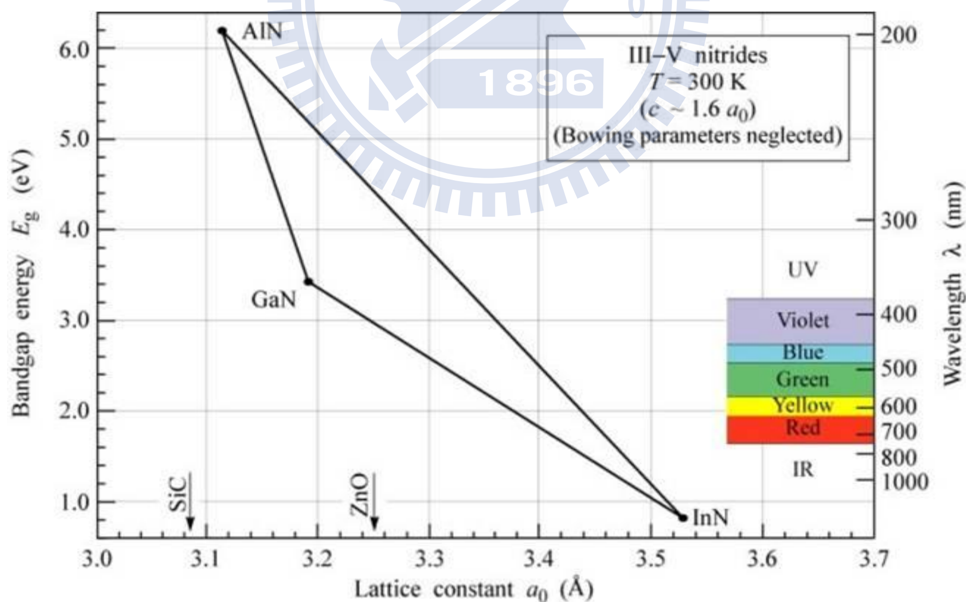

Fig. 1.1.1. Bandgap energy versus lattice constant of III-V nitride semiconductors at room temperature.

The wide bandgap implies the large band off-set in hetero-structure or multi quantum well (MQW) could be achieved in this material system. The large band off-set is very useful

to confine carrier for the high-speed and high power electronic devices and light emitting devices [14]. Although wurtzite nitride compounds have some unique properties such as piezoelectric field and spontaneous polarization which is unfavorable to the efficiency of optoelectronic devices, the material system still is a very strong candidate for the future optoelectronic applications due to their superior material properties.

1.2 GaN-based Near-Ultraviolet Light-Emitting Diodes (Near-UV LEDs)

Pioneering work of Pankove, Akasaki, Amano, Schubert, and Nakamura has led to the development of bright green and blue LEDs based on nitride semiconductors in the recent decade. The first blue light-emitting diode (LED) using III-nitrides materials was fabricated by J. I. Pankove *et al.* [15] in 1972. Since that, related research about GaN-based material is going on continually. However, progresses have been limited because of highly background *n*-type concentration resulting from the native defects commonly thought to be nitrogen vacancies and residual impurities such as silicon and oxygen acted as an efficient donor, poorly conducting *p*-type GaN, and the lack of appropriate substrates for epitaxial growth. Until late 1980s, I. Akasaki and H. Amano *et al.* discovered a very useful method of an AlN buffer layer and developed low-energy electron beam interaction (LEEBI) techniques to obtain a better quality GaN film and conductive *p*-type GaN layer [16-18]. The quality of GaN thin film grown by atmospheric pressure metal-organic vapor phase epitaxial (AP-MOVPE) using AlN buffer layers is shown to be excellent in terms of morphological, crystalline, and optical properties. Using AlN buffer layers, GaN thin films with optically flat surfaces free from cracks are successfully grown. The narrower x-ray rocking curve of GaN film with AlN buffer layer from the (0006) plane is shown in Fig. 1.2.1 [16]. In 1989, I. Akasaki *et al.* put a sample of GaN:Mg in a scanning electron microscope (SEM) with an optical window through which they could see the blue cathodoluminescence. As shown in Fig.

1.2.1, they noticed that the intensity of luminescence kept getting stronger the longer they scanned. When the brightness seemed to saturate they took the sample out and measured the Hall effect. To their great surprise and to the world's astonishment, the previously insulating sample had become conducting p-type [17].

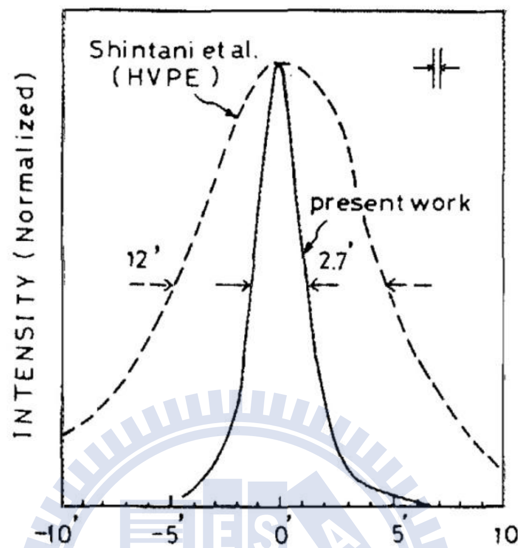

Fig. 1.2.1. X-ray rocking curve for (0006) diffraction from GaN grown at 970 ℃ with the AlN buffer layer. Dotted line shows data obtained by HVPE.

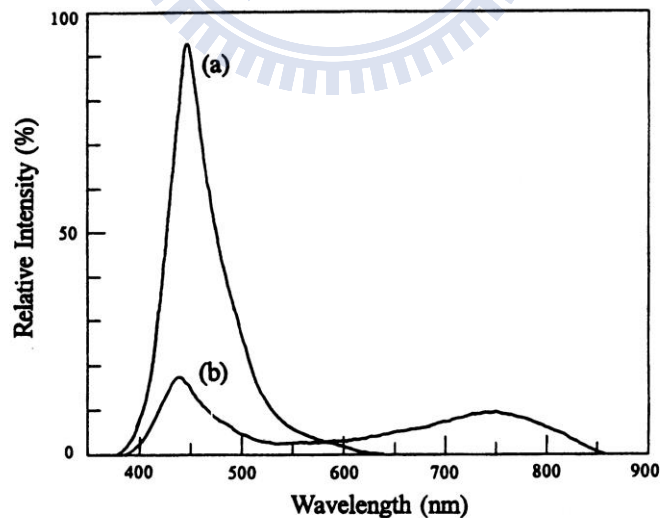

Fig. 1.2.2. Photoluminescence spectra of GaN:Mg (b) before and (a) after the electron beam treatment. The ratio of the two peaks is 100.

Until 1991, S. Nakamura developed a new buffer layer for high quality GaN growth by MOVPE. Strenuous efforts were made to optimize growth conditions by introducing suitable

buffer layers (between the sapphire substrate and the active GaN) of GaN grown at low temperatures (~ 500 ℃) and by adjusting flow rates and temperatures with the object of reducing n-type background doping levels and increasing Hall mobility. The optimum thickness of the GaN buffer layer was around 200 Å. Fig. 1.2.3 shows the Hall mobility and carrier concentration measured at 77 K and 300 K as a function of the thickness of the GaN buffer layer. This eventually proved successful high Hall mobility values of 600 $cm^2/V \cdot s$ at 300 K and background levels below 10^{17} cm^{-3} were achieved, followed by the important breakthrough of p-type doping at the end of the 1980s [19].

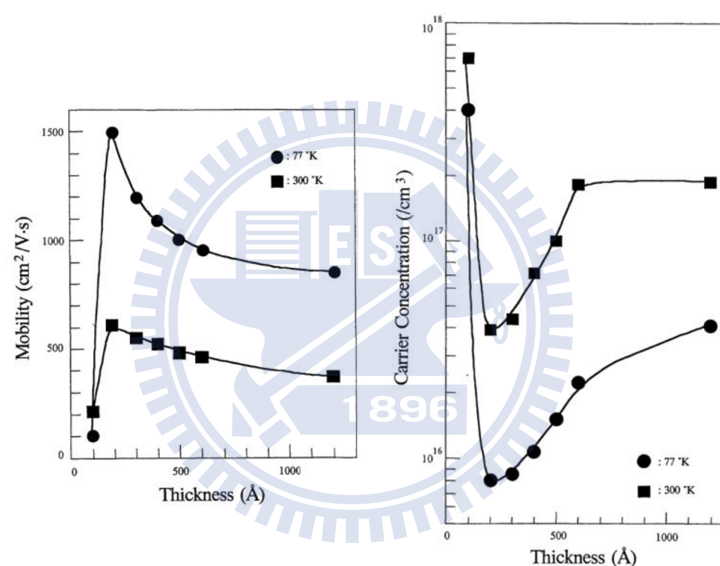

Fig. 1.2.3. The Hall mobility and carrier concentration measured at 77 K and 300 K as a function of the thickness of the GaN buffer layer.

These discoveries initiated a new strong interest in this research field. Finally, the first GaN-based blue LED constructed of a real p-n junction was achieved, which had greatly improved in the device performance. However, the acceptor concentration of *p*-type GaN is still too low such that the application of these materials is still unreliable. After that, in 1992, S. Nakamura *et al.* made the definitive experiment that showed by thermal annealing in nitrogen ambient that above 700℃ the passivating H was dissociated from Mg, rendering GaN conducting p-type. Fig. 1.2.4 shows the resistivity of GaN:Mg after annealing at various

temperatures. H could be reintroduced by heating in NH_3 making GaN:Mg insulating again [20]. Afterward Nakamura and Mukai *et al.* [21] succeeded in growing high-quality InGaN films that emitted strong band-to-band emission from green to UV region by changing the indium content of InGaN with a two-flow MOCVD method. Nowadays, most of III-Nitride based LEDs use InGaN as active layer instead of GaN, since adding a small amount of indium into the GaN is very important to obtain a strong band-to-band emission at RT.

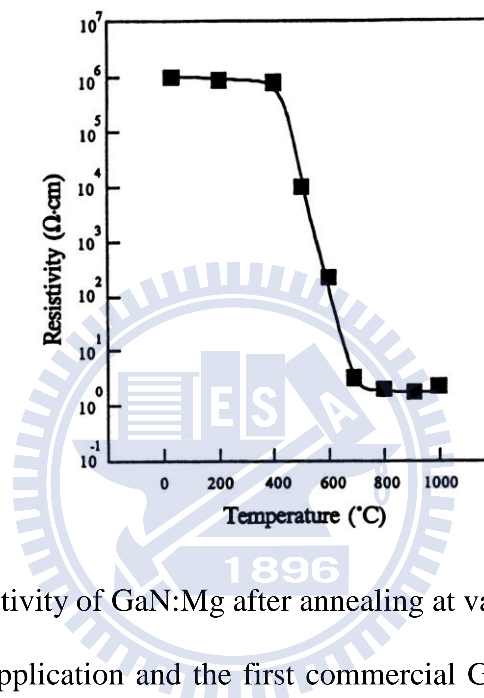

Fig. 1.2.4. Resistivity of GaN:Mg after annealing at various temperatures.

The most spectacular application and the first commercial GaN product is the LED. In 1997, Nakamura *et al*. have produced the brightest LEDs using GaN p-n junctions that include a Zn-doped well as shown in Fig. 1.2.5 [22]. The purpose of the well is to confine the carriers in a small volume, and the purpose of the Zn is to introduce an efficient blue or green luminescent center [23].

Further development of the AlN, AlGaN and AlInGaN materials resulted in an appearance of ultraviolet (UV) LEDs which represent the next frontier in solid-state optoelectronics with a large potential in biological, medical and environmental instrumentation, resin curing, photo-catalyst for disinfection and deodorization, UV light source [24], and there have been interests in solid-state lighting by using near-UV LEDs light

for the phosphor-converting source [25, 26].

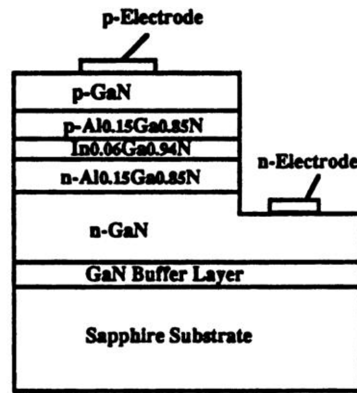

Fig. 1.2.5. Structure of III-Nitride light emitting diodes (LEDs).

Near-UV LED has some unique advantages, such as safer operation with very low heat generation, low electricity consumption, without UVB and UVC dangerous wavelengths, no warm-up time, instant turn on/off, lower operating voltage, compact and scalable design for ease of integration, much longer service life, and environmentally friendly with no ozone emissions or dangerous mercury. Fig. 1.2.6 shows extensively applications of Near-UV LEDs.

Fig. 1.2.6. Applications of Near-UV LEDs.

A great progress in solid-state sources of GaN-based *p-n* junction UV light was achieved by Akasaki *et al.* in 1992 [4]. Present UV LEDs are based on heterostructures developed using GaN-based materials such as GaN/AlGaN [27], InGaN/AlGaN [28], AlGaN/AlGaN

[29], and quaternary AlInGaN [30, 31]. There are two main issues of GaN-based UV LED: the chips must feature band diagrams structure that assists high efficiency of carrier injection into the active layer, the internal quantum efficiency (IQE) should be maximized by enhancing radiative recombination and restraining the nonradiative recombination, and light generated in active layer must be efficiently extracted from the chip. Certainly, reduction of the dislocation density, solving self-absorption of GaN, and preventing cracking of epitaxial layers mismatched to the substrate is one of the most important issues.

Most of GaN-based UV LEDs are grown on sapphire substrate, which has a 16 % lattice mismatch with GaN. This disadvantage is being bypassed through dislocation reducing by epitaxial lateral overgrowth (ELO) and by using superlattices, strain-compensating layers and quaternary AlInGaN alloys. To increase the IQE of UV LEDs, optimization of quantum well structures is necessary through selecting composition and doping profiles of the well, barrier and p-type layers, shaping of the interfaces between well and barrier, and engineering of the built-in electric field to avoid the quantum-confined Stark effect (QCSE). In addition, basic investigation for unveiling the routes of nonradiative recombination in AlGaN alloys with high molar fraction of aluminum is needed. To overcome the high resistivity of p-AlGaN, novel doping approaches including piezoelectric and super-lattice doping, graded composition, and co-doping of magnesium (Mg) and indium (In) are being developed.

First commercial 375 nm LEDs were fabricated by Nichia in 1998 [28]. Typically, these devices feature 1.5~2 mW light output power and are available with the out-coupling optics for narrow-angle (20 °) and wide-angle (110 °) far-field radiation pattern. Cree fabricated the first near-UV LED for use in the illumination market in 2001. The InGaN based devices were grown on SiC substrate, and the light output power was about 12 mW with the wavelength between 395~405 nm. These near-UV LEDs have a geometrically enhanced vertical chip structure to maximize light extraction efficiency and require only a single Au-wire bond

connection with the device.

Shown in Fig. 1.2.7 is the benchmark of history development of GaN-based UVA LED in the wavelength range from 320 to 410 nm [32]. From the benchmark, it can be deliberated that the UV LED has an energetic development after 1998.

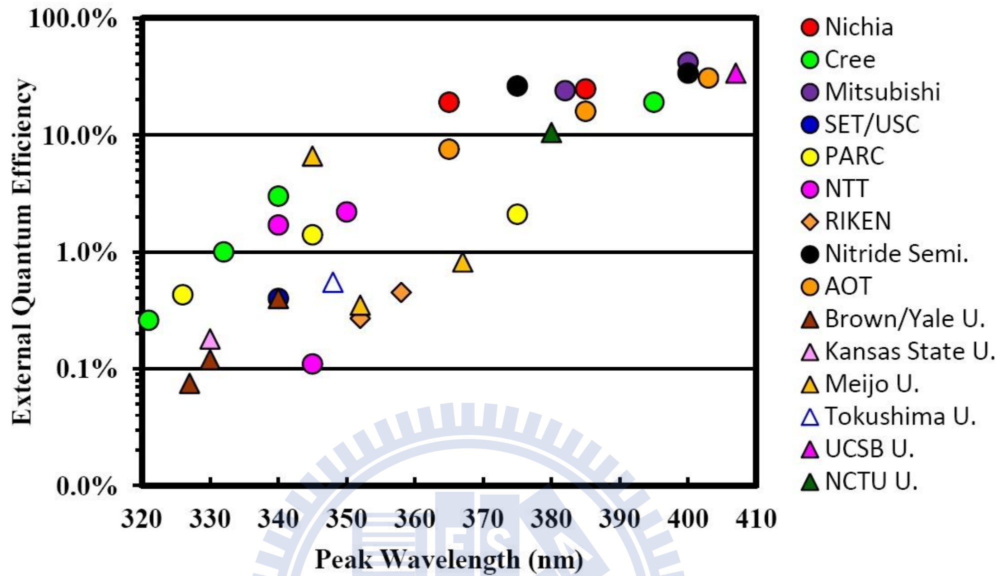

Fig. 1.2.7. Benchmark of UVA LED in the wavelength range from 320 to 410 nm.

Although the excellent external quantum efficiency (EQE) that have been obtained by many groups for LEDs in the near UV range, the EQE of InGaN-based UV LEDs with emission wavelength shorter than 365 nm is at least one order of magnitude below the best devices in the near-UV wavelength range about 400 nm. There are multiple causes that currently limit the EQE of GaN-based UV LEDs. For example, with decreasing wavelengths, the light output power is dropping and challenges in growing high quality nitride heterostructures with a high aluminum (Al) molar fraction are becoming more difficult [30]. The solutions to device problems lie in using better substrates (ex: AlN substrates in non-polar orientations, and patterned sapphire substrate), using better epitaxial growth techniques (ex: ELO), improving device design (ex: vertical chip and flip chip) and using better contact technology.

1.3 Content of Dissertation

In this study, there are several major contributions for fabricating high efficient near-UV LEDs such as (a) inserting a quaternary material of InAlGaN layers for quantum barrier (b) fabricating a high quality GaN-based V-LED structure by using mechanical lift-off (MLO) technology, will review as below:

(a) InAlGaN barrier near-UV LED

One of the major problems of efficiency decay in near-UV is the lack of an excellent distribution of carriers in multi-quantum-well (MQW) active region. To solve this issue, we prepare a 50-nm InAlGaN and AlGaN single heteroepitaxial layers, and the quaternary structure of InGaN/InAlGaN and ternary structure of InGaN/AlGaN MQW grown on n-AlGaN/ud-GaN/Sapphire substrate. Several properties of optical, surface morphology and MQWs structure have been measured by photoluminescence (PL), atomic force microscopy (AFM), high-resolution double crystal x-ray diffraction (DCXRD) and transmission electron microscopy (TEM), respectively. Electroluminescence (EL) results indicate that the light output power of quaternary LEDs can be enhanced by 25 % and 55 % at 350 mA and 1000mA, respectively. Finally, the optical and electrical properties of quaternary InGaN/InAlGaN and conventional InGaN/AlGaN MQW LEDs are numerically calculated using the APSYS simulation software [33]. Simulation results show that InGaN-based UV LEDs with quaternary InAlGaN barrier exhibit higher radiative recombination rate and low efficiency droop. The details of the physical origin in efficiency droop are investigated in chapter 4.

(b) Mechanical lift-off (MLO) technology

Sapphire is the most commonly used substrate because of its relative low cost during the last decade of years, but it also limits the devices performance due to its poor electrical and thermal conductivity. In order to improve the device performance, it is necessary to develop a

method to separate device from sapphire substrate. The techniques of laser lift-off (LLO) [34, 35] and chemical lift-off (CLO) [36-38] have been adopted to fabricate the freestanding GaN membrane and the vertical LEDs (V-LEDs) for the purpose of high performance devices. However, the LLO process may induce some possible damages under high temperature in the GaN/sapphire interface. And even though the CLO can prevent the GaN layer from the laser damage during the laser lift-off process, but it also makes another chemical etching damages and reduce the crystal quality. Hence, we study the fabrication of mechanical lift-off (MLO) for high quality GaN-based V-LEDs with Hexagonal Inversed Pyramid (HIP) structures. Scanning electron microscopy (SEM) and transmission electron microscopy (TEM) images reveal the clear GaN/sapphire interface before and after the re-growth process. Raman spectrum shows the residual stress of the LED can also be considerably reduced while introducing the HIP structure to the GaN/sapphire interface. Finally, the optical and electrical properties of high efficient near-UV V-LEDs have been measured and the physical mechanisms of lift-off process are also carefully investigated in chapter 5.

Chapter 2

Properties of InGaN-based Near-UV LEDs

For many biological, medical and environmental instrumentation, resin curing, and photo-catalyst applications as mentioned previously, LEDs operating in the UV region of the spectrum are more and more interested. However, any LED-emitting radiation above the energy of violet light is accessible by low indium-nitride (InN) molar fraction indium-gallium -nitride (InGaN) active layer, some amount of In seems to be a requisite for localization-enhanced radiative emission. Besides, with decreasing wavelengths, the efficiency is dropping and challenges in growing high quality nitride-based barrier with a high aluminum (Al) molar fraction are becoming more difficult. Nevertheless, LEDs based on InGaN quantum well active layers just below the violet wavelengths have been developed and the range of wavelength between 380 nm and 410 nm is denominated near-UV LEDs.

The properties of physical and material such as InGaN active layer, GaN self-absorption, indium-tin-oxide (ITO) film serving as a transparent contact layer (TCL), definition of efficiencies, and the origin of efficiency droop of InGaN-based near-UV LEDs will be described in detail in this section.

2.1 Structure of InGaN-based Near-UV LEDs

2.1.1 Epitaxy Structure of InGaN-based Near-UV LED

Currently, the most commonly used method to achieve GaN-based LEDs is using by metal-organic chemical vapor deposition (MOCVD) system. A detailed introduction of MOCVD technology will be described in Chap. 3.

For the growth of InGaN-based LEDs, trimethyl gallium (TMGa), trimethyl indium (TMIn), trimethyl aluminum (TMAl), and ammonia (NH_3) were used as the source precursors

for Ga, In, Al, and N, respectively. Silane (SiH_4) and bis-cyclopentadienyl magnesium (Cp_2Mg) were used as n-type and p-type dopants. The conventional structure of InGaN-based near-UV LEDs consists of a low-temperature (500°C) 30-nm-thick GaN nucleation layer, a 1-μm-thick un-doped GaN buffer layer, a 3-μm-thick Si-doped GaN cladding laye (or Si-doped AlGaN cladding layer), a InGaN active layer (or 10 periods of InGaN/AlGaN MQWs active region), a 20-nm-thick Mg-doped AlGaN cladding layers serving as a electron blocking layer (EBL), and a 100-nm-thick Mg-doped GaN contact layer.

The varieties possessing of GaN-based active layer such as InGaN single-quantum-well (SQW), InGaN/GaN double heterostructure (DH) [40], GaN/AlGaN [27], InGaN/AlGaN [28], AlGaN/AlGaN [29], and quaternary AlInGaN [30, 31] multi-quantum-well (MQWs) were developed in the past two decades.

A schematic representation of a typical early variety of nitride-based near-UV LED of Nichia is illustrated in Fig. 2.1.1 [39].

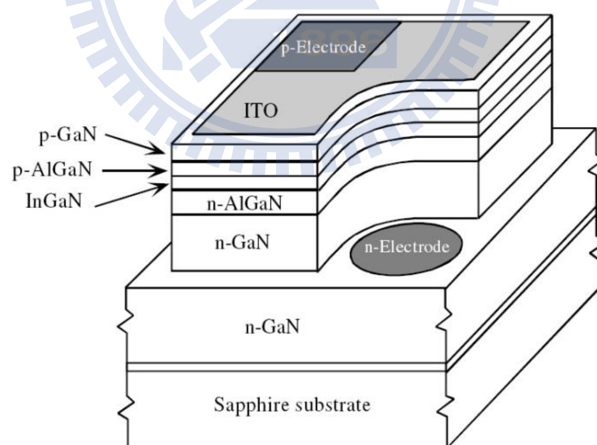

Fig. 2.1.1. Schematic of nitride-based near-UV LED of Nichia.

Some amount of In is necessary for localization-enhanced radiative intensity. Because InGaN lends itself to composition fluctuations or clustering and thus reduced adverse effects of nonradiative recombination, the emission intensity drops as the InN mole fraction is reduced near the GaN end of the ternary. As mentioned of the benchmark of UVA LED in Fig.

1.2.7, the external quantum efficiency (EQE) as functions of the wavelength. By reducing the InN mole fraction in InGaN active layer, the wavelength of operation can be shifted to the shorter spectrum. When the InN mole fraction is lower, as indicated above, the emission intensity degrades extremely. Shorter wavelength of near-UV and UV LED need larger bandgap energy to prevent the electron overflow, and the adequate barrier height whether in quantum barrier or p-type cladding layer depends on the wavelength desired.

It is worth mentioning for the issue of GaN self-absorption in near-UV LED. To obtain high light-extraction efficiency and avoid absorption of light, all semiconductor layers other than the active region should have a bandgap energy larger than the photon energy. The absorption coefficient v.s. energy of an idealized semiconductor and a real semiconductor is shown schematically in Fig. 2.1.2 [41].

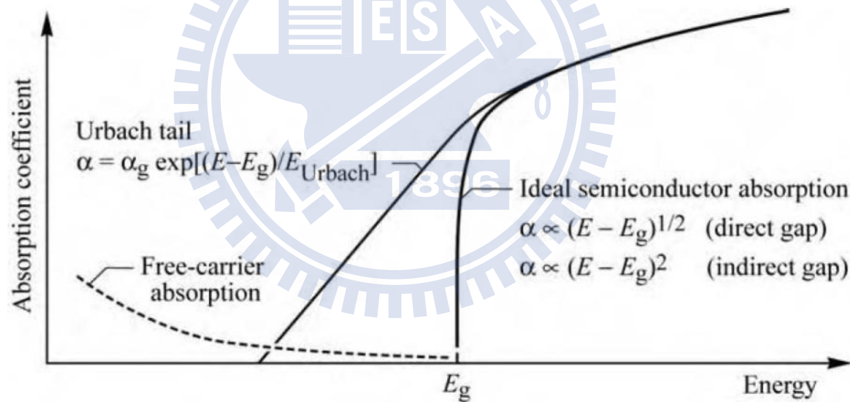

Fig. 2.1.2. Absorption coefficient of a semiconductor with bandgap Eg versus energy.

In this absorption tail, called the ***Urbach tail***, the absorption coefficient v.s. energy is given by:

$$\alpha = \alpha_g \exp\left[(E - E_g)/E_{\mathrm{Urbach}}\right] \quad (2.1.1)$$

where α_g is the experimentally determined absorption coefficient at the bandgap energy and E_{Urbach} is the characteristic energy (here called the Urbach energy), which determines how rapidly the absorption coefficient decreases for below bandgap energies. Urbach (1953) measured the absorption tail for different temperatures and showed that the *Urbach energy* is

approximately kT, the thermal energy.

The "Urbach tail" dominates absorption near but below the bandgap energy, and absorption further below the bandgap is dominated by free-carrier absorption as shown in Fig. 2.1.2.

The energy of photons emitted from a semiconductor with energy gap Eg is given by the bandgap energy, i.e.

$$h\nu = \frac{hc}{\lambda} \approx E_g \qquad (2.1.2)$$

where h is the Planck's constant, v the frequency, c the speed of light in a vacuum, and λ the wavelength of emission light.

Therefore, the wavelength of near-UV range from 410 nm to 380 nm can be converted to the energy gap by 3.02 eV and 3.26 eV, respectively. Obviously, the bandgap energy of n-GaN (3.39~3.418 eV) [42, 43] or p-GaN (3.27~2.88 eV) [44-49] is near or below the emission light of near-UV range, thus the absorption effect is more significant as the wavelength become shorter. For this reason, the applicable way to avoid self-absorption is to reduce the thickness of each layer which the bandgap energy near or below the emission light such as n-type and p-type material and replace the n-GaN by n-AlGaN under layer.

2.1.2 Chip Structure of Near-UV LEDs

There are three types of typical chip design for GaN-based near-UV LEDs: mesa-type chip, flip-chip, and vertical-chip, respectively. Because of the advantages of simple process and low cost, the most commonly used for near-UV LEDs is sapphire-based mesa-type chip. The schematic representation of a typical mesa-type chip is illustrated in Fig. 2.1.3. The light generated in the active InGaN MQWs traverses the chip without any appreciable absorption, as the entire chip is transparent to the radiation wavelength except for the self-absorption in the active layer. Due to the problematic nature of Mg-doping and the low hole mobility, the

spreading resistance in the top p-GaN layer is large. To overcome this problem, a transparent top contact such as indium-tin-oxide (ITO) became popular.

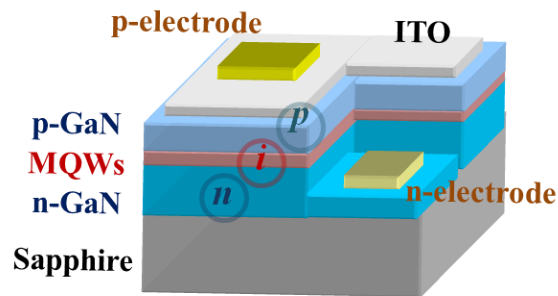

Fig. 2.1.3. Schematic of GaN-based mesa-type chip.

The LED with a transparent and conductive large-area contact made of ITO connects to the top p-type GaN layer for better optical and electrical transportation. In the wavelength around 400 nm, the transmittance through 3000 Å-thick of ITO layer is about 90 %. The method naturally keeps the lower contact resistance to the p-type GaN layer, by virtue of increased area of contact, and reduces current crowding and associated ill effects.

Flip-chip is also used in near-UV LED for high power applications. The schematic representation of a typical flip-chip is illustrated in Fig. 2.1.4 [50]. The devices were subsequently fabricated by etching square mesa structures by inductively coupled plasma (ICP), reactive ion etching (RIE) or chemically assisted ion beam etching (CAIBE) with the length of the sides ranging from 100 to 900 μm. Ti/Al metal contacts were then deposited on the exposed n-type AlGaN current spreading layer for the lateral electrical connection and Ni/Au contacts on the p-type GaN layer for hole injection [32]. The flip-chip mount method is used in which the p-side is mounted face down on a metallic mirror and the light is collected from the n-side layer and the sapphire substrate. Therefore, the method achieves the higher light extraction efficiency (LEE) and better thermal dissipation, but this design is still unable to resolve the problem of current crowding under high current density driving.

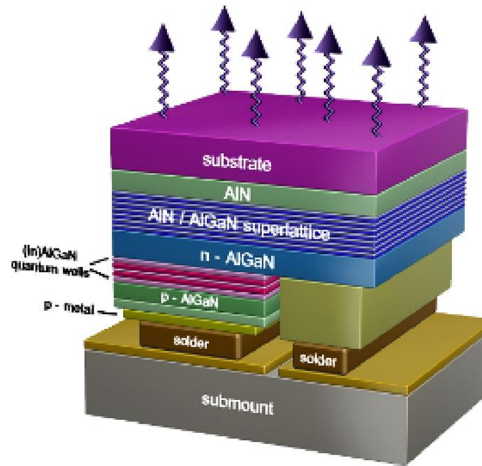

Fig. 2.1.4. Schematic of a UV LED flip-chip mounted onto a heat sink substrate.

To achieve higher light excitation and light output performance, the LED must be driven under high current density. For better thermal management, a heat sink substrate is necessary to avoid early saturation in the LED output power due to the inherent joule heating and current crowding issues. The schematic representation of a typical vertical chip is illustrated in Fig. 2.1.5.

The structure of vertical-type chip can be achieved by laser lift-off (LLO) or chemical lift-off (CLO) techniques for the purpose of high performance optoelectronic devices. Many advantages of vertical-type structure such as higher thermal conductivity for the use of metal alloyed substrate, higher reflectivity of metallic mirror between p-GaN/substrate interface, without absorption issue from TCL for the p-side down design, vertical current path for uniform current spreading, and without current crowding issue between two electrodes.

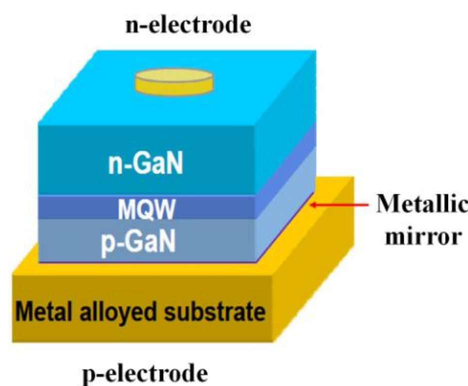

Fig. 2.1.5. Schematic of a GaN-based vertical chip.

2.2 The Physical Definition of Efficiencies

LED is a classical semiconductor diode that emits spontaneous radiation under suitable forward bias condition. Under forward bias conditions, both electrons from n-type and holes from p-type semiconductor inject into active region and then recombine in the smaller bandgap active region, and accompany by the emission of a photon (radiatively) or non-radiatively. These two recombination pathways can be considered as parallel processes occurring across the bandgap of the active region material, as illustrated in Fig. 2.2.1.

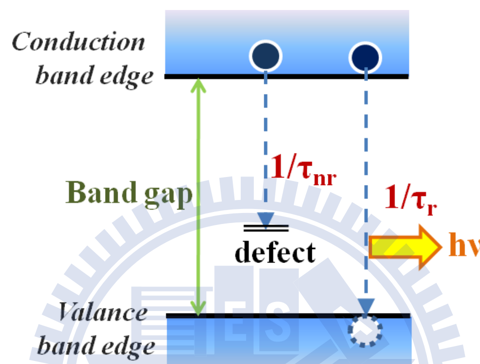

Fig. 2.2.1. Illustration of radiative and non-radiative transition in a semiconductor.

If the radiative lifetime is denoted as τ_r and the non-radiative lifetime is denoted as τ_{nr}, then the total probability of recombination in active region is given by the sum of the radiative and non-radiative probabilities:

$$\frac{1}{\tau} = \frac{1}{\tau_r} + \frac{1}{\tau_{nr}} \tag{2.2.1}$$

The relative probability of radiative recombination is given by the radiative probability over the total probability of recombination. Therefore, the internal quantum efficiency (IQE) can be expressed in terms of the radiative and non-radiative lifetimes.

$$\eta_{IQE} = \frac{{\tau_r}^{-1}}{{\tau_r}^{-1} + {\tau_{nr}}^{-1}} \tag{2.2.2}$$

where the IQE is denoted as η_{IQE}. In other words, the definition of η_{IQE} is the ratio of the photons emitted from the active region of the semiconductor to the number of electrons

injected into the p-n junction LED. From the concept of electrical excitation mechanism, the internal quantum efficiency is defined as:

$$\eta_{\mathrm{IQE}} = \frac{\text{number of photons emitted from active region/sec.}}{\text{number of electrons injected into LED/sec.}} = \frac{P_{\mathrm{int}}/h\nu}{I/e} \quad (2.2.3)$$

where P_{int} is the optical power emitted from the active region, and I is the injection current.

In an ideal LED, all photons produced in the active region will emit into free space. However, in a real device, a part of photons will not emit into the free space because of absorption and total internal reflection (TIR) issues.

The extraction efficiency can be a severe limitation for high performance LEDs. It is quite difficult to increase the extraction efficiency without resorting to high sophisticated and costly device processes. The light extraction efficiency (LEE) is defined as:

$$\eta_{\mathrm{LEE}} = \frac{\text{number of photons emitted into free space/sec.}}{\text{number of photons emitted from active region/sec.}} = \frac{P/h\nu}{P_{int}/h\nu} \quad (2.2.4)$$

where the LEE is denoted as η_{LEE}, and P is the optical power emitted into free space.

Considering the refractive indices of GaN (n = 2.5) and air (n = 1), for the light escape cone is about 23.6 % due to the critical angle. Assuming that light emitted from sidewalls and backside is neglected, one expects that approximately only 4.18 % of the internal light can be extracted from a surface of the device.

Finally, the external quantum efficiency (EQE) can be defined as:

$$\eta_{EQE} = \frac{number\ of\ photons\ emitted\ into\ free\ space/sec.}{number\ of\ electrons\ injected\ into\ LED/sec.}$$

$$= \frac{(P/h\nu)}{(I/e)} = \eta_{IQE} \cdot \eta_{LEE} \quad (2.2.5)$$

where the EQE is denoted as η_{EQE}. From the above equation, we can know that the EQE depend on IQE and LEE. Therefore, the improvement of IQE and LEE play a very important role for fabricating a high performance LED.

Finally, the wall-plug efficiency (WPE) of LEDs can be described by the following relationship:

$$\eta_{WPE} = \frac{(P_{out})}{(I \cdot V)} = \eta_{EQE} \cdot \frac{\hbar\omega}{e \cdot V} \tag{2.2.6}$$

where the WPE is denoted as η_{WPE}, P_{out} the light output power, I the drive current, V the operating voltage, and $\hbar\omega$ the photon energy [51].

2.3 The Basic Concept of Efficiency Droop

Although significant progress in GaN-based LEDs has been made in recent decades, higher efficiencies and light output power are necessary for using in general lighting and high power light source market. However, the efficiency of LED generally is highest at a low current density around a few milliampere (mA). Besides, the efficiency decreases gradually as the injection current increases [52-56]. As shown in Fig. 2.3.1, the normalized efficiency as a function of the current density shows efficiency droop of GaN-based LEDs. The efficiency reaches its peak at current densities as low as 10 A/cm^2 and monotonically decreases with further increase in current.

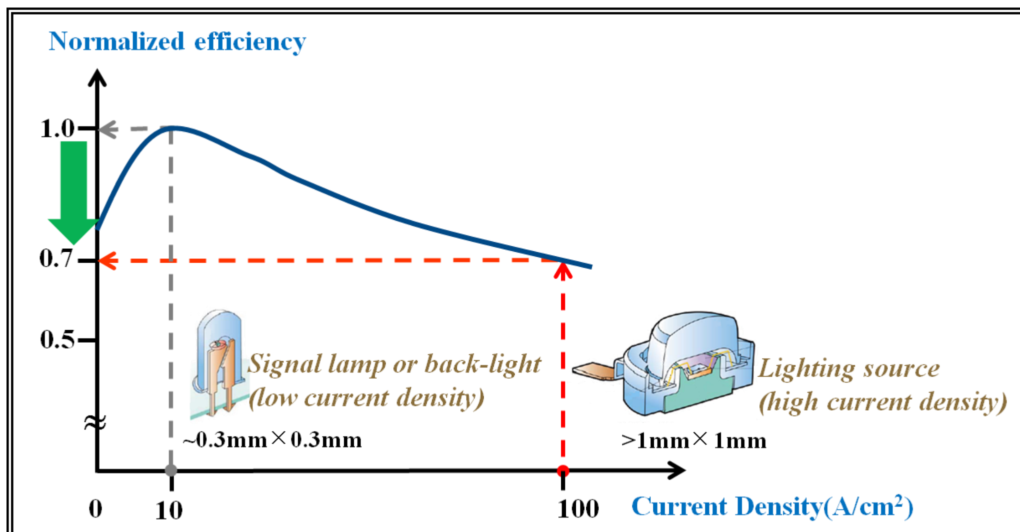

Fig. 2.3.1. Efficiency droop of GaN-based LEDs

This well-known phenomenon of efficiency droop must be solved for devices operating at high current density. A solution to the efficiency droop issue has not yet been provided, and different explanations were proposed extensively. However, the physical origin of efficiency droop is not well understood.

Currently, dislocations have been shown to reduce the overall efficiency but not affect the efficiency droop [57]. The major cause of efficiency droop in GaN-based LED is still a huge controversy in last decade of years, and several possible mechanisms of droop including carrier overflow [58-62], non-uniform distribution of holes [63, 64], Auger recombination and scattering [65-68], carrier delocalization [69-71], junction heating [72] have been proposed, but the genesis of the efficiency droop is still the topic of an active debate.

Although Auger recombination was proposed for the efficiency droop [61], the Auger losses in such a wide bandgap semiconductor are expected to be very small [73], which has also been verified that the direct Auger losses are negligible in InGaN quantum wells by using fully microscopic many body models [74].

Chapter 3

Experimental Instruments and Physical Models

Experimental instruments employed in this research contain metal-organic chemical vapor deposition (MOCVD), photoluminescence (PL), atomic force microscopy (AFM), raman system, high-resolution double crystal x-ray diffraction (DCXRD), scanning electron microscopy (SEM), cathodoluminescence (CL), transmission electron microscopy (TEM), and electroluminescence (EL). Furthermore, the physical models, bandgap energy, band offset ratio, and carrier transport mechanism will be described in detail in this chapter.

3.1 Metal-organic Chemical Vapor Deposition System (MOCVD)

Metal-organic chemical vapor deposition (MOCVD) is a growth technique that includes a dynamic flow in which gaseous reactants flow over a heated substrate and react chemically in the surface to form a semiconductor layer [75]. It has been widely used in modern semiconductor industry, which provide a way to grow high-quality semiconductor films and sharp interface. Its potentials have also been proven by producing high quality epitaxial structures with excellent surface morphology and a precise control for layer thickness and uniformity. Several epitaxial crystal growth technologies for an impressive array of commercial devices are also carried out by MOCVD, such as lasers, LEDs, photo-cathodes, high electron mobility transistor (HEMT), photo-detectors, and solar cells.

MOCVD growth is facilitated by introducing group III precursors (Al, Ga, and In) and NH_3 with carrier gases into a reactor under suitable total flow rate, rotation speed, growth temperature, and growth pressure. As shown in Fig. 3.1.1, a typical MOCVD system consists of four major parts: (a) Control panel (b) Gas delivery system (c) Reactor chamber (d) Heating system (e) Gas exhaust system.

Fig. 3.1.1. III-N based MOCVD system (Nippon Sanso SR-4000).

The precursors TriMethyl-Gallium (TMGa), TriMethyl-Aluminum (TMAl), and TriMethyl-Indium (TMIn) react with ammonia (NH_3) on the heated substrate surface to form semiconductor layers. Additional sources such as hydrogen (H_2), nitrogen (N_2), silane (SiH_4), disilane (Si_2H_6), and Bis(cyclopentadienyl) magnesium (Cp_2Mg) sources are needed. The precursor molecules NH_3 and TMAl, TMGa and TMIn are fed in separately into the reactor chamber as shown in Fig. 3.1.2.

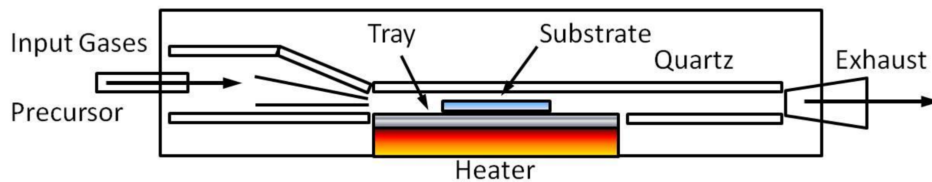

Fig. 3.1.2. Scheme of metal-organic chemical vapor deposition (MOCVD) growth.

The basic MOCVD reaction describing the GaN deposition process is:

$$Ga(CH_3)_3 + NH_3 \rightarrow GaN + 3CH_4 \quad (3.1.1)$$

However, the details of the reaction are not well known because the intermediate reactions are so complex. Several types of MOCVD system are being developed for the mass production of GaN-based materials and devices. Both atmospheric-pressure and low-pressure

systems are being produced by the major MOCVD equipment manufacturer such as Aixtron, Tomas Swan (merged by Aixtron in 1999), Veeco, Emcore (merged by Veeco in 2003), and Nippon Sanso.

3.2 Materials and devices analysis

3.2.1 Photoluminescence (PL)

Photoluminescence is a process in which a substance absorbs photons (electromagnetic radiation) and then re-radiates photons. It has been widely used as a measurement method to detect the optical properties of the semiconductor materials because of its non-destructive characteristics. PL can reveal the band structure and the carrier transportation behaviors in a semiconductor material. Moreover, the bandgap, doping type, composition, lifetime, etc. of the nano-scale semiconductor material can be shown in the PL spectrum. So the PL could be a judgment of the material quality, semiconductor characteristic, and be a key instrument of the development for nano-technology.

In general, PL system use a laser as a light source, and the laser light source used to excite carriers should have larger energy bandgap than the semiconductor materials. When the laser light is absorbed within the semiconductors, it would excite the carriers from the valence band to the conduction band. During the process it produces the electrons in the conduction band and the holes in the valence band as shown in Fig. 3.2.1. In a direct gap material, the conduction band minimum and the valence band maximum occur at the same k values. Direct gap semiconductor materials are excellent light emitters and their optical properties can be analyzed by using this technique.

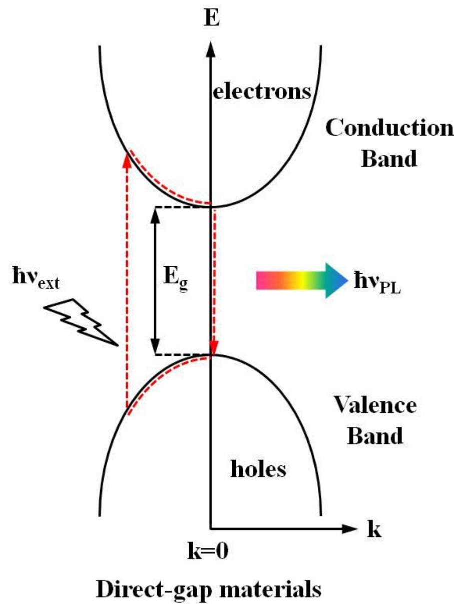

Fig. 3.2.1. Schematic band diagrams for the photoluminescence processes in a direct gap material.

The PL spectroscopy is the optical measurement to examine the quality and optical characteristic of material. First, when we analysis an unknown compound semiconductor, we can use PL measurement to know the band gap of the unknown material. Second, the intensity of PL signal is contributed to the amount of radiative recombination in the materials. Therefore, PL measurement can be used to understand the material quality and the recombination mechanisms of the materials.

The schematic setup of our PL system is shown in Fig. 3.2.2. The pumping source was a multi-mode and non-polarized Helium-Cadmium laser operated on 325 nm with 35 mW. After reflecting by three mirrors, the laser light was focused by a lens which focal length was 5 cm, to 0.1 mm in diameter and the luminescence signal was collected by some lens. The probed light was dispersed by 0.32 monochromator (Jobin-Yvon Triax-320) with 1800, 1200, and 300 grooves/mm grating and the maximum width if the entrance slit was 1 mm. In order to prevent the laser coupling with the PL spectrum, we used the long pass filter in front of the entrance slit.

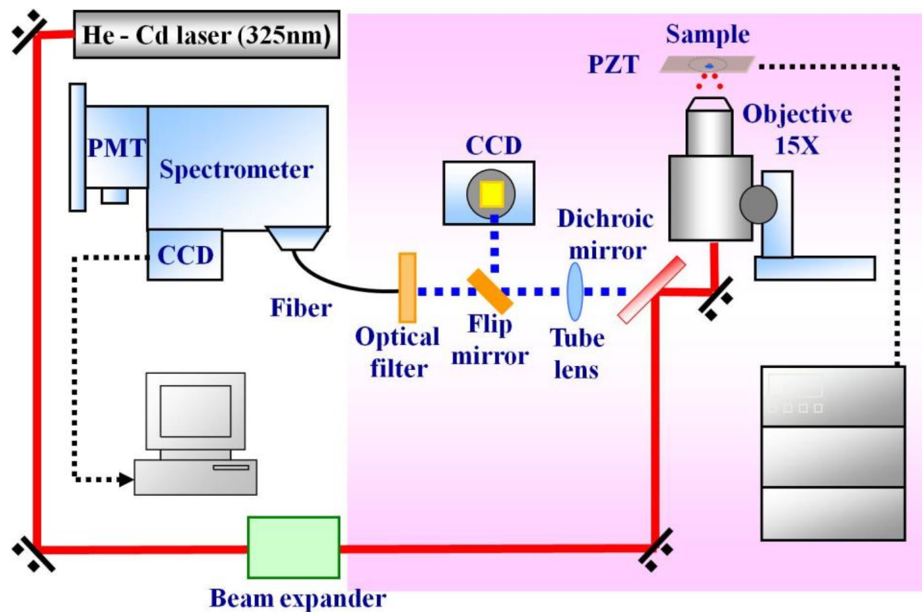

Fig. 3.2.2. The schematic of experimental Photoluminescence setup.

3.2.2 Atomic Force Microscopy (AFM)

Atomic force microscopy (AFM) or scanning force microscopy (SFM) is a very high-resolution type of scanning probe microscopy, with demonstrated resolution on the order of fractions of a nanometer, more than 1000 times better than the optical diffraction limit of optical microscope system. The AFM or SFM was invented in 1986 by Binnig, Quate and Gerber. Like all other scanning probe microscopes, the AFM utilizes a sharp probe moving over the surface of a sample in a raster scan.

The AFM consists of a cantilever with a sharp tip (probe) at its end that is used to scan the sample surface. Fig. 3.2.3 shows the concept of AFM and the optical lever. As shown in Fig. 3.2.3 (a), the probe is a tip on the end of a cantilever which bends in response to the force between the tip and the sample. The small probe-sample separation (on the order of the instrument's resolution) makes it possible to take measurements over a small area. To acquire an image the microscope raster-scans the probe over the sample while measuring the local property in question. The resulting image resembles an image on a television screen in that

both consist of many rows or lines of information placed one above the other. Unlike traditional microscopes, scanned-probe systems do not use lenses, so the size of the probe rather than diffraction effect generally limits their resolution. The cantilever is typically silicon or silicon nitride with a tip radius of curvature on the order of nanometers as shown in Fig. 3.2.3 (d).

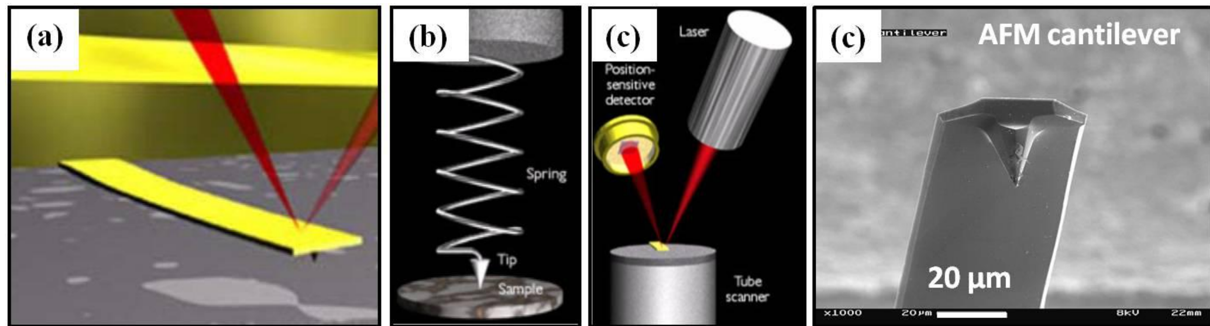

Fig. 3.2.3 Concept of AFM and the optical lever: (a) a cantilever touching a sample (b) illustration of the meaning of "spring constant" as applied to cantilevers (c) the optical lever (d) AFM cantilever image.

3.2.3 Double Crystal X-ray Diffraction (DCXRD)

X-rays are a form of electromagnetic radiation with a wavelength range from 10 to 0.01 nanometers. The wavelength must be smaller that the atomic spacing of the material being analyzed. The x-rays are created from an electron beam striking a target. The beam should be monochromatic with a very small divergence obtained by collimation.

Fig. 3.2.4. shows photograph and the schematic setup of DCXRD system (Bede D1, UK, using Cu Kα1 λ = 1.54056 Å). X-rays scatter from atoms by different degrees which are dependent on the atom type. However for a good quality x-ray beam incident on a well ordered crystalline material (such as a single crystal semiconductor) the scattered x-rays interfere with each other and result in a diffracted beam leaving the material.

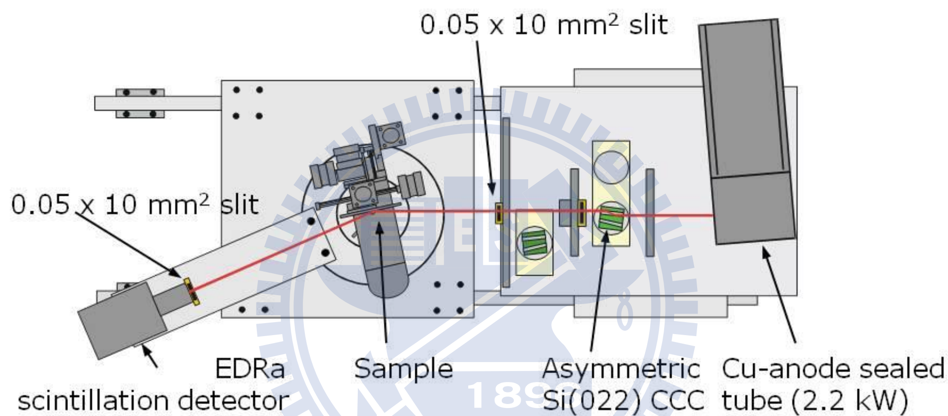

Fig. 3.2.4. The photograph and the schematic setup of DCXRD system.

This type of diffraction is caused by parallel planes of atoms, in the same way that light may be diffracted by a diffraction grating. For any given values of x-ray wavelength and angle of incidence of the x-ray beam only one set of parallel planes will cause diffraction. This is formalized in Bragg's Law which states:

$$n\lambda = 2dsin\theta \tag{3.2.1}$$

Where n is an integer value, 1, 2, 3 etc., λ is the wavelength of the x-ray beam, d is the lattice constant, the spacing between adjacent parallel planes and θ is the angle to the normal of the plane at which the x-ray beam is incident. The diffracted beam leaves the crystal plane at the same angle from the plane's normal as the incident beam, but in the opposite direction, as can be seen in the Fig. 3.2.5 (a). It shows a 'symmetric reflection', so called because the

diffracting plane is parallel to the surface of the crystal. This is the case for diffraction from the 004 plane of a standard orientation (surface is the 001 plane) semiconductor wafer.

Fig. 3.2.5 (b) shows an 'asymmetric reflection', in which the diffracting plane is not parallel to the surface of the crystal.

If the same x-ray source and beam conditioner are used then it can be safely assumed that 'λ' does not change. Each family of planes within a crystal has a characteristic and unique 'd' value. It is not possible for diffraction to occur from more than one plane if a single good quality (low divergence and approximately monochromatic) x-ray beam is used. Because of this, knowing the orientation of a wafer allows any plane to be chosen as the diffracting plane.

When an x-ray beam is fired at a crystal, and the crystal is then rotated through a small angle as observed in Fig. 3.2.6, the diffracted intensity should sharply increase from zero and then sharply decrease to zero, as the x-ray beam–crystal angle passes through the Bragg angle, 'θ'. This is commonly displayed on a 'rocking curve', which plots the angle at which the crystal is tilted against the intensity of x-rays from the crystal.

Bragg's Law above suggests that for a perfect single crystal and a good quality x-ray beam, one sharp peak should be seen only. Even with a perfect beam of x-rays, rocking curves for more complicated structures, such as the multiple quantum well laser will show multiple peaks.

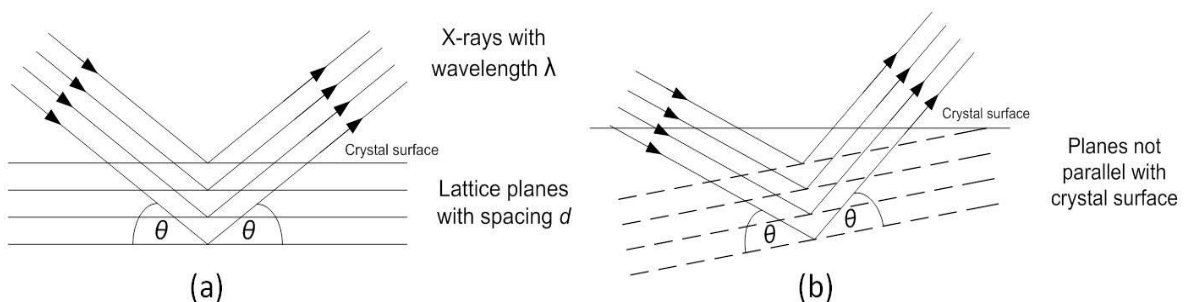

Fig. 3.2.5. Bragg diffraction from (a) a symmetric plane and (b) an asymmetric plane.

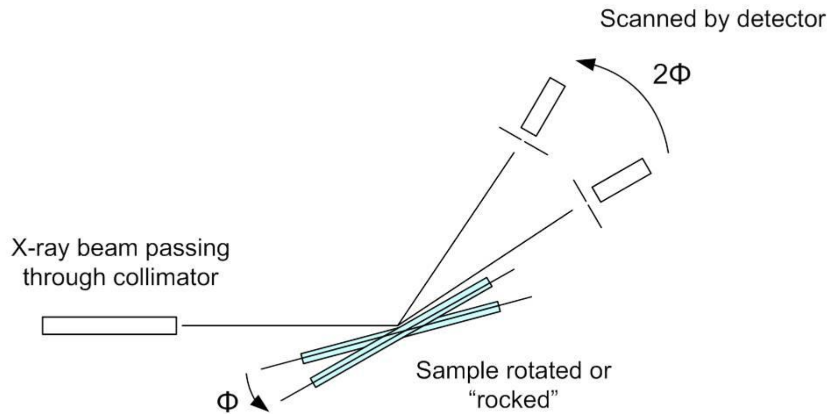

Fig. 3.2.6. Geometry for x-ray rocking curve. The angle movement for the detector is twice that of the sample.

3.2.4 Scanning Electron Microscopy (SEM)

The electron microscope uses electromagnetic lenses to focus the beam to produce an image. However, SEM and TEM differ in the way images are produced and magnified. SEM is used to view the surface or near surface of a sample, whereas TEM provides information of the internal structure of thin specimens. The scanning electron microscope as the name suggests scans across the specimen by the scan coils.

As the sample is scanned by the electron beam as shown in Fig. 3.2.7, it emits electrons and electromagnetic radiation. A detector counts the low energy secondary electrons (< 50 eV) or other radiation emitted. The image is produced by two dimensional intensity distributions by scanning a cathode ray tube (CRT) spot onto a screen and modulating the brightness by the amplified current from the detector. Three dimensional samples change the way electrons are emitted and results in the appearance of a three dimensional image. Therefore, resolutions less than 1 nm can be achieved by using SEM system.

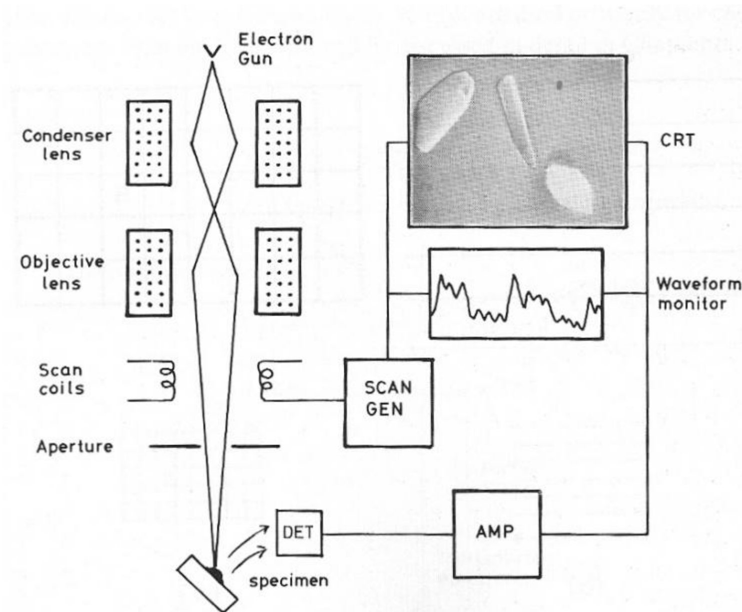

Fig. 3.2.7. Schematic diagram of a SEM.

3.2.5 Transmission Electron Microscopy (TEM)

TEM is a method of imaging where a beam of electrons are directed through a an ultra thin sample after which they are scattered into discrete diffracted beams. The diffracted electron beams are then focused in the back focal plane of the objective lens. TEM may have two modes. When operated in diffraction mode, the diffraction lens is focused on the back focal plane to produce a diffraction pattern. For the imaging mode, the diffraction lens is focused on the first image plane to produce a magnified image. In addition, the beam may be allowed to pass through the sample to obtain a bright-field image however the diffracted beams produce a dark-field image.

The ray diagram (Fig. 3.2.8) shows (a) imaging projecting a diffraction pattern and (b) projection of an image onto a viewing screen. The interaction of the electron beam with crystalline material tends to be by diffraction. The orientation of the planes of atoms in the crystal to the electron beam changes the intensity of diffraction. TEM equipment often uses a goniometer to allow the sample to be tilted to a range of angles to obtain specific diffraction

conditions. Diffracted electrons are also selected using different apertures. The intensity of diffraction is a maximum at the Bragg angle, although a variation of diffraction intensity occurs with deviation from the Bragg angle. This also depends on the thickness of the specimen. The thinner the crystal sample, the further the crystal may deviate from the Bragg condition.

When crystal planes are almost parallel to the electron beam they are close to fulfilling Bragg's Law. The majority of electrons are diffracted when the electron beam strikes one set of lattice planes exactly at their Bragg angle and only a few will pass through the sample undeviated. If the planes are exactly at the Bragg condition, strong diffraction will occur and the bright field image will appear dark. This variation with diffraction is shown with bend contours which are a feature of bending of the crystal planes. Dark contour images correspond to regions at the Bragg angle, while light contours result in the regions not strongly diffracting.

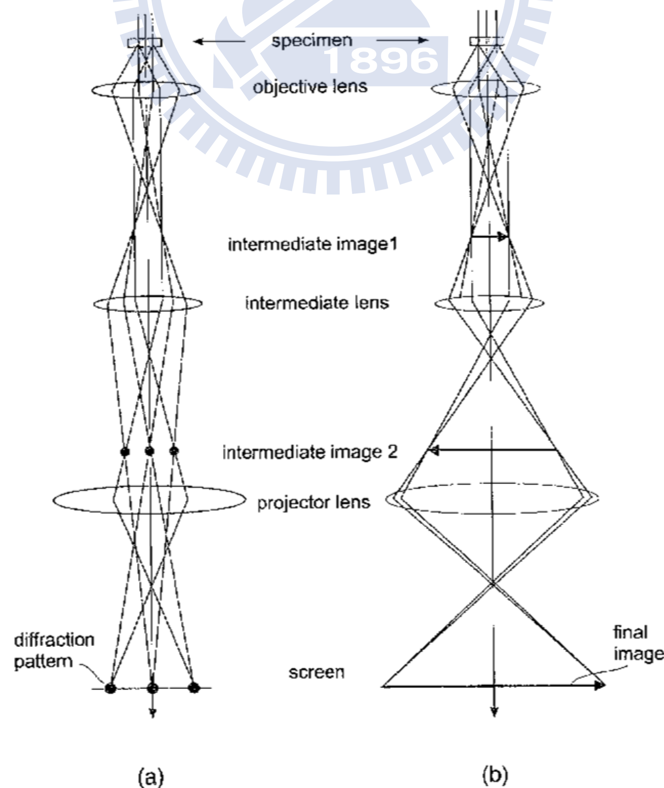

Fig. 3.2.8. Ray diagram showing two basic operations of TEM.

3.2.6 Electroluminescence (EL)

Electroluminescence (EL) is an optical and electrical phenomenon in which a material emits light in response to the passage of an electric current or under an electric field. Fig. 3.2.9 shows the schematic of electroluminescence measurement systems. A set of instruments including CW current source Kiethley 238, a microscope to observe the patterned electrode of sample surface, three axial stages for probe and fiber to detected the light output, and then the light detected by a 0.32 m monochromator (Jobin-Yvon Triax-320) with 1800, 1200, and 300 grooves/mm grating and the maximum width if the entrance slit was 1 mm. Fig. 3.2.10 shows the photograph of electroluminescence measure system.

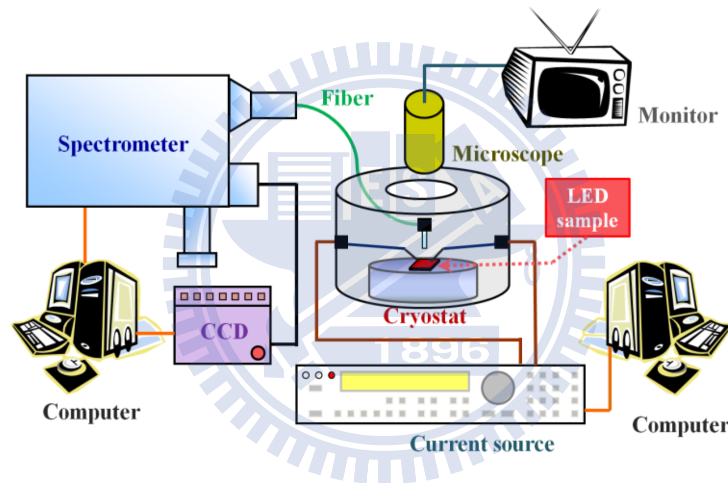

Fig. 3.2.9. The schematic of electroluminescence setup.

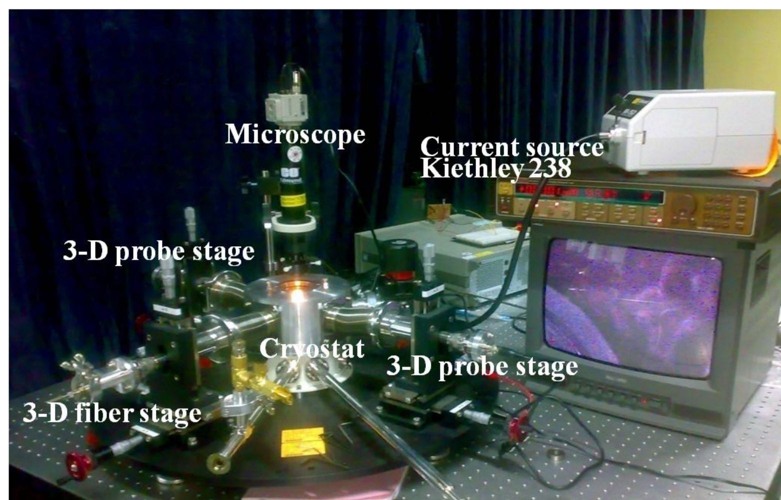

Fig. 3.2.10. The photograph of electroluminescence measure system.

3.3 Advanced Physical Models of Semiconductor Devices (APSYS)

To explore the physical origin and theoretically in this study, the numerical simulation software of APSYS (Advanced Physical Models of Semiconductor Devices) was used to predict and optimize our LEDs design in each layer. It is based on 2D/3D finite element analysis of electrical, optical and thermal properties of compound semiconductor devices. Emphasis is placed on band structure engineering and quantum mechanical effects. Inclusion of various optical modules also makes this simulation package attractive for applications involving photosensitive or light emitting devices. The APSYS simulator solves the Poisson's equation, the current continuity equations, the carrier transport equations, the quantum mechanical wave equation, and the heat transfer equations, via self-consistent manner. Built-in polarization induced by spontaneous and piezoelectric polarization is considered at hetero-interfaces of nitride related devices. We put commonly accepted physical parameters to perform the simulations. Usually, for performing a simulation, the used material parameters had been set as default data from former research results. However, we also can modify and update these values to be similar to real device. Therefore, setting suitable parameters for simulation is an important point.

3.3.1 Theoretical Model

The physical model of the InGaN MQWs is considered in such a way that the conduction bands are assumed to be decoupled from valence subbands and have isotropic parabolic bands due to the larger bandgap of nitride semiconductor and the valence band structures, which includes the coupling of the heavy-hole (HH), the light-hole (LH), and the spin-orbit split-off bands, are calculated by the 6×6 Hamiltonian with envelop function approximation. By using the basis transformation, the 6×6 Hamiltonian can be transformed into a block-diagonalized Hamiltonian [76],

$$H_{6\times6} = \begin{bmatrix} H^U & 0 \\ 0 & H^L \end{bmatrix}$$

$$with\ \ H^U = \begin{bmatrix} F & K_t & -iH_t \\ K_t & G & \Delta - iH_t \\ iH_t & \Delta + iH_t & \lambda \end{bmatrix} \ ,\ H^L = \begin{bmatrix} F & K_t & iH_t \\ K_t & G & \Delta + iH_t \\ -iH_t & \Delta - iH_t & \lambda \end{bmatrix}$$

$$F = \Delta_1 + \Delta_2 + \lambda + \theta \ ,\ G = \Delta_1 - \Delta_2 + \lambda + \theta$$

$$\lambda = \frac{\hbar^2}{2m_0}\left(A_1 {k_z}^2 + A_2 {k_t}^2\right) + \lambda_\varepsilon \ ,\ \lambda_\varepsilon = D_1 \varepsilon_{zz} + D_1\left(\varepsilon_{xx} + \varepsilon_{yy}\right) \tag{3.3.1}$$

$$K_t = \frac{\hbar^2}{2m_0} A_5 {k_t}^2 \ ,\ H_t = \frac{\hbar^2}{2m_0} A_6 k_z k_t$$

$$\Delta = \sqrt{2}\Delta_3 \ ,\ and\ \ {k_t}^2 = {k_x}^2 + {k_y}^2$$

where m_0 is the free electron mass. The A_i parameters are related to the hole effective masses. The crystal-field split energy is $\Delta_{cr} = \Delta_1$ and the spin-orbit splitting is $\Delta_{so} = 3\Delta_2 = 3\Delta_3$. The D_i parameters are deformation potential constants.

To obtain the numerical parameters required for calculations for the nitrogen-containing semiconductors, a linear interpolation between the parameters of the relevant binary semiconductors is utilized except for the unstrained bandgap energies. The material parameters of the binary semiconductors at room temperature are taken from the paper by Vurgaftman and Meyer [77] and summarized in Table 3.1.

Table 3.1. Material parameters of the binary semiconductors GaN, AlN, and InN at room temperature.

Parameter	**Symbol**	**GaN**	**AlN**	**InN**
Lattice constant	a_0 (Å)	3.189	3.112	3.545
Spin-orbit split energy	Δ_{so} (eV)	0.017	0.019	0.005
Crystal-field split energy	Δ_{cr} (meV/K)	0.010	-0.169	0.040
Hole effective mass parameter	A_1	-7.21	-3.86	-8.21

	A_2	-0.44	-0.25	-0.68
	A_3	6.68	3.58	7.57
	A_4	-3.46	-1.32	-5.23
	A_5	-3.40	-1.47	-5.11
	A_6	-4.90	-1.64	-5.96
Hydrost. deform. potential (*c*-axis)	a_z (eV)	-4.9	-3.4	-3.5
Hydrost. deform. potential (transverse)	a_t (eV)	-11.3	-11.8	-3.5
Shear deform. potential	D_1 (eV)	-3.7	-17.1	-3.7
	D_2 (eV)	4.5	7.9	4.5
	D_3 (eV)	8.2	8.8	8.2
	D_4 (eV)	-4.1	-3.9	-4.1
Elastic stiffness constant	c_{33} (GPa)	398	373	224
	c_{13} (GPa)	106	108	92
Hole effective mass (*c*-axis)	m_e^z/m_0	0.2	0.32	0.07
Hole effective mass (transverse)	m_e^t/m_0	0.2	0.30	0.07

3.3.2 Bandgap Energy of Ⅲ-Nitride Alloys

As being mentioned before, nitride-based materials are mainly made up of three binary compounds (GaN, AlN, and InN), so the bandgap energy of these nitride-based compounds is also made up of these binary materials. Besides, the bandgap energy of these three binary materials is related to the temperature. Therefore, we will extend this discussion to ternary and quaternary nitride-based compound in the next paragraph.

Temperature dependence of the bandgap energy in GaN, AlN, and InN can be expressed by the Varshni formula [78]:

$$E_g(T) = E_g(0) - \frac{\alpha T^2}{T + \beta} \quad (3.3.2)$$

where $E_g(T)$ is the bandgap energy at temperature T, $E_g(0)$ is the bandgap energy at 0 K, α and β are material-related constant, of the binary alloys are listed in Table 3.2 [77].

The bandgap energy of $In_xGa_{1-x}N$ and $Al_xGa_{1-x}N$ ternary alloys measured by Osamura et al. at room temperature (RT) is treated as [79]:

$$E_g(In_xGa_{1-x}N) = x \cdot E_g(InN) + (1-x) \cdot E_g(GaN) - bowing \cdot x \cdot (1-x)$$

$$E_g(Al_xGa_{1-x}N) = x \cdot E_g(AlN) + (1-x) \cdot E_g(GaN) - bowing \cdot x \cdot (1-x) \quad (3.3.3)$$

$$E_g(Al_xIn_{1-x}N) = x \cdot E_g(AlN) + (1-x) \cdot E_g(InN) - bowing \cdot x \cdot (1-x)$$

and the bandgap energy of $Al_xIn_yGa_zN$ quaternary alloy is [80]:

$$E_g(Al_xIn_yGa_zN) = \frac{xy\,T_{12}\left(\frac{1-x+y}{2}\right) + yz\,T_{23}\left(\frac{1-y+z}{2}\right) + xz\,T_{13}\left(\frac{1-x+z}{2}\right)}{x \cdot y + y \cdot z + z \cdot x}$$

$$z = 1 - x - y\ ,\quad T_{ij}(u) = u \cdot E_{g,j} + (1-u) \cdot E_{g,i} + bowing_{ij} \cdot u \cdot (1-u) \quad (3.3.4)$$

where “bowing” is the so-called bowing parameter (also called bowing vector), which is 7.0 eV for AlInN, 3.0 eV for InGaN, and 1.0 eV for AlGaN in our calculation, and the suffix 1, 2, and 3 is taken for AlN, InN, and GaN, respectively.

Table 3.2. Bandgap energy of GaN, AlN and InN related-temperature parameters.

Parameter	**unit**	**GaN**	**AlN**	**InN**
Eg(0 K)	eV	3.507	6.23	0.735
α	meV/K	0.909	1.799	0.245
β	K	830	1462	624

3.3.3 Band Offset Ratio of Ⅲ-Nitride Alloys

The value of band-offset, which plays a very important role in the analysis of energy band diagram, is quite significant for the design of heterostructure devices. In some other textbooks, band-offset is also called band discontinuity, and it is obvious that when two different materials are grown next to each other, the conduction and the valence bands of the two materials will become discontinuous at the interface. However, the devotion of the determination of the band-offset values in semiconductor hetero-junction from experimental measurements and theoretical calculations exist large discrepancy which may be related to different factors in the following.

(A) Technical difficulty and often indirect nature of measurements,

(B) Possible dependence of band discontinuity on detailed, conditions of interface preparation,

(C) Strain dependence of band discontinuity.

And they may be related to the difficulty of obtaining high equality epitaxial films.

The conduction band offset ratio ($\Delta E_c/\Delta E_g$) for the AlN/GaN interface is between 0.66 and 0.81 according to the recent calculations [81].

3.3.4 Carrier Transportation in Ⅲ-Nitride Alloys

The physical model of carrier transport is the traditional drift-diffusion model for semiconductors. The specific equations can be expressed as:

$$\overrightarrow{J_n} = q\mu_n n\,\vec{F} + qD_n \nabla n \;\; (for\ electrons)$$

$$,and \qquad \overrightarrow{J_p} = q\mu_p p\,\vec{F} + qD_p \nabla p \;\; (for\ holes) \qquad (3.3.5)$$

where n and p are the electron and hole concentrations, $\overrightarrow{J_n}$ and $\overrightarrow{J_p}$ are the current densities of electrons and holes, $\vec{F}$ is the electrostatic field, μ_n and μ_p are the mobilities of electrons and

holes. The diffusion constants D_n and D_p are replaced by mobilities using the Einstein relation $D = \mu k_B T/\mathrm{q}$. The equations used to describe the semiconductor device behavior are Poisson's equation,

$$\nabla \cdot \left(\varepsilon_0 \varepsilon \vec{F}\right) = \mathrm{q}\left(p - n + p_D - n_A \pm N_f\right) \tag{3.3.6}$$

and the current continuity equations for electrons and holes,

$$\frac{1}{\mathrm{q}} \nabla \cdot \overrightarrow{J_n} - R_n + G_n = \frac{\partial n}{\partial t} \quad \text{(for electrons)}$$

$$\frac{1}{\mathrm{q}} \nabla \cdot \overrightarrow{J_p} - R_p + G_p = \frac{\partial p}{\partial t} \quad \text{(for holes)} \tag{3.3.7}$$

where ε is the relative permittivity. G_n and R_n are the generation rates and recombination rates for electrons, G_p and R_p are the generation rates and recombination rates for holes, respectively. The electric field is affected by the charge distribution, including the electron and hole concentrations, dopant ions p_D and n_A, and other fixed charges N_f that are of special importance in nitride-based devices due to the effect of built-in polarization.

Built-in polarization induced due to spontaneous and piezoelectric polarization is known to influence the performance of nitride devices. In order to consider the built-in polarization within the interfaces of nitride devices, the method developed by Fiorentini et al. is employed to estimate the built-in polarization, which is represented by fixed interface charges at each hetero interface. They provided explicit rules to calculate the nonlinear polarization for nitride alloys of arbitrary composition [82].

Although the interface charges can be obtained by this theoretical model, experimental investigations often find weaker built-in polarization than that predicted by theoretical calculation. It is mainly attributed to partial compensation of the built-in polarization by defect and interface charges [83]. Typical reported experimental values are of 20 %, 50 % or

80 % smaller than the theoretically calculated values [84]. As a result, 50 % of the theoretical polarization values are used in our simulation from the average of the reported values.

A widely used empirical expression for modeling the mobility of electrons and holes is the Caughey Thomas approximation, which is employed in our calculation and can be expressed as [85]:

$$\mu(N) = \mu_{min} + \frac{\mu_{max} - \mu_{min}}{1 + \left(\frac{N}{N_{ref}}\right)^{\alpha}} \tag{3.3.8}$$

where μ_{max}, μ_{min}, N_{ref} and α are fitting parameters. The parameter μ_{max} represents the mobility of undoped or unintentionally doped samples, where lattice scattering is the main scattering mechanism, while μ_{min} is the mobility in highly doped material, where impurity scattering is dominant. The parameter α is a measure of how quickly the mobility changes from μ_{min} to μ_{max} and N_{ref} is the carrier concentration at which the mobility is half way between μ_{min} and μ_{max}. The electron mobility of $Ga_{1-x-y}Al_xIn_yN$ in our simulation can be expressed as:

$$\mu_{\mathrm{min}}\,(\mathrm{Ga_{1-x-y}Al_xIn_yN}) = (1 - \mathrm{x} - \mathrm{y}) * \mu_{\mathrm{min}}\,(\mathrm{GaN}) + \mathrm{x} * \mu_{\mathrm{min}}\,(\mathrm{AlN}) + \mathrm{y} * \mu_{\mathrm{min}}\,(\mathrm{InN})$$

$$\mu_{\mathrm{max}}\,(\mathrm{Ga_{1-x-y}Al_xIn_yN}) = (1 - \mathrm{x} - \mathrm{y}) * \mu_{\mathrm{max}}\,(\mathrm{GaN}) + \mathrm{x} * \mu_{\mathrm{max}}\,(\mathrm{AlN}) + \mathrm{y} * \mu_{\mathrm{max}}\,(\mathrm{InN}) \tag{3.3.9}$$

The relative parameters are summarized in Table 3.3 [86].

Table 3.3. Mobility parameters of GaN, AlN and InN.

Parameter (unit)	**Electrons**
N_{ref} (cm^{-3})	1.0*10^{17}
$\boldsymbol{\alpha}$	1.37
GaN ; InN	
μ_{max} ($\mathrm{cm}^2\mathrm{V}^{-1}\mathrm{s}^{-1}$)	684
μ_{min} ($\mathrm{cm}^2\mathrm{V}^{-1}\mathrm{s}^{-1}$)	386
AlN	
μ_{max} ($\mathrm{cm}^2\mathrm{V}^{-1}\mathrm{s}^{-1}$)	306
μ_{min} ($\mathrm{cm}^2\mathrm{V}^{-1}\mathrm{s}^{-1}$)	132

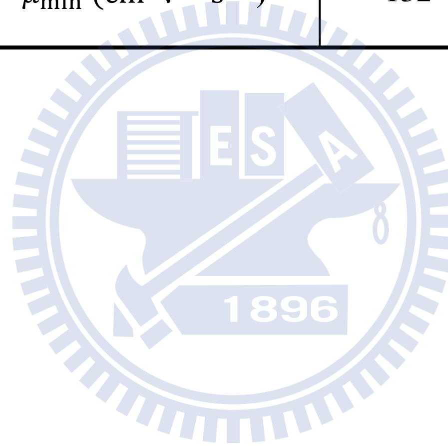

Chapter 4

Investigation of Efficiency Droop for InGaN-Based Near-UV Light-Emitting Diodes with InAlGaN Barrier

4.1 Introduction

GaN-based near-ultraviolet light emitting devices (LEDs) have attracted great attention in last few years due to its potential applications in photo-catalytic deodorizing such as air conditioner, biological, medical and environmental instrumentation, resin curing, UV light source, and there have been interests in solid-state lighting by using near-UV LEDs light for the phosphor-converting source, as we mentioned of the applications in Chap. 1.

However, it is difficult to fabricate near-UV LEDs with high efficiency, because the internal quantum efficiency (IQE) decreases drastically under the low indium composition [30][87, 88]. Moreover, crystalline quality and light absorption of GaN are significant for short wavelength near-UV LEDs [89, 90]. It's well known that in low indium content InGaN based-quantum wells, AlGaN barrier is necessary for carrier confinement. But the two materials of AlGaN and InGaN are very different in growth temperature which affects strongly on the quality of material and device performances.

In this study, we demonstrate high efficient near-UV LEDs by replacing AlGaN by InAlGaN barrier in active region. Furthermore, the efficiency droop characteristics and optical properties of high efficient near-UV LEDs have been measured and investigated by APSYS.

4.2 Sample Structures and Fabrication Methods

All samples used in this study were grown on 2-inch c-plane (0001) sapphire substrates using an atmospheric-pressure metal organic chemical vapor deposition (AP-MOCVD) in a Taiyo Nippon Sanso SR4000 reactor system.

Prior to the growth, we heated the sapphire substrate to 1150 ℃ in H_2 ambient to remove surface contamination. For the growth of GaN-based LEDs, trimethyl gallium (TMGa), trimethyl indium (TMIn), trimethyl aluminum (TMAl), and ammonia (NH_3) were used as the source precursors for Ga, In, Al, and N, respectively. Silane (SiH_4) and bis-cyclopentadienyl magnesium (Cp_2Mg) were used as n-type and p-type dopants.

The conventional structure is as follows. A 500 ℃ low temperature (LT) 30-nm-thick GaN nucleation layer was deposited, followed by a 1-μm-thick un-doped GaN layer and a 2.5-μm-thick n-type $Al_{0.02}Ga_{0.98}N$ layer grown at 1150 ℃. A ten-period InGaN/AlGaN multi-quantum-well (MQW) active region was grown at 830 ℃. Subsequently, a 15-nm-thick Mg-doped $Al_{0.3}Ga_{0.7}N$ and a 10-nm-thick Mg-doped $Al_{0.1}Ga_{0.9}N$ electron-blocking layers (EBL) were grown at 1050 ℃, followed by a 60-nm-thick Mg-doped GaN contact layer grown at 1030 ℃.

The quaternary structure of InGaN/InAlGaN MQW was almost identical to that of the InGaN/AlGaN MQW LED, the only difference was that we used InAlGaN instead of AlGaN as the barrier layers in the active region. Here, the MQW active region consisted of ten periods of 2.6-nm-thick un-doped $In_{0.025}Ga_{0.975}N$ well layers and 11.7-nm-thick Si-doped $In_{0.0085}Al_{0.1112}Ga_{0.8803}N$ or $Al_{0.08}Ga_{0.92}N$ quantum barrier layers growth on n-$Al_{0.02}Ga_{0.98}N$/ud-GaN/Sapphire.

In additions, the growth time of quantum well and barrier were 79 sec and 380 sec, respectively. Therefore, the growth rate of quantum well and barrier were 0.329 Å /s and 0.308 Å /s. The schematic of InGaN/AlGaN and InGaN/InAlGaN MQWs structure are shown in Fig. 4.2.1.

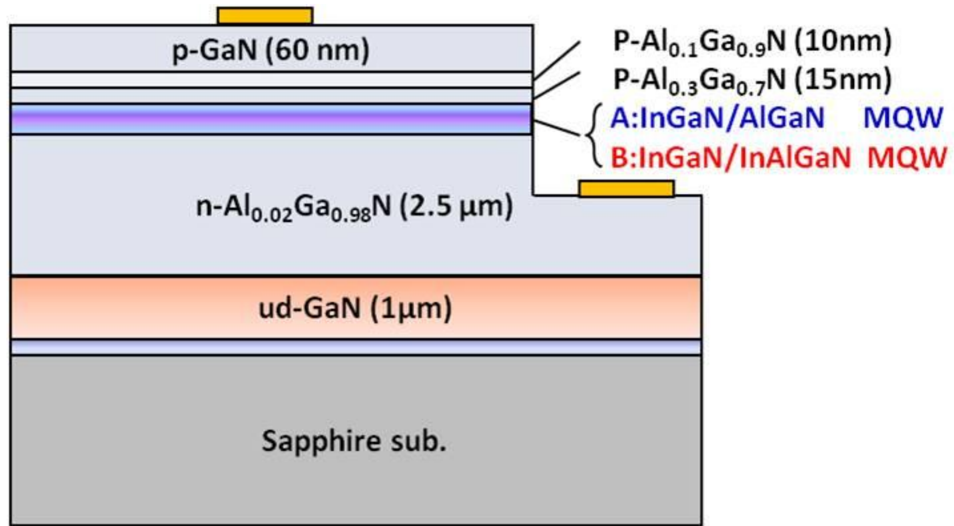

Fig. 4.2.1. Schematic of InGaN/AlGaN and InGaN/InAlGaN MQWs structures.

During the growth of barriers, we kept the flow rates of TMGa, NH_3 and SiH_4 at 12.24 µmol/min, 0.67 mol/min, and 0.196 nmol/min. For the growth of InAlGaN, we added the flow rate of TMIn for 0.79 µmol/min and increased the flow rate of TMAl from 1.94 µmol/min to 2.13 µmol/min, compared to AlGaN barrier. All the detail conditions during MOCVD growth such as temperature, time, gas flow (TMGa, TMIn, TMAl, NH_3, and SiH_4), thickness, and growth rate as summarized in Table 4.1.

Table 4.1. Growth parameters of the InAlGaN, AlGaN, and InGaN MQWs.

	Temp.	Time	TMGa	TMIn	TMAl	NH3	SiH4	Thickness	GR
	(°C)	(sec)	(µmol/min)	(µmol/min)	(µmol/min)	(mol/min)	(nmol/min)	(nm)	(Å/s)
InAlGaN	830	380	12.24	0.79	2.13	0.67	0.196	11.7	0.308
AlGaN	830	380	12.24	0	1.94	0.67	0.196	11.7	0.308
InGaN	830	79	12.24	16.75	0	0.67	0	2.6	0.329

To probe the detailed properties of epitaxial layers, a 50-nm AlGaN and InAlGaN single heteroepitaxial layers were also deposited on n-AlGaN/ud-GaN/Sapphire substrate. The schematic of AlGaN and InAlGaN single heteroepitaxial layers are shown in Fig. 4.2.2.

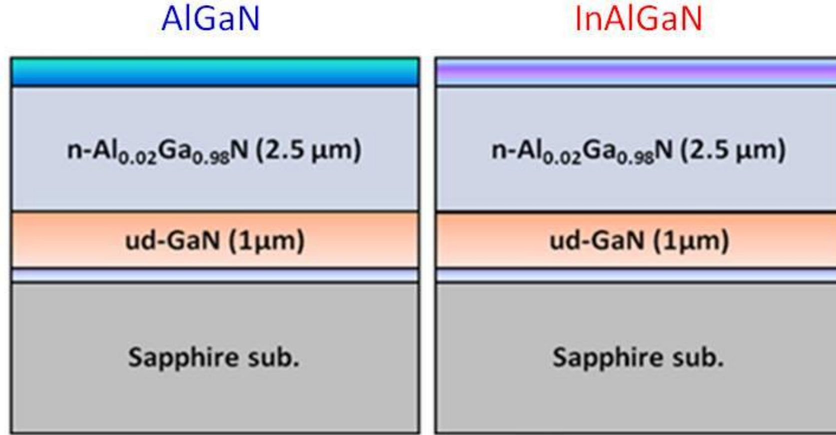

Fig. 4.2.2. Schematic of AlGaN and InAlGaN single heteroepitaxial layers.

The mole fractions of Al and In in MQWs were identified by High-resolution double crystal x-ray diffraction (DCXRD, Bede D1, UK) using Cu Kα1 (λ = 1.54056 Å) as source. These samples were also characterized by photoluminescence (PL), atomic force microscopy (AFM) and transmission electron microscopy (TEM) to reveal the optical property, surface morphology and MQWs structure, respectively.

Finally, the UV LED wafers were processed into mesa-type chips (size: 1mm×1mm) and packaged on epoxy-free metal cans (TO-66, thermal resistance (R_θ) ~ 2 K/W). The output power of the UV LED was measured using an integrated sphere detector and tested at room temperature with currents up to 1 A. Testing is done in pulsed mode with 100 µs pulses and a 1 % duty cycle to prevent self-heating, because the thermal time constant of the LEDs is in the millisecond range [91]. In this paper, the optical and electrical properties of InGaN/InAlGaN and conventional InGaN/AlGaN MQW LEDs are numerically calculated using the APSYS simulation software [92].

4.3 Investigation of Optical Property and Surface Morphology

4.3.1 Optical Properties

PL spectra of AlGaN and InAlGaN single heteroepitaxial layers grown on

n-AlGaN/ud-GaN/Sapphire substrate were obtained at a room temperature to investigate the band edge emission. Fig. 4.3.1 shows that the PL emission energy of these two samples are very close (about 3.594 eV) and the peak intensity of InAlGaN is slightly higher than AlGaN. The strong PL emission is attributed to the better crystal quality [93].

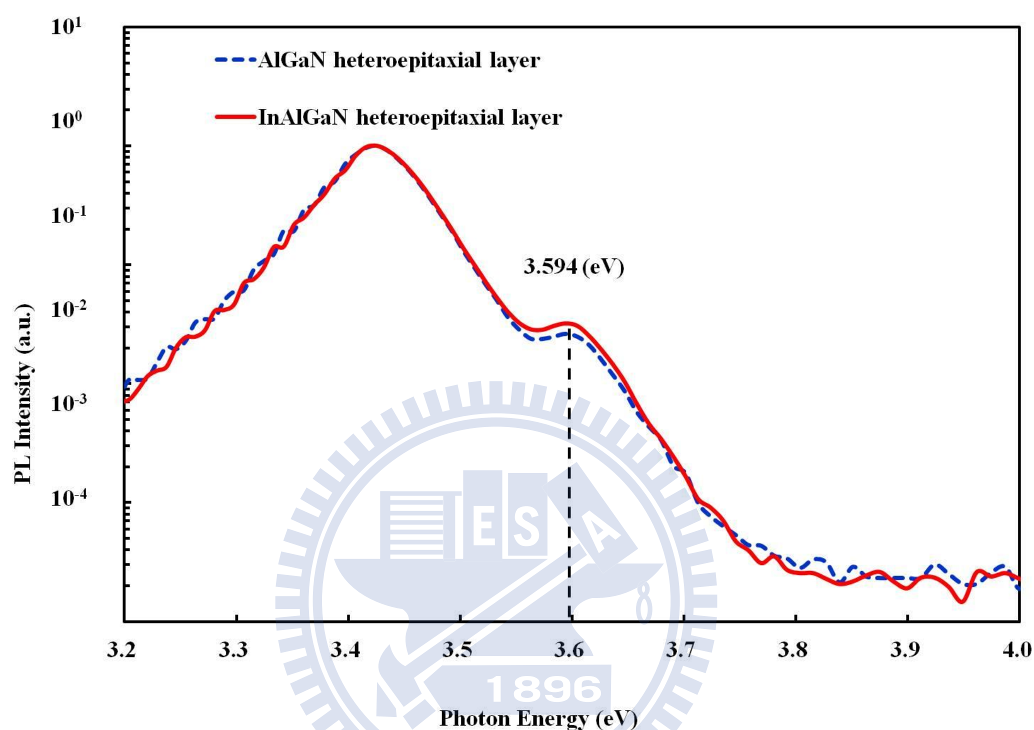

Fig. 4.3.1. Room-temperature PL spectra of AlGaN and InAlGaN single heteroepitaxial layers.

4.3.2 Surface Morphology

Fig. 4.3.2 shows the surface morphology of the two AlGaN and InAlGaN single heteroepitaxial layers with the same thickness about 50-nm. The root-mean-square (RMS) roughness measured by AFM is about 0.813 nm and 0.595 nm, respectively. The relatively high roughness of AlGaN single heteroepitaxial layer can mainly be attributed to the low deposition temperature of 830℃ necessary for the adjacent InGaN well.

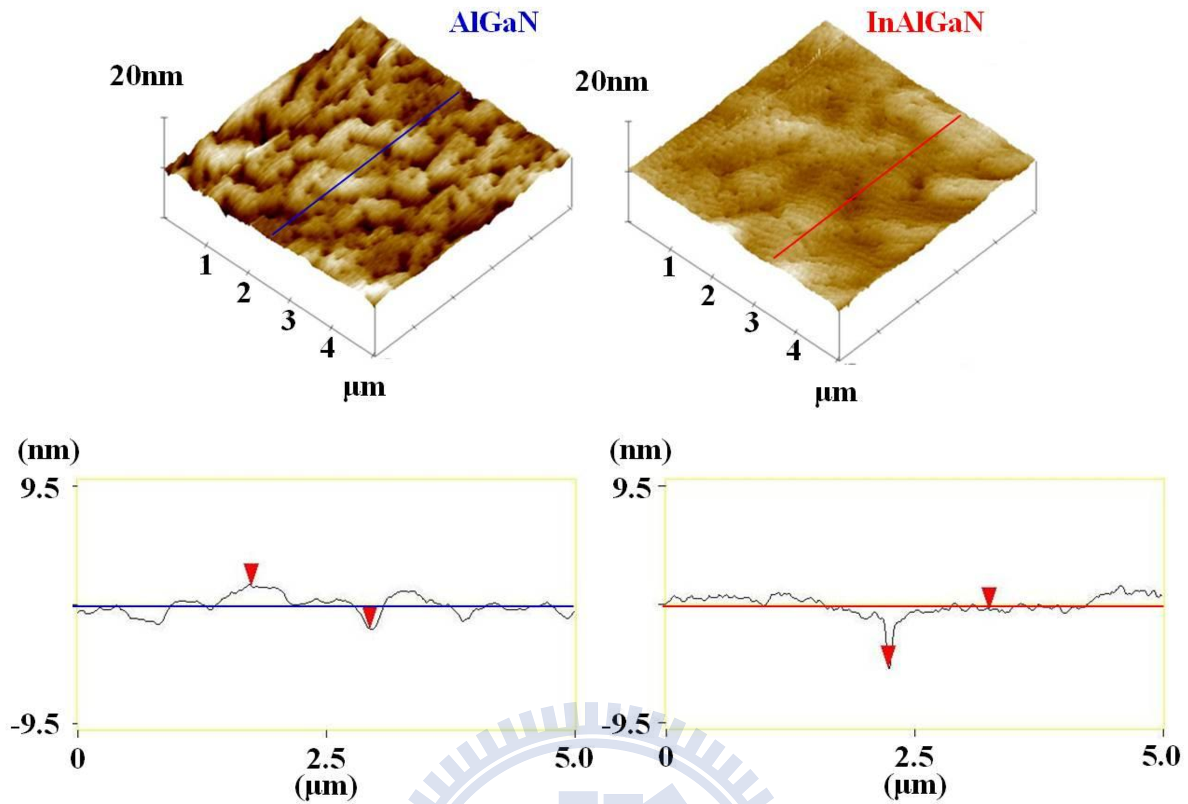

Fig. 4.3.2. Shows surface morphology AFM over 5×5 µm2 of AlGaN (RMS:0.813 nm) and InAlGaN (RMS:0.595 nm) layer with thickness about 50 nm.

To compare the different morphology in surface, a 50-nm GaN single heteroepitaxial layer was also deposited on n-AlGaN/ud-GaN/Sapphire substrate. These single heteroepitaxial layers were grown at a low temperature (LT) 830 ℃ for In incorporation in adjacent quantum well.

Pit topography and surface morphology can be observed from top-view AFM images. As shown in Fig. 4.3.3, the dimension of each pit in GaN and AlGaN is slightly larger than in InAlGaN layer. The relatively small pits of LT InAlGaN layer can mainly be attributed to the smaller tensile strain in LT AlGaN or LT GaN by inserting the isoelectronic In atoms. Experiments have shown that the presence of In leads to a smooth morphology with better crystal quality and optical properties, and this result is due to the interaction between In atoms and screw dislocations [94].

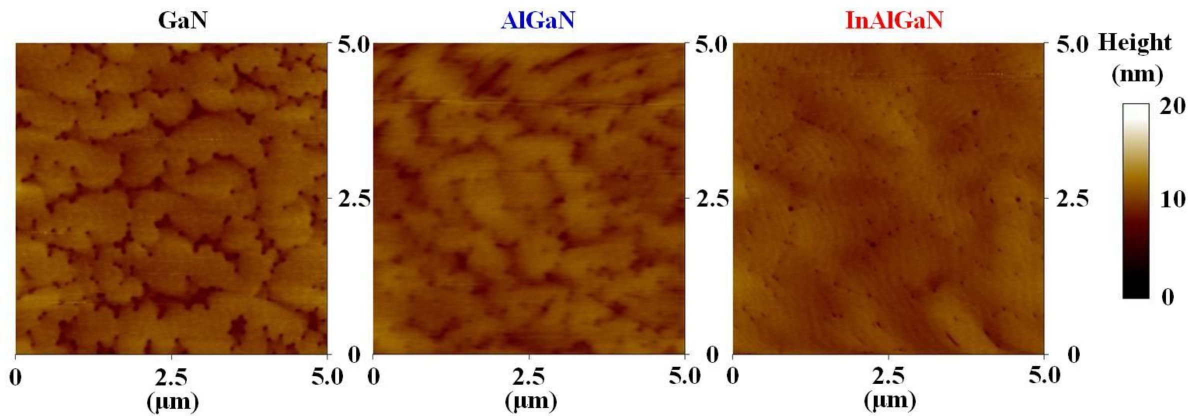

Fig. 4.3.3. Surface morphology of top-view AFM images over 5×5 μm^2 of LT GaN, AlGaN, and InAlGaN layer.

4.3.3 Compositions and Thicknesses Analysis

To investigate the lattice and mole fractions of Al and In in GaN-based MQWs, these samples of heteroepitaxial layers and devices were identified by High-resolution double crystal x-ray diffraction (XRD).

Fig. 4.3.4 shows the HRXRD (ω-2θ) curves in the (004) and (105) reflections of GaN, AlGaN, and InAlGaN single heteroepitaxial layers. The results show that the locations of right side peaks of AlGaN and InAlGaN layers are very close. It proves that the lattices in those two samples of ternary and quaternary material are matched. It is worth mentioning for the asymmetric spectrum in the center. This is because the single heteroepitaxial layers are grown on an n-AlGaN/ud-GaN/Sapphire substrate, and the peak in center and the merged peak around -300 arcsec indicate the 2.5-μm $Al_{0.02}Ga_{0.98}N$ and 1-μm GaN, respectively.

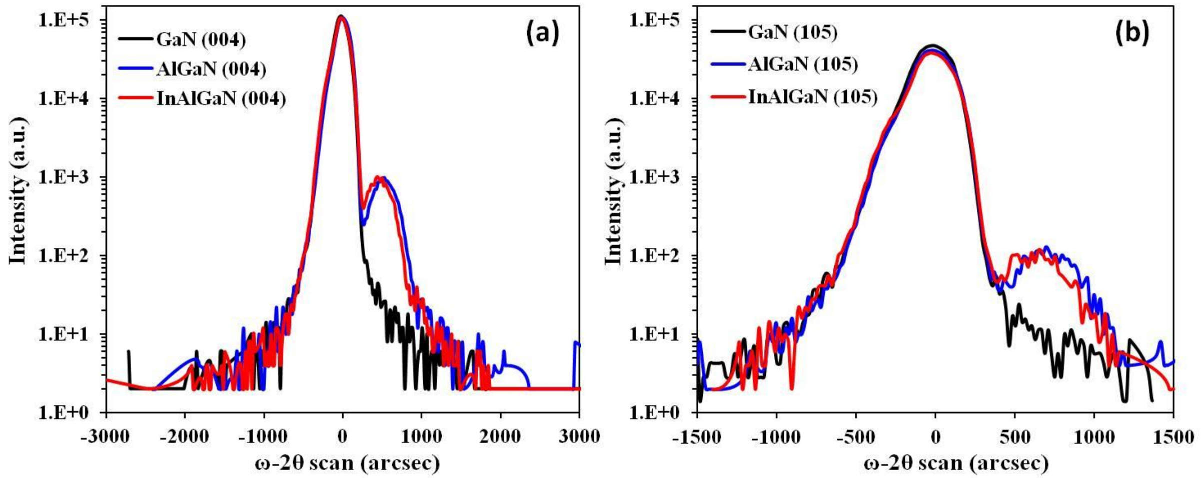

Fig. 4.3.4. HRXRD (ω-2θ) curves in the (a) (004) and (b) (105) reflections of GaN, AlGaN, and InAlGaN single heteroepitaxial layers.

Further study in lattice matched, Fig 4.3.5 shows the HRXRD (105) reflection of Reciprocal Space Map (RSM) for (a) GaN, (b) AlGaN, and (c) InAlGaN single heteroepitaxial layers. The results show lattices matched in x-plane and z-direction between AlGaN and InAlGaN layer, and this indicate that the influence in quantum well of total polarization from ternary and quaternary barrier will be the same value.

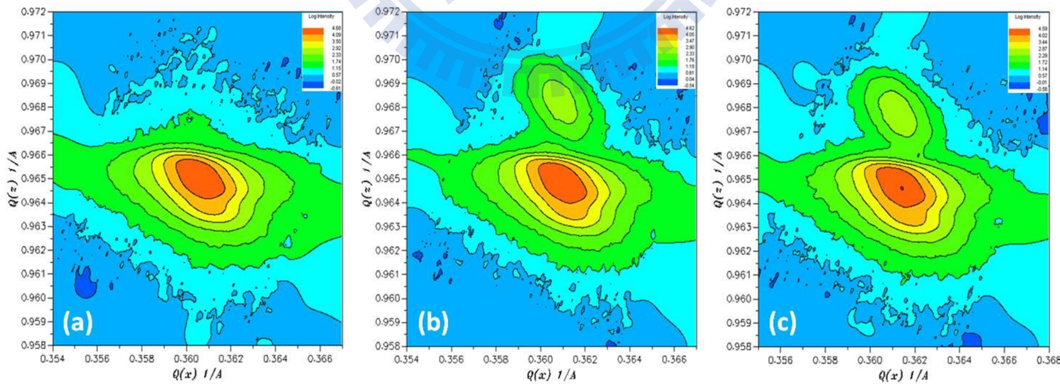

Fig. 4.3.5. HRXRD (105) RSM of GaN, AlGaN, and InAlGaN single heteroepitaxial layers.

Fig. 4.3.6 shows the HRXRD (ω-2θ) curves in the (002) reflections of InGaN/AlGaN and InGaN/InAlGaN MQWs. The results show that the locations of multiple satellite peaks of InGaN/AlGaN and InGaN/InAlGaN MQWs are very close. This indicates that the thickness

of barrier layer in these two samples is matched, and it is quite consistent with the measured values of 11.7 nm from HRTEM images as shown in Fig. 4.3.7 (a) and Fig. 4.3.7 (b). In addition to experimentally estimate the Indium and Aluminum composition in the MQWs, we simulate the HRXRD (ω-2θ) curve by using dynamical diffraction theory. The In composition in the QWs was determined to be about 2.5 %, where the thickness of the well was about 2.6 nm. The compositions of ternary and quaternary barriers were $Al_{0.08}Ga_{0.92}N$ and $In_{0.0085}Al_{0.1112}Ga_{0.8803}N$, respectively. Besides, the growth rates of well and barrier were estimated about 0.329 and 0.308 Å /s, respectively.

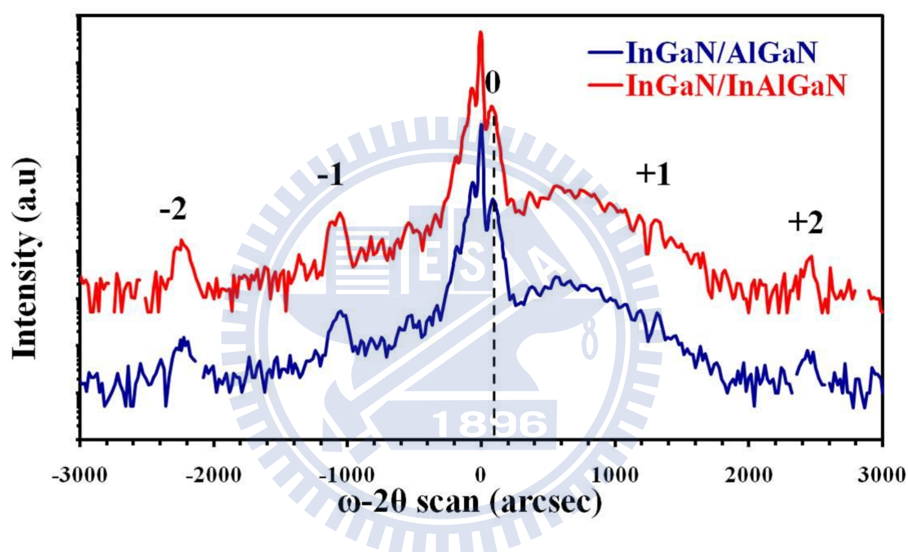

Fig. 4.3.6. HRXRD (ω-2θ) curves in the (002) reflections of InGaN/AlGaN and InGaN/InAlGaN MQWs.

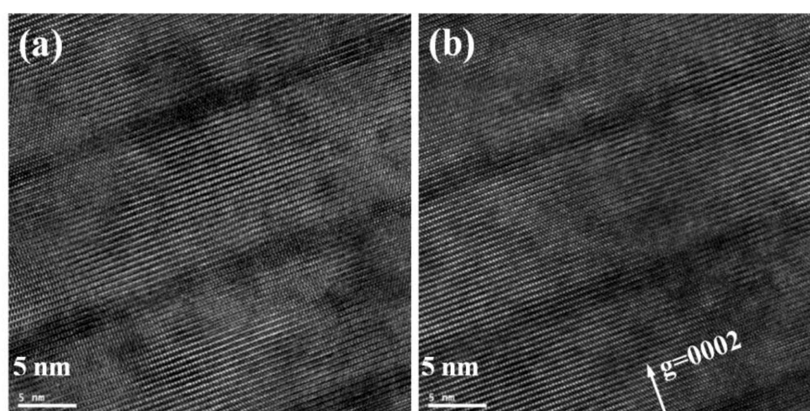

Fig. 4.3.7. Cross-sectional TEM images of (a) InGaN/AlGaN and (b) InGaN/InAlGaN MQWs. The diffraction condition is g0002.

Fig. 4.3.8 shows the Cross-sectional TEM images of (a) InGaN/AlGaN and (b) InGaN/InAlGaN fully LED structures. Inset in Fig. 4.3.8 shows ternary and quaternary MQWs structure. According to the TEM images, we can observe the thickness and interface of each layer.

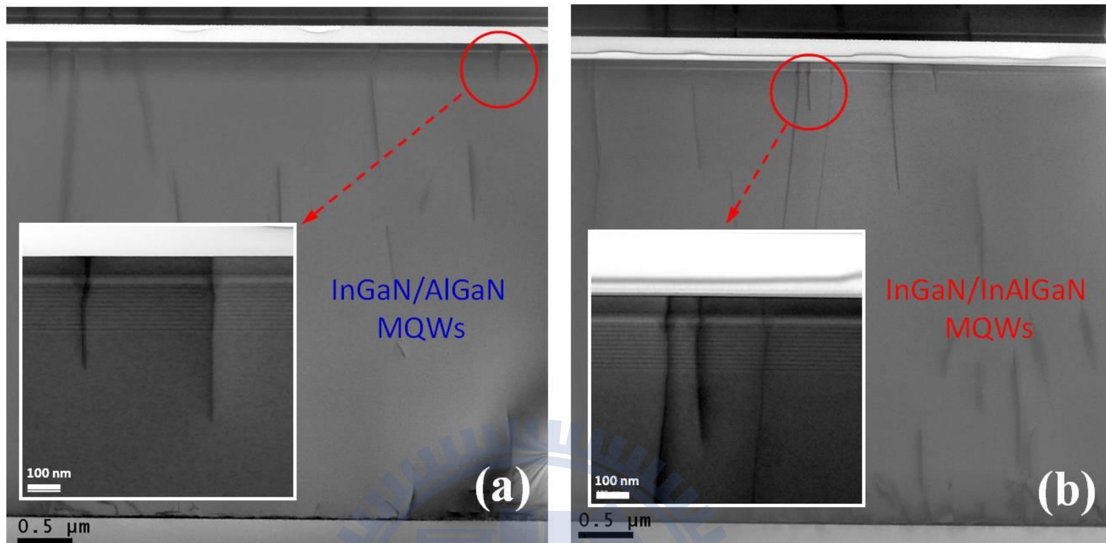

Fig. 4.3.8. Cross-sectional TEM images of (a) InGaN/AlGaN and (b) InGaN/InAlGaN LED structures. Inset in Fig. 4.3.8 shows ternary and quaternary MQWs structure.

4.4 Current-dependent Intensity and Efficiency

Fig. 4.4.1 (a) shows the optical microscope (OM) image of 2-inch near-UV LED epi-wafer under 100 mA operated at room temperature. Then, the wafers were processed into mesa-type chips (size: 1mm×1mm), and the processes include steps: (1) definition of mesa area, (2) etching untial n-AlGaN exposed, (3) deposition of transparent contact layer (ITO), (4) deposition of n and p contact, (5) passivating by SiO_2, (6) thinning, and (7) dicing. The chip image is shown in Fig. 4.4.1 (b), and OM image of the chip under 350 mA driving current is shown in Fig. 4.4.1 (c).

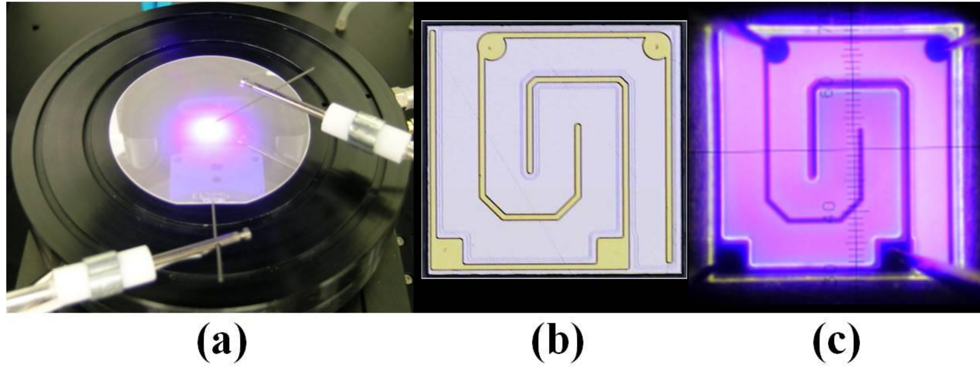

Fig. 4.4.1. (a) 2-inch near-UV LED epi-wafer under 100 mA, (b) the mesa-type near-UV chip and (c) chip image under 350 mA driving current.

Fig. 4.4.2 shows the optical properties of light output power–current–voltage (L-I-V) characteristics for the AlGaN and InAlGaN barrier near-UV LEDs. The forward voltage was 3.89 and 3.98 V for InGaN/AlGaN and InGaN/InAlGaN MQWs near-UV LED at a forward current of 350 mA, respectively. A little high forward voltage of InAlGaN barrier LED can be attributed to the higher Al content compare to the AlGaN barrier, thus increase the series resistance in the device. The light output power of InGaN-based near-UV LED with the InAlGaN barrier is higher by 25 % and 55 % than the AlGaN barrier at 350 mA and 1000 mA, respectively.

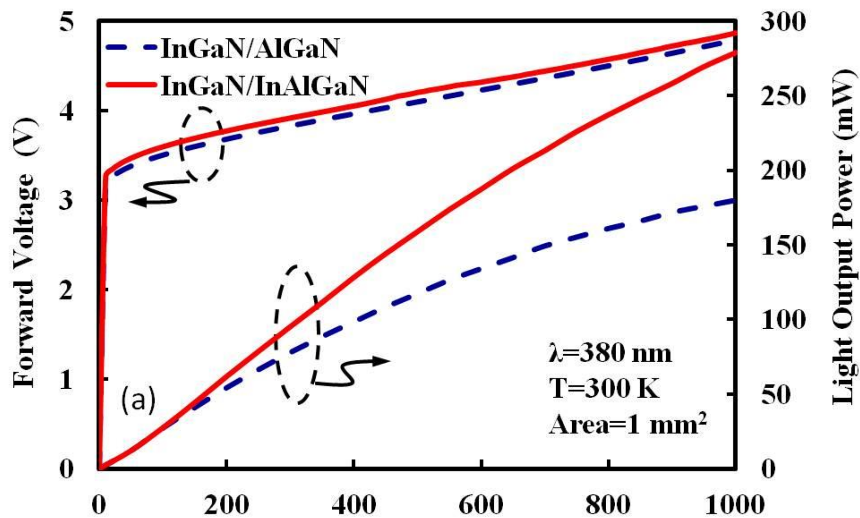

Fig. 4.4.2. L-I-V curves of the LEDs with AlGaN (dash) and InAlGaN (solid) barrier.

Fig. 4.4.3 shows the normalized efficiency curves of experimental (open circles) and simulated (solid lines) as a function of forward current for the two samples. For the InGaN/AlGaN near-UV LEDs, when the injection current exceeds 1000 mA, the efficiency is reduced to 66 % of its maximum value. In contrast, InGaN/InAlGaN near-UV LEDs exhibit only 13 % efficiency droop when we increase the injection current to 1000 mA. The reduction of efficiency droop is quite clear and the current at maximum efficiency shifts from 150 to 400 mA.

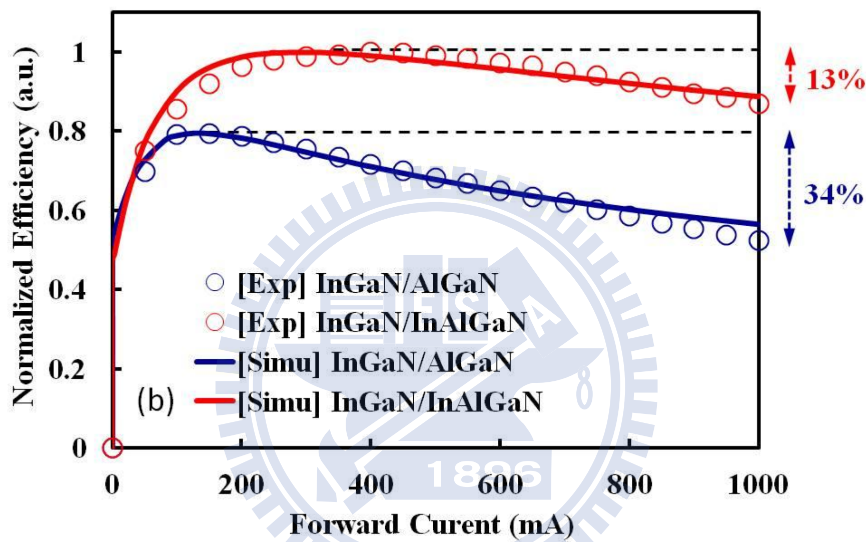

Fig. 4.4.3. Normalized Efficiency curves of experimental (open circles) and simulated (solid lines).

Besides, the wavelength is nearly constant about 380 nm over the entire current range. Fig. 4.4.4 shows the EL spectra of the near-UV LEDs at increasing continuous wave (CW) and pulsed currents. In CW mode as shown in Fig. 4.4.4 (a) InGaN/AlGaN MQWs and (b) InGAN/InAlGaN MQWs, the peak is initially located at ~3.26 eV (380 nm) and it exhibits a noticeable red shift due to self-heating effects. In contrast, the LED in pulse mode was driven up to 1000 mA, corresponding to a current density of ~100A/cm^2. The pulsed current-dependent spectra are shown in Fig. 4.4.4 (c) InGaN/AlGaN MQWs and (d) InGAN/InAlGaN MQWs. The peak energy is nearly constant over the entire current range.

The absence of temperature-induced red shift suggests that self-heating is substantially suppressed. Another noticeable fact is that the peak wavelength of pulsed mode is almost the same as the one at low current density (~ 10A/cm2) in CW mode, which further supports our assumption. Therefore, we can reasonable believe that the junction temperature of the device during operation is close to room temperature. The similar result for preventing self-heating by pulsed mode is shown in Ref 71. The absence of temperature-induced red shift suggests that self-heating is substantially suppressed by using metal type packaging and pulsed mode operating [71].

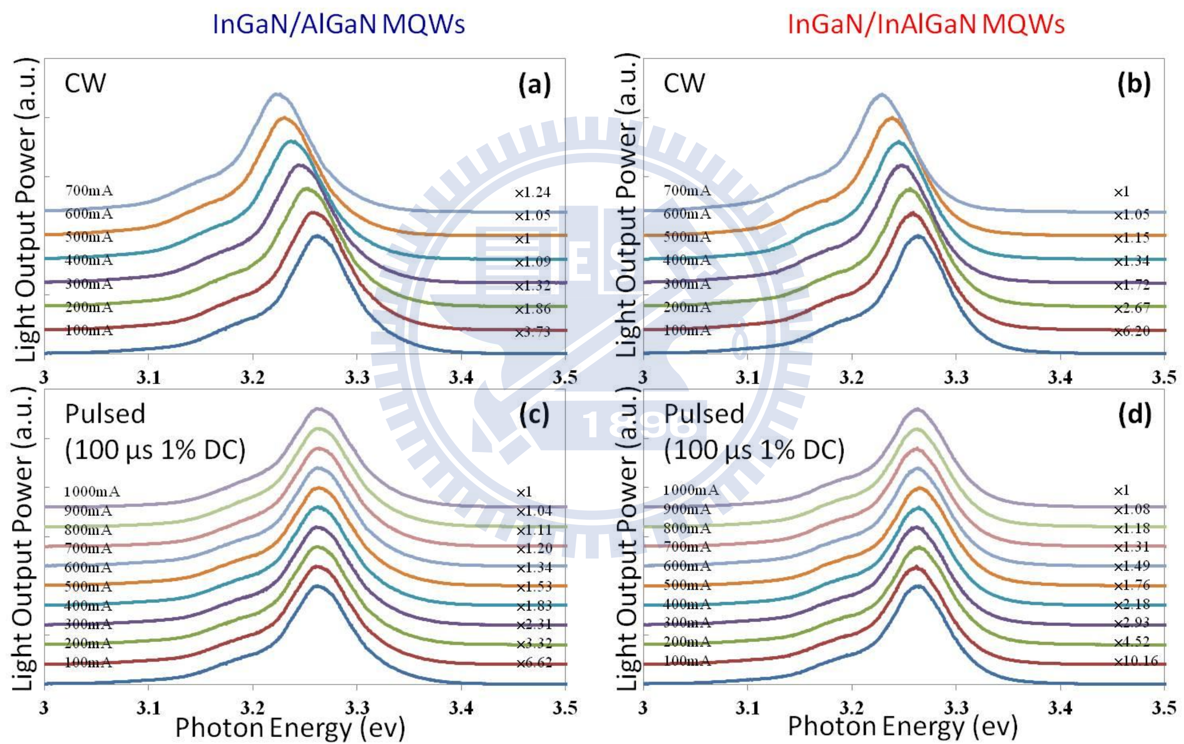

Fig. 4.4.4. EL spectra for InGaN/AlGaN and InGAN/InAlGaN MQWs under (a) (b) CW current and (c) (d) pulsed current with 100 μs and a 1 % duty cycle.

It is worth mentioning for the different blue shift level of EL between near-UV and green (or blue) LED as shown in Fig. 4.4.5 [71]. Fig. 4.4.5 shows the peak energies of the near-UV and green LEDs as a function of the CW and pulsed modes for different duty cycles of 0.1 %, 0.2 %, 1 %, and 2 %.

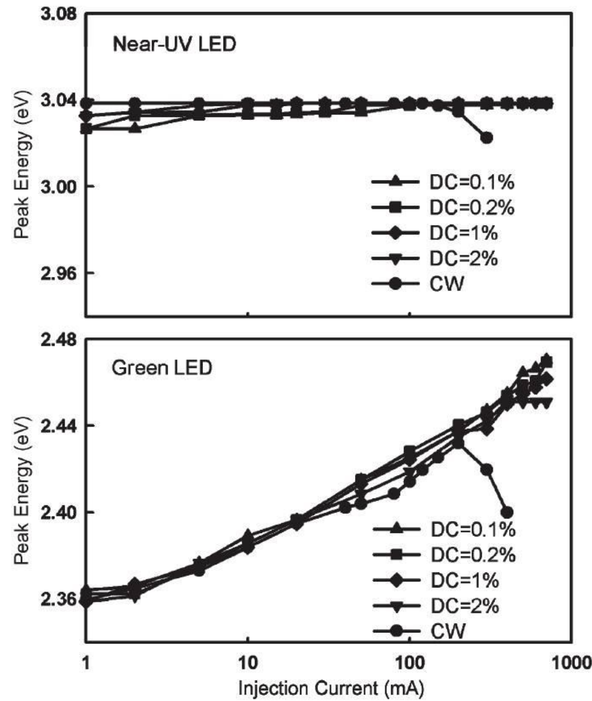

Fig. 4.4.5. EL peak energy of the (top) near-UV and (bottom) green LEDs as a function of the CW and pulsed modes.

The peak energy shift of the near-UV LED (~409 nm) that is over the entire current range is minimal (∼10 meV) under pulsed injection for all duty cycles, whereas the CW injection above 200 mA leads to a significant amount of red shift. Similar peak energy evolution has been observed for the UV LED (~369 nm). In contrast, the EL peaks of the green (~519nm) LED shows a large amount of blue shift with increasing injection current from 1 mA to 900mA, as shown at the bottom part of Fig. 4.4.5.

The total amount of peak shift decreases as the In content in the active region decreases as shown in Fig. 4.4.6 [71].

The large current-induced blue shift of EL is one characteristic feature of the InGaN-based green and blue LEDs with relatively high In mole fractions in the QWs. It occurs because of the band filling of localized states resulting from the compositional or thickness fluctuation of InGaN QWs. The screening of the piezoelectric field in the QWs by the injected carriers would also lead to a blue shift of the emission peak.

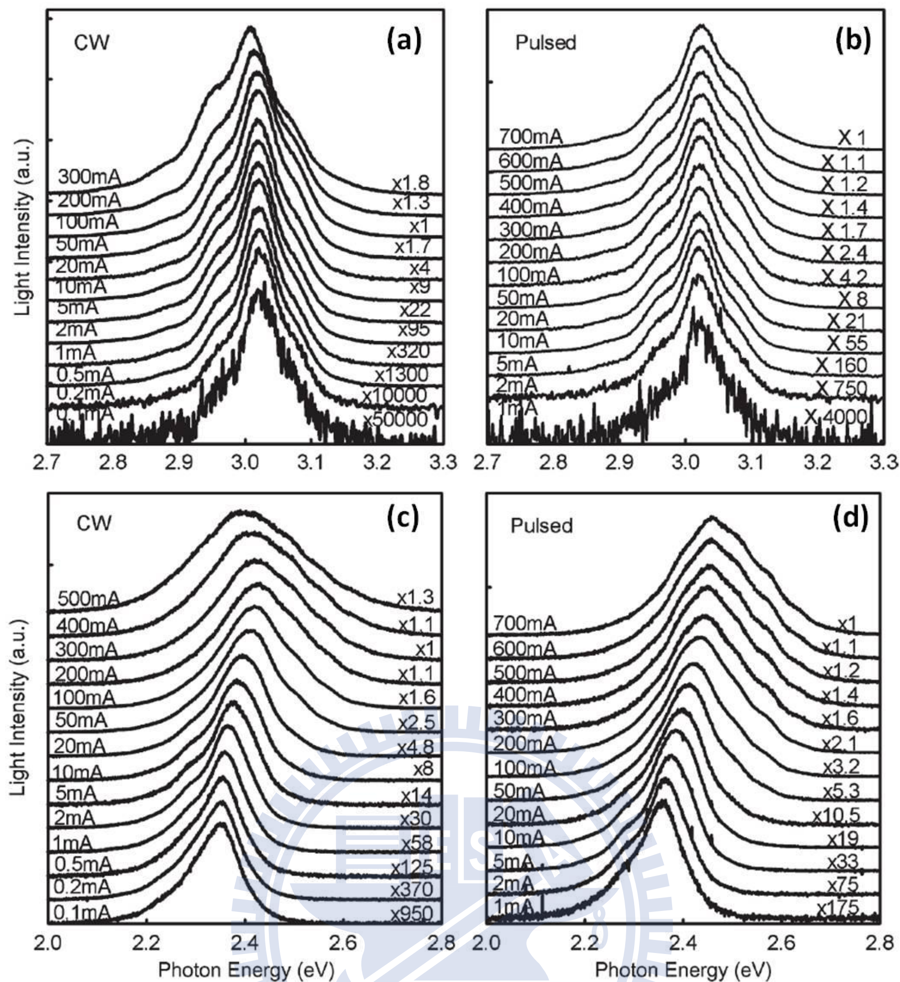

Fig. 4.4.6. EL spectra for the near-UV LED (top) with increasing (a) CW current and (b) pulsed current, and green LED (bottom) with increasing (c) CW current and (d) pulsed current with a duty cycle of 1 %.

Therefore, the absence of noticeable blue shift in the near-UV LED (see Fig. 4.4.4) suggests the following:

(a) The influence of piezoelectric field is minimal, which is presumably due to the effective screening by Si doping in the barrier layers.

(b) There are much weaker localization effects in the near-UV LED due to the improved composition homogeneity and thickness uniformity of the lower In content InGaN QWs.

In order to investigate the physical origin of efficiency droop in these near-UV LEDs, we performed a simulation of the above structures by using the APSYS simulation software.

Commonly accepted Shockley-Read-Hall recombination lifetime (about ~6 ns) and Auger recombination coefficient (about ~10^{-30} cm^6s^{-1}) are used in the simulations. Other material parameters of the semiconductors used in the simulation can be found in Ref. 18. In addition, we can reduce the effect of spontaneous and piezoelectric polarizations, because of lattice match condition in barrier between AlGaN and InAlGaN. The total polarization fields in different combination of materials can be obtained through the calculation, and the results of $In_{0.025}Ga_{0.975}N$, $Al_{0.08}Ga_{0.92}N$ and $In_{0.0085}Al_{0.1112}Ga_{0.8803}N$ are -0.0305, -0.0391 and -0.0398 ($C\cdot m^{-2}$), respectively [59].

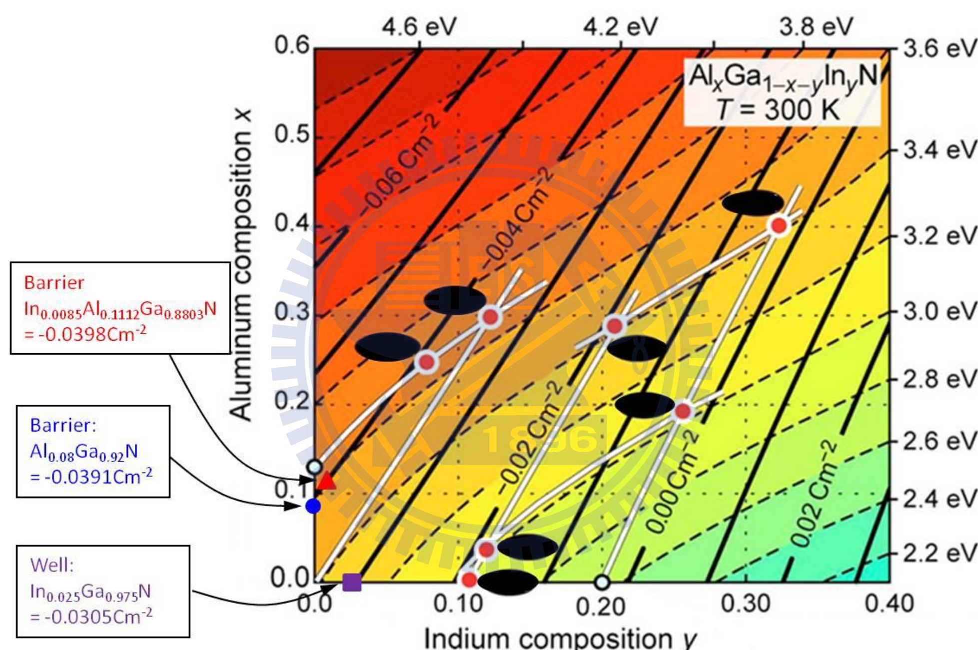

Fig. 4.4.7. Bandgap (dashed-line contours) and total polarization charge (solid-line contours) of AlGaInN as a function of Al and In compositions.

Besides, a different band-offset ratio from 6:4 to 7:3 is used in this simulation for introducing of indium in AlGaN. We can know that under the same energy band of barrier, the band-offset ratio from 6:4 to 7:3 will lead higher conduction-band and lower valence-band between well and barrier as shown in Fig 4.4.8. This is useful for electron confinement and hole distribution in low indium content InGaN-based near-UV LEDs.

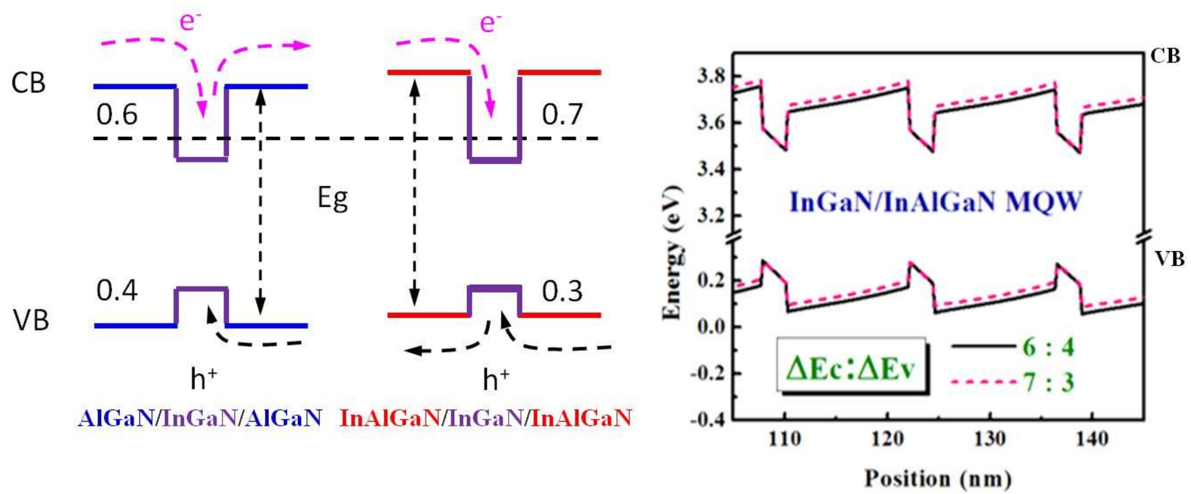

Fig. 4.4.8. Schematic of band diagram and band-offset ratio from 6:4 (InGaN/AlGaN) to 7:3 (InGaN/InAlGaN).

The IQE of the InGaN/InAlGaN near-UV LEDs with different band-offset ratio as a function of injection current is shown in Fig. 4.4.9. Inset in Fig. 4.4.9 shows the L-I curves of the InGaN/InAlGaN LEDs. The result of the efficiency peak and droop simulation of 7:3 is in good agreement direction with the experimental data.

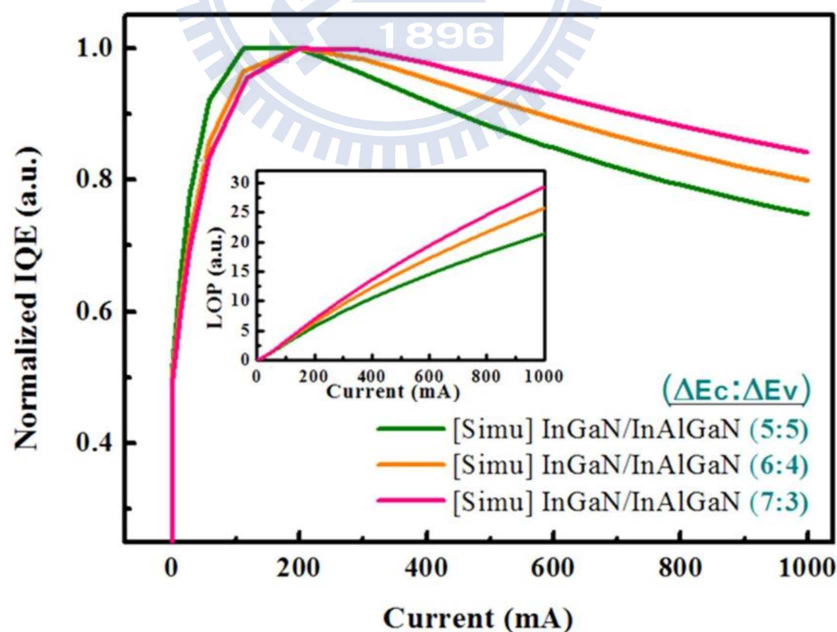

Fig. 4.4.9. Normalized IQE of InGaN/InAlGaN near-UV LED with different band-offset ratio from 5:5, 6:4 to 7:3. Inset in Fig. 4.4.9 shows the L-I curves of the InGaN/InAlGaN LEDs.

However, another difficult problem is the inclusion of degenerate valence bands in minority carrier hole mobility. Hence, to investigate the efficiency droop in these two samples, we assume that InGaN-based near-UV LED with InAlGaN barrier has relatively high carrier mobility. To prove above hypothesis, we vary the carrier mobility of InAlGaN depending on the value of AlGaN, and these simulation results are shown in Fig. 4.4.10.

It can clearly be seen that the droop behavior is dominated by hole mobility, and we find the efficiency curve will nearest to the experimental result when electron and hole mobility of InAlGaN is about 1.8 and 2.5 times the value of AlGaN. The values of mobility for electron and hole are calculated by Caughey Thomas approximation and assumed in the simulation, $\mu_{n\text{-}InGaN/AlGaN} = 354$, $\mu_{n\text{-}InGaN/InAlGaN} = 642$, $\mu_{p\text{-}InGaN/AlGaN} = 2$ and $\mu_{p\text{-}InGaN/InAlGaN} = 5$ cm^2/Vs, respectively. Finally, the results of the EQE droop simulation of both different structures are in good agreement with the experimental data as shown in Fig. 4.4.10.

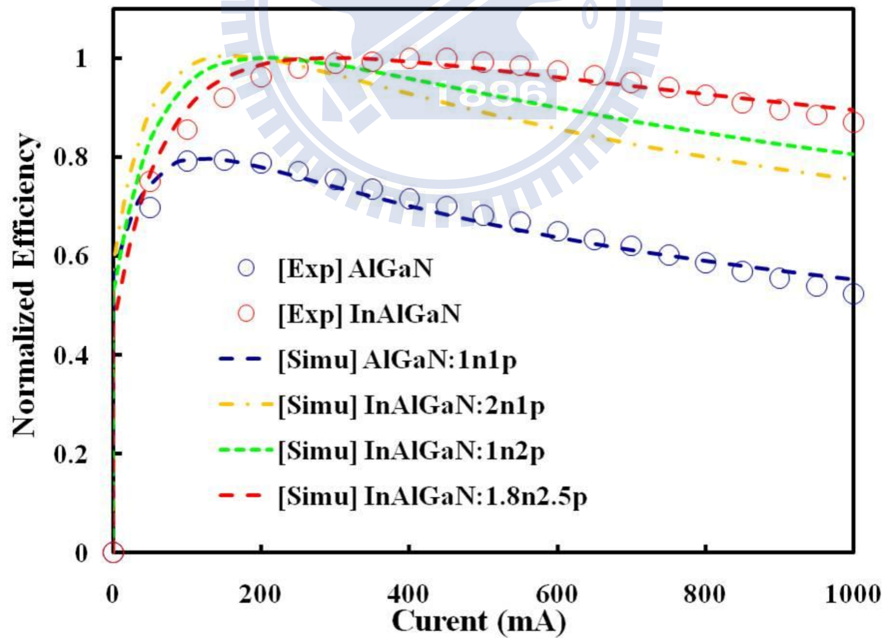

Fig. 4.4.10. Simulation results of normalized IQE under different carrier mobility.

Finally, we performed the numerical simulation with different parameters in band-offset ratio and carrier mobility, listed in Table 4.2.

Table 4.2. Simulation parameters in band-offset ratio and carrier mobility.

Items	Band offset ratio	Electron mobility ($cm^2/V^{-1}s^{-1}$)	Hole mobility ($cm^2/V^{-1}s^{-1}$)
InGaN/AlGaN MQWs	6 : 4	354	2
InGaN/InAlGaN MQWs	7 : 3	642	5

4.5 Theoretical Analysis

Finally, we have to check the actual carrier distribution in our simulation. Fig. 4.5.1 shows the calculated carrier distribution in these near-UV LEDs structure under a high forward current density of 100 A/cm^2 (1000 mA) by APSYS. When we apply the corresponding band-offset ratio and the carrier mobility in InGaN/InAlGaN MQWs, the electron and hole concentration increases in the QW by about 26 % and 35 %, respectively, and the distribution of carrier becomes more uniform than InGaN/AlGaN case. Under high current density, the carrier distribution of both electrons and holes determines how efficient the photon-emission process will be.

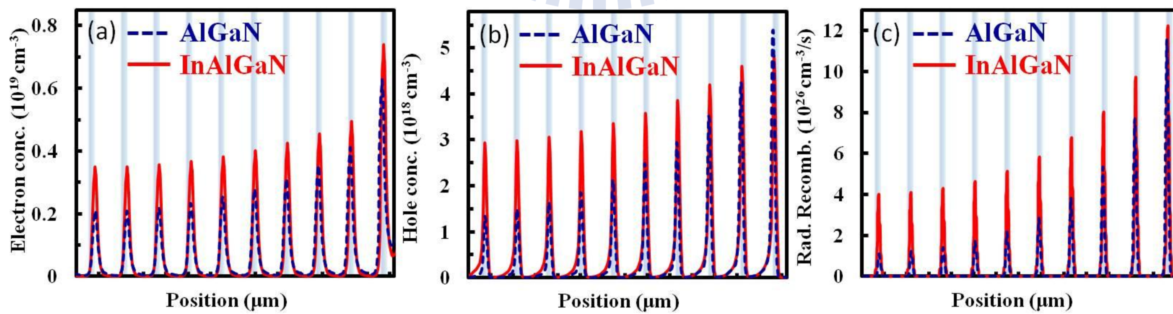

Fig. 4.5.1. Distribution of (a) Electron (b) Hole concentrations, and (c) Radiative recombination rates concentrations of the LEDs with AlGaN and InAlGaN barrier under a high forward current den sity of 100 A/cm^2.

As shown in Fig. 4.5.1, the peak-to-peak carrier ratio of InAlGaN barrier sample is reduced due to better carrier transportation, and this is also more obvious in the hole

distribution. The direct consequence is the increasing radiative recombination rate and thus the light output is expected to rise. On the other hand, in the traditional AlGaN barrier samples, the holes are locally concentrated in the first quantum well which causes the unbalanced distribution between different types of carriers, and thus leads to reduction of radiative recombination rate. Comparing electrons and holes, holes suffer more as a result of this nonuniformity due to their large effective mass and low mobility. Thus, our InAlGaN design can reduce the carrier leakage and increase electron-hole pair radiative recombination simultaneously, especially for the distribution of holes.

4.6 Summary

In summary, we fabricated and compared the performance of LEDs of InGaN-based near-UV MQWs active region with ternary AlGaN and quaternary InAlGaN barrier layers. HRXRD and TEM measurements show the two barriers are consistent with the lattice, and smooth morphology of quaternary InAlGaN layer can be observed in AFM. The electroluminescence results indicate that the light performance of the InGaN-based near-UV LEDs can be enhanced effectively when the conventional LT AlGaN barrier layers are replaced by the InAlGaN barrier layers. Furthermore, simulation results show that InGaN-based near-UV LEDs with quaternary InAlGaN barrier exhibit 62 % higher radiative recombination rate and low efficiency droop of 13 % at a high injection current. We attribute this improvement to increasing of carrier concentration and more uniform redistribution of carriers.

Chapter 5

High Quality GaN-based Vertical LED with Hexagonal Inversed Pyramid by Means of the Mechanical Lift-off

5.1 Introduction

Gallium nitride based materials have recently attracted considerable attention all over the world due to their potential applications in the optoelectronic devices, such as light emitting diodes (LEDs) and laser diodes (LDs) [95-97]. These devices were usually grown heteroepitaxially onto foreign substrates such as sapphire and SiC. The sapphire is the most commonly used substrate because of its relative low cost, but it also limits the devices performance due to its poor electrical and thermal conductivity.

During the last decade of years, the techniques of laser lift-off (LLO) [98, 99] and chemical lift-off (CLO) which use CrN layer [100], ZnO layer [101], and Si-doped n-GaN layer [102] as the sacrificial layer have been adopted to fabricate the freestanding GaN membrane and the vertical LEDs for the purpose of high performance optoelectronic devices. However, the LLO process may induce some possible damages under high temperature in the GaN/sapphire interface. And even though the CLO can prevent the GaN layer from the laser damage during the laser lift-off process, but it also makes another chemical etching damages and reduce the crystal quality.

In this work, we announce the fabrication of high quality GaN-based Vertical LED with hexagonal inversed pyramid (HIP) structures by mechanical lift-off (MLO). The interface morphologies and the optical properties of lifted-off GaN epilayer will be analyzed.

5.2 Sample Structures and Fabrication Methods

5.2.1 Fabrication the Hexagonal Inversed Pyramid (HIP) Structure

The GaN-based epilayer and LED structure was used in this study were all prepared by metal–organic chemical vapor deposition (MOCVD). We first deposited a 3 μm-thick un-doped GaN on a c-plane sapphire substrate as a template. The GaN epilayer was observed to be etched in the molten KOH for 10 mins at high temperature of 280 ^{o}C. The Hexagonal Inversed Pyramid (HIP) GaN/air/Sapphire structure was formed by the reversed etching from the N-face GaN. The etched path along with the threading dislocation propagation form the GaN top surface to the interface of GaN and sapphire, and the related processes have been presented in our previous study [103].

Finally, the HIP structures are created by anisotropic chemical wet etching at GaN-sapphire interface. The wet etching processes of molten KOH selectively etches defect sites from top-down, lateral etches LT buffer layer, and forms HIP GaN/air/Sapphire structure as illustrated in Fig. 5.2.1.

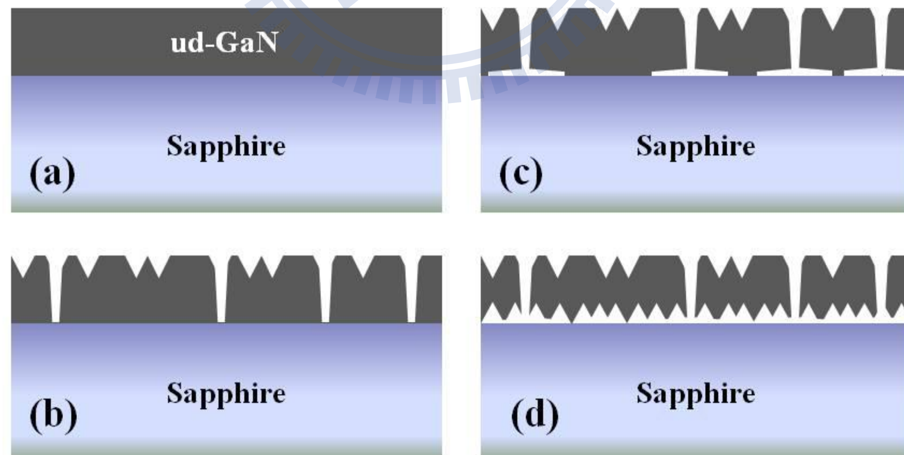

Fig. 5.2.1. Schematic of (a) ud-GaN/Sapphire (b) top-down etching (c) lateral etching (d) HIP GaN/air/Sapphire structure.

5.2.2 Regrowth LED Structure and Wafer Bonding Process

Next, the GaN-based LED structures were grown on HIP GaN/air/Sapphire template in the lateral regrowth process. The LED device structure was 2 μm modulation-doped GaN, 3.5 μm n-doped GaN, ten pairs of $Al_{0.02}Ga_{0.98}N/In_{0.1}Ga_{0.9}N$ quantum wells 13/2.5 nm, and 100 nm of p-doped GaN cap layer. The designed emission wavelength is measured at approximately 405 nm. After Ni/Au p-GaN contact layer was deposited on the p-GaN layer in the E-gun process, which was followed by a 2 mins annealing process to accomplish a low-resistance contact. The annealing temperature was 500 ℃ in ambient air. After annealing process, a reflective layer of 1500 Å Al was deposited to prevent light from reaching the absorbing Si substrate. In this way, a metalized Ni/Au bonding layer was deposited on the top of the Al layer. The thicknesses of Ni and that of Au layer were 1500 and 2000 Å, respectively. This 1500 Å Ni layer serves as an adhesive barrier layer while the 2000 Å Au layer serves as the seed layer in the electroplating process of 2 μm thick Au layer which is used to do Au-Si wafer bonding.

5.2.3 Mechanical Lift-off by using HIP structure

The conceptual process flow of the mechanical lift-off procedure is depicted in Fig. 5.2.2. In the Au-Si wafer bonding process, GaN thin film with HIP structure and sapphire substrate were under 400 ℃. GaN thin film will carry high-level thermal stress under this condition, and it will separate from sapphire substrate during cooling process because of different thermal expansive coefficient (CTE). This prominent CTE mismatch with GaN and sapphire brings an unbearable shear stress to the interface and as well makes the HIP structure break off. Therefore, the sapphire substrate can be removed simultaneously by way of this mechanical lift-off technique and follows the process of vertical LED (V-LED). The entire mechanical lift-off process of flowchart and GaN-based vertical LED is shown in Fig. 5.2.2.

As shown in Fig. 5.2.2, the entire mechanical lift-off process consists of five major parts: (a) GaN on sapphire; (b) The HIP GaN/air/Sapphire structure; (c) GaN-based LED structure on HIP GaN/air/Sapphire template; (d) Wafer bonding process; (e) Remove sapphire substrate by mechanical lift-off during cooling process.

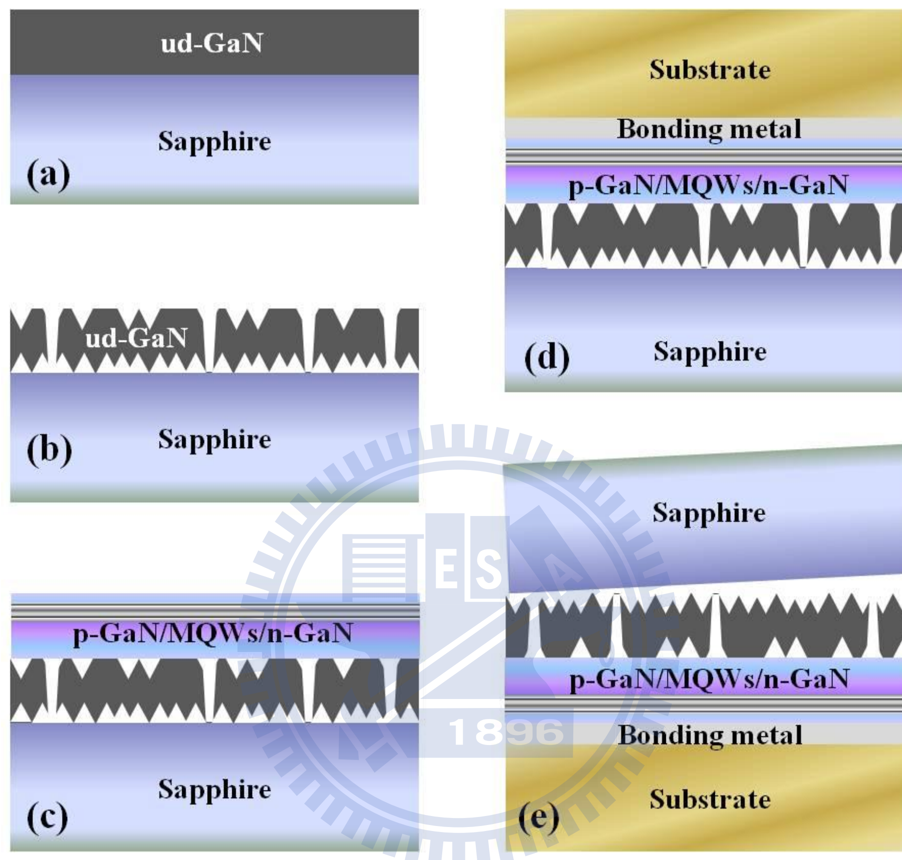

Fig. 5.2.2. The process flowchart for fabrication of GaN-based vertical LED: (a) GaN on Sapphire; (b) The HIP GaN/air/Sapphire structure; (c) GaN-based LED structure on HIP GaN/air/Sapphire template; (d)Wafer bonding process; (e) Remove sapphire substrate by mechanical lift-off during cooling process.

5.3 Characteristics of GaN-based V-LED with HIP Structure

5.3.1 HIP Structure

The etching process then turned into lateral direction because the defect density was high at interface and etched away a thin layer of GaN along sapphire interface. It is known that

KOH etching is typically anisotropic and preferentially etches specific crystallographic planes.

The cleaved sample, which is tilted to be examined under the scanning electron microscopy (SEM) after wet etching process, is shown in Fig. 5.3.1 (a), where the HIP structure at GaN/sapphire interface can be clearly observed and the V-shaped hexagonal pits of about 4.5×10^{6} cm^{-2} are also formed on the surface as shown in Fig. 5.3.1 (b). Inset in Fig. 5.3.1 are zoom in view of the HIP interface and surface. According to the SEM images, we can observe the behavior of three step wet etching process, pits density, and pits topography.

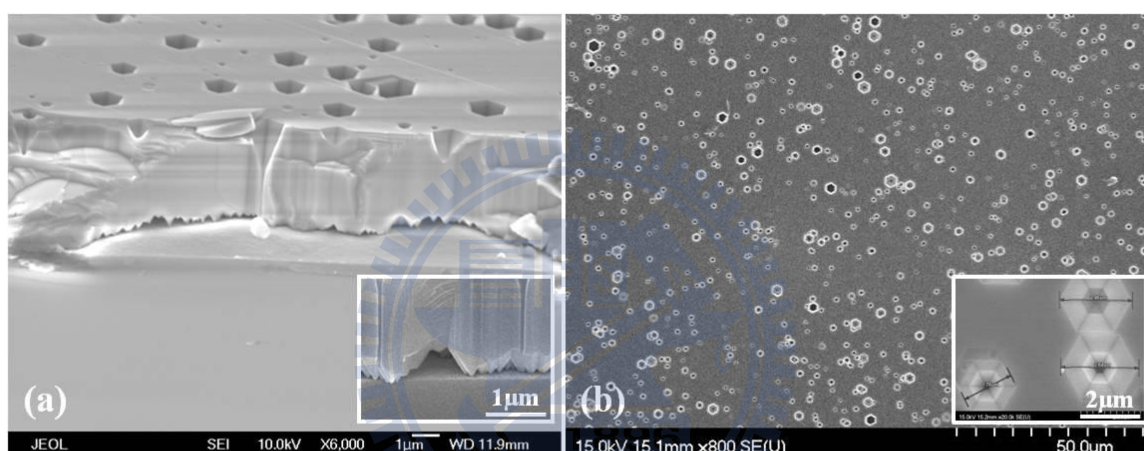

Fig. 5.3.1. (a) The tilted SEM image of the HIP structure; (b) SEM image of the etched GaN surface. Inset in Fig. 5.3.1 show the zoom in view images of the HIP structure.

5.3.2 Interface Morphologies

Additional GaN was grown on the etched GaN wafer to fill up both the etched openings and surface pits to provide a flat top surface for the subsequent LED device growth. Fig. 5.3.2 reveals the cross-sectional SEM image of the GaN-based LED sample at the GaN/sapphire interface in the regrowth process.

It was discovered that the HIP structures were still complete and some air voids were also found in the HIP structures. During the regrowth process, the growth temperature of GaN film is about 1150 ◦C. Under this high temperature, recrystallization of GaN is very possible

and final coalescence u-GaN HIP structure was performed and air voids were encapsulated, as shown in Fig. 5.3.2 (b).

From cross-sectional SEM images in Fig. 5.3.2 (b), we can estimate the average diameter of these air voids is about 100 nm. This result indicates that the vertical etched path was effectively hindered by means of the lateral overgrowth.

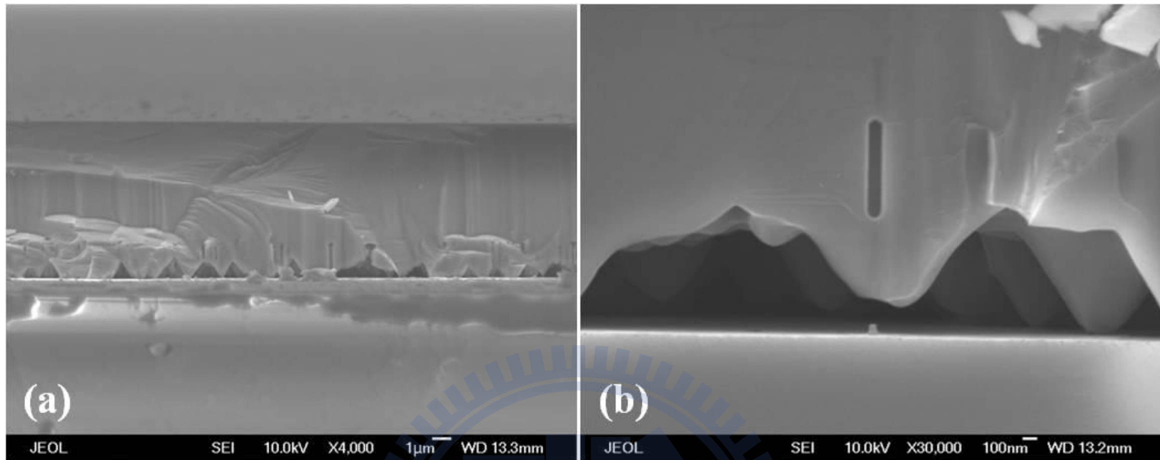

Fig. 5.3.2. Cross-sectional SEM images of (a) The regrowth HIP GaN/air/Sapphire interface; (b) Zoom in view of the interface.

Fig. 5.3.3 (a) illustrates the cross-sectional transmission electron microscopy (TEM) image of the GaN-based LED sample with the white lines indicating the regrowth boundary of the GaN epilayer regions. The formation of air void usually observed in the etching boundary during the lateral regrowth process.

The dislocation density at the bottom of the GaN layer is rendered at about 2×10^9 cm^{-2} and slightly reduces to 1×10^8 cm^{-2} at the top of the GaN layer. The density of dislocations degrades due to bending and a half loop of threading dislocations at the regrowth boundary. Most dislocations associate with each other by bending and loop formation, and they do not extend to the top surface as we can observe in Fig. 5.3.3 (b).

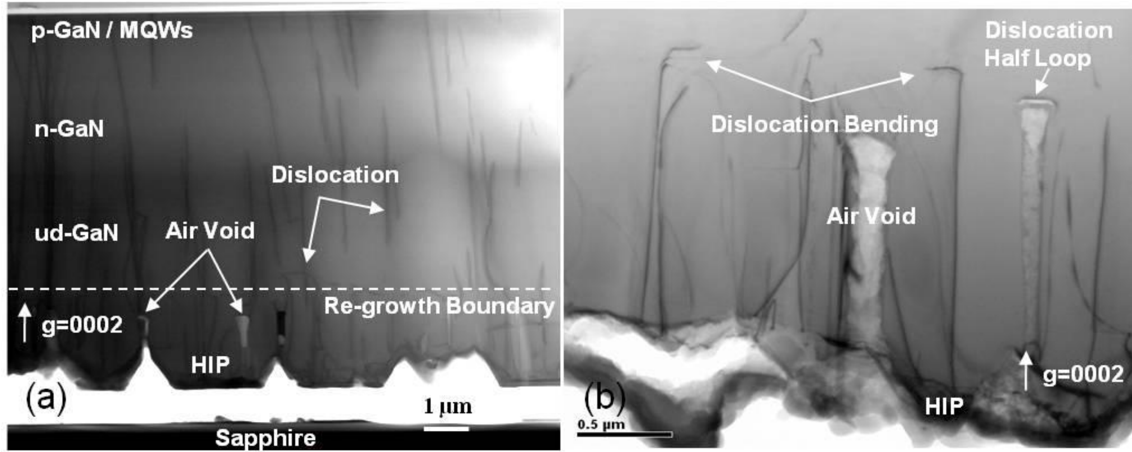

Fig. 5.3.3. Cross-sectional TEM images of (a) GaN-based LED structure grown on HIP GaN/air/Sapphire template (b) The regrowth HIP GaN/air/Sapphire boundary. The diffraction condition is g0002.

5.3.3 Vertical LED Structure and Surface Morphology

Fig. 5.3.4 unveils the Cross-sectional SEM image of the vertical LED structure after mechanical lift-off GaN LED/Silicon from the sapphire substrate at high temperature in the wafer bonding process. The inset in Fig. 5.3.4 reveals a top-view SEM image of the HIP surface morphology. Obviously, the cone shape structure and etched path were formed on the GaN surface in this sample. The size and density of etch cone shape estimated from SEM were 0.5 μm ~ 1 μm and 8×10^7 /cm^2, respectively.

The density of etch cone shape approach to GaN nucleation layer [104], hence we conjecture that the etch cone shape is the original seed layer of GaN nucleation layer. Accordingly, the etched paths were created throughout the GaN/sapphire interface and the GaN epilayer which is partially attached to the sapphire substrate. Therefore, the mechanical lift-off process was proved to be available by regarding the HIP structures as a sacrificial layer at high temperature during the wafer bonding process.

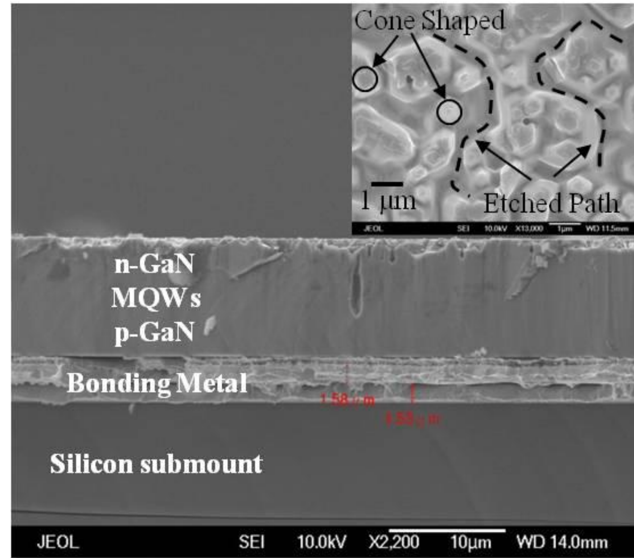

Fig. 5.3.4. Cross-sectional SEM image of the vertical LED structure after mechanical lift-off GaN LED/Silicon from sapphire substrate. Inset in Fig. 5.3.4 shows top-view SEM image of the HIP surface morphology after lift-off from sapphire substrate.

5.3.4 Raman Spectroscopy Analysis

Fig. 5.3.5 shows the room temperature Raman spectrum of the GaN epilayer regrowth on HIP structure and mechanical lift-off by HIP structure. The Raman shift peak of E_2 (high) for the GaN epilayer regrowth on HIP structure and mechanical lift-off by HIP structure were located at around 567.82 and 567.11 cm^{-1}, respectively. We can obtain the strain value of GaN epilayer with the following equation [105].

$$\Delta\omega = \omega_{E_2} - \omega_0 = C \cdot \sigma_{xx}$$

$$\sigma_{xx} = M_f \cdot \varepsilon_{xx} \qquad (5.3.1)$$

$$\varepsilon_{xx} = \frac{\Delta\omega}{C \cdot M_f}$$

As the equation uncovers, $\Delta\omega$ is the Raman shift peak difference between the strained GaN epilayer ω_{E2} and the unstrained GaN epilayer ω_0 (566.5 cm^{-1}). C is the biaxial strain coefficient, which is 2.25 cm^{-1}/GPa. M_f is the biaxial modulus to the substrate, which is 449.6

GPa [106]. σ_{xx} is the biaxial stress, and ε_{xx} is the biaxial strain.

The calculated in-plane compressive strain ε_{xx} are approximately 1.30×10^{-3} and 6.03×10^{-4} for the GaN epilayer regrowth on HIP structure and mechanical lift-off by HIP structure, respectively. The Raman shift peak of E_2 (high) for GaN on sapphire without HIP structure is 569.5 (cm^{-1}), and the in-plane compressive strain ε_{xx} is about 2.97×10^{-3}.

Table 5.1 shows the Raman shift of E_2 (high) mode and strain value of unstrained GaN, mechanical lift-off, regrowth on HIP, and GaN on sapphire, respectively. In other words, it implies that the residual stress of GaN-based LED can also be considerably declined while introducing the HIP structure to the GaN/sapphire interface.

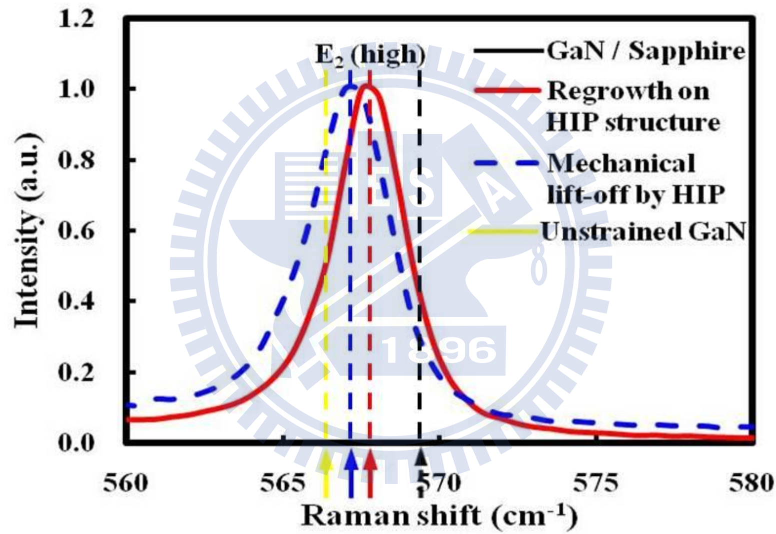

Fig. 5.3.5. Room temperature Raman spectrum of GaN epilayer regrowth on HIP structure and mechanical lift-off by HIP structure.

Table 5.1. The Raman shift of E_2 (high) mode and strain value.

Sample	Unstrained GaN	Mechanical lift-off	Regrowth on HIP	GaN on Sapphire
E_2 high (cm^{-1})	566.5	567.11	567.82	569.5
Compressive Strain	0	$6.03\text{x}10^{-4}$	$1.30\text{x}10^{-3}$	$2.96\text{x}10^{-3}$

5.3.5 Electrical and Optical Properties

In order to compare the performance of V-LED fabricated by mechanical lift-off with regular LEDs on a sapphire substrate, regular LEDs were also fabricated by applying the same LED structure for reference (Ref-LED) and the same size of 380×380 μm^2.

The room temperature electroluminescence (EL) spectra of both LEDs collected in the normal to the front surface direction at 20 mA are shown in Fig. 5.3.6 (a). The peak wavelength of V-LED and that of Ref-LED are 405.5 and 406 nm, respectively. The inset in Fig. 5.3.6 (a) shows the schematic of the Ref-LED and V-LED chips.

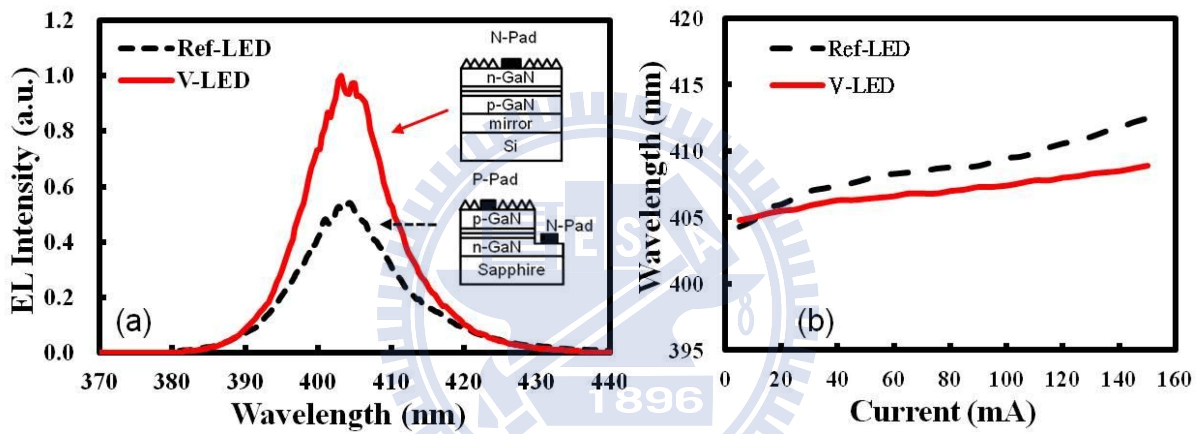

Fig. 5.3.6. (a) EL spectra of Ref-LED and V-LED in normal direction at 20mA. (b) The peak wavelength shift of the LEDs. Inset in Fig. 5.3.6 (a) shows the schematic of the Ref-LED and V-LED.

Fig. 5.3.6 (b) shows the variation of LED emission peak wavelength of the V-LED and that of the Ref-LED under high current continuous-wave (cw) operation conditions with epoxy-based 5 mm lamp package. The peak wavelength of the Ref-LED showed a relatively larger redshift of about 6.5 nm from a low current of 20 mA to a high current of 150 mA. However, the peak wavelength of the V-LED displayed only a slight redshift of about 3.4 nm in the same current range, indicating the relief of compressive strain and better heat dissipation in V-LED.

Fig. 5.3.7 shows the light output intensity–current–voltage (L – I –V) characteristics

under cw operation conditions for the V-LED and the Ref-LEDs. The forward voltage of V-LED and that of Ref-LED are 3.38 and 3.58 V, respectively. The light output intensity of the V-LED is higher by 100 % than the Ref-LED at 20 mA.

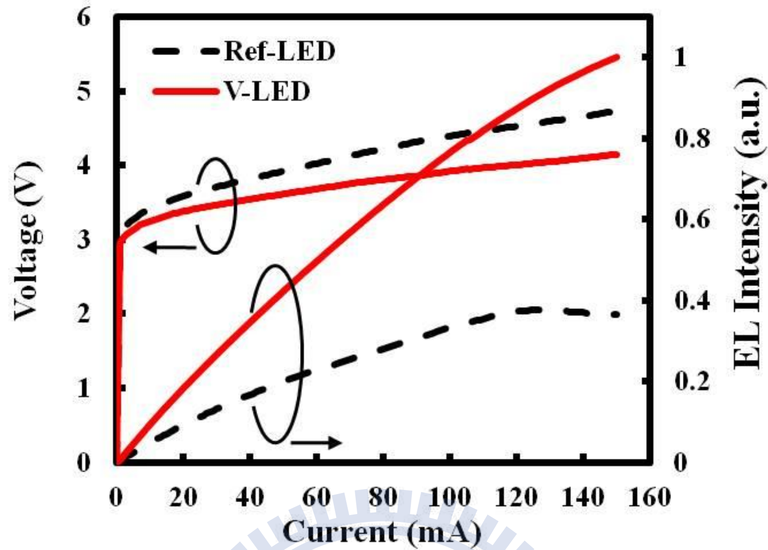

Fig. 5.3.7. L-I-V characteristics of the two fabricated LEDs.

An image of GaN-based LED transferred onto p-Si wafer is shown in Fig. 5.3.8 (a). It clearly confirmed that the lift-off process of GaN through HIP transformation can be used for GaN-based vertical LED. The light emitting image of near-UV V-LED is observed at 20 mA operating currents as shown in Fig. 5.3.8 (b), and the OM image of the 380×380 μm^2 V-LED chip under 1 mA driving current is shown in Fig. 5.3.8 (c).

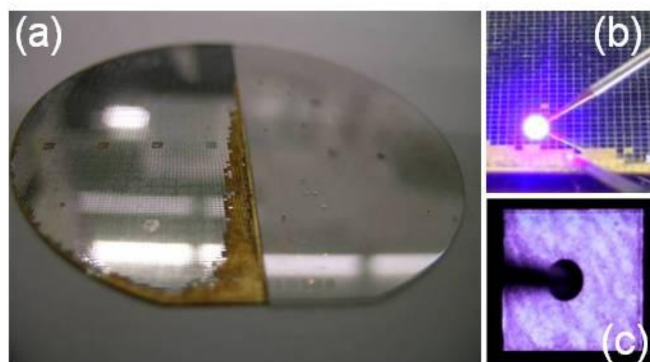

Fig. 5.3.8. (a) An image of V-LED/Si wafer after lift-off process from sapphire substrate. (b) The light emitting image of near-UV V-LED is observed at 20 mA operating currents. (c) OM image of 380×380 μm^2 V-LED chip at a 1 mA current injection.

5.4 Theoretical Analysis of Mechanical Lift-off

The strain of GaN growth on sapphire or Si substrate to be reduced by air gap structure had been discussed [107, 108]. The HIP structure partially relieves GaN from sapphire interface so that relieves the compressive strain. This partially relieved layer serves as a template in the subsequent regrowth process. It acted as a transition layer to partially filter the mismatched lattice constant and thermal expansion coefficient problems to improve the crystal quality. Therefore, we speculate that this HIP structure will efficiently reduce the stress state on regrowth GaN epilayer, in which the high efficiency vertical LED was demonstrated.

Table 5.2 show material properties of GaN, Si (111), and sapphire, where the given thermal expansion coefficient is an averaged value and might differ significantly at very low and at high temperatures.

Table 5.2. Material properties of GaN, Si (111), and sapphire [109].

Material	*a* (Å)	*c* (Å)	thermal conductivity (W/cm · K)	thermal expansion coefficient in-plane (10^{-6}/K)	lattice mismatch GaN/substrate (%)	thermal mismatch GaN/substrate (%)
Sapphire	4.758	12.991	0.5	7.5	16	-34
GaN	3.189	5.185	1.3	5.59	-	-
Si (111)	5.430	-	1-1.5	2.59	-16.9	54

Calculation of in-plane thermal mismatch between Si and Sapphire substrate, we can get the mismatch percentage during cooling down from 400 ^{o}C to room temperature (20 ^{o}C) in bonding process is about 0.18 %. Consequently, GaN thin film between Si and Sapphire is under large strain and the HIP structures play a sacrificial layer for mechanical lift-off process. The schematic of entire mechanical lift-off process is shown in Fig. 5.4.1.

From inset in Fig. 5.3.4, top-view SEM image of the HIP surface morphology shows only about 18 % of the contact area with the sapphire substrate. It implies that partially attached to the sapphire substrate of LT GaN HIP structures bear 5.5 times of stress.

Therefore, the mechanical lift-off process was proved to be available by regarding the HIP structures as a sacrificial layer at high temperature during the wafer bonding process.

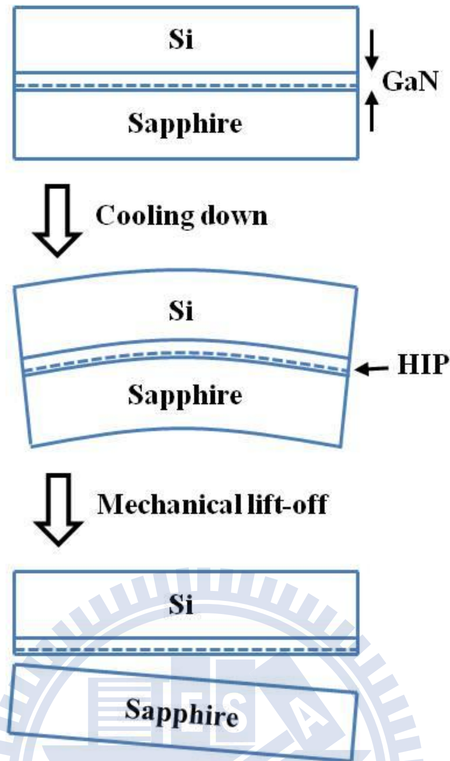

Fig. 5.4.1. Schematic of mechanical lift-off process.

5.5 Summary

In summary, we have successfully demonstrated the fabrication of mechanical lift-off high quality thin GaN LED with HIP structures as a sacrificial layer during wafer bonding process for vertical LEDs. The density of threading dislocations can be efficiently reduced from 2×10^9 to 1×10^8 cm^{-2} by applying the regrowth GaN epilayer on HIP structure. The reduction of dislocation was due to bending and a half loop of threading dislocations at the regrowth boundary. The in-plane compressive strain ε_{xx} are calculated to be about 1.30×10^{-3} and 6.03×10^{-4} for the GaN epilayer regrowth on HIP structure and mechanical lift-off by HIP structure, respectively. It implies that the residual stress of GaN-based LED can also be greatly reduced while introducing the HIP structure to the GaN/sapphire interface. The peak

wavelength of the V-LED also shows only a slight redshift of about 3.4 nm in the spectrum from 20 mA to 150 mA. The result indicates the relief of compressive strain and better heat dissipation in V-LED. Finally, the overall optical output power has shown significant 100 % enhancement under operating current 20 mA with this mechanical lift-off technique for fabrication the vertical-LED, and the mechanical lift-off process was proved to be available by regarding the HIP structures as a sacrificial layer at high temperature during the wafer bonding process.

1896

Chapter 6

Conclusions and Future work

In the thesis, we have demonstrated the high efficient near-UV LEDs by replacing AlGaN by InAlGaN barrier in active region and the mechanical lift-off technology for V-LEDs. Therefore, we will summarize the works contributed from the research.

First, we have demonstrated the high efficient near-UV LEDs by replacing AlGaN by InAlGaN barrier in active region. A 50-nm AlGaN and InAlGaN single heteroepitaxial layers grown on n-AlGaN/ud-GaN/Sapphire, and InGaN/AlGaN and InGaN/InAlGaN MQWs LED structures are prepared to investigate the optoelectronic properties of material and devices in this study. PL emission energy of these two samples are very close and the peak intensity of InAlGaN is slightly higher than AlGaN. The strong PL emission is attributed to the better crystal quality. The relatively small pits and smooth morphology of LT InAlGaN layer can be observed in AFM, and this phenomenon can mainly be attributed to the smaller tensile strain in LT AlGaN or LT GaN by inserting the isoelectronic In atoms. HRXRD and TEM measurements show the two barriers are consistent with the lattice, and the compositions of ternary and quaternary barriers were $Al_{0.08}Ga_{0.92}N$ and $In_{0.0085}Al_{0.1112}Ga_{0.8803}N$, respectively. The light output power of InGaN-based near-UV LED with the InAlGaN barrier is higher by 25 % and 55 % than the AlGaN barrier at 350 mA and 1000 mA, respectively. InGaN/InAlGaN near-UV LEDs exhibit only 13 % efficiency droop when we increase the injection current to 1000 mA. The reduction of efficiency droop is quite clear and the current at maximum efficiency shifts from 150 to 400 mA.

Furthermore, simulations show that quaternary LEDs exhibit 62 % higher radiative recombination rate and low efficiency degradation of 13 % at a high injection current of 100 A/cm^2. The band-offset ratio from 6:4 to 7:3 will lead higher conduction-band and lower valence-band between well and barrier, and the efficiency curve will nearest to the

experimental result when electron and hole mobility of InAlGaN is about 1.8 and 2.5 times the value of AlGaN. APSYS simulations show the electron and hole concentration increases in the QW by about 26% and 35%, respectively, and the distribution of carrier becomes more uniform than InGaN/AlGaN case. We attribute this improvement to increasing of carrier concentration and more uniform redistribution of carriers in active region.

Second, we have successfully demonstrated the fabrication of mechanical lift-off high quality GaN-based near-UV LED with HIP structures as a sacrificial layer during wafer bonding process for V-LEDs. The HIP GaN/air/Sapphire structures are formed at the GaN/sapphire substrate interface under high temperature during KOH wet etching process. The density of threading dislocations can be efficiently reduced from 2×10^{9} to 1×10^{8} cm^{-2} by applying the regrowth GaN epilayer on HIP structure. Raman spectroscopy analysis revealed that the compressive stress of GaN epilayer was effectively relieved in the GaN-based near-UV V-LED with HIP structures. The calculated in-plane compressive strain ε_{xx} are approximately 1.30×10^{-3} and 6.03×10^{-4} for the GaN epilayer regrowth on HIP structure and mechanical lift-off by HIP structure, respectively. It implies that the residual stress of GaN-based LED can also be greatly reduced while introducing the HIP structure to the GaN/sapphire interface. The size and density of etch cone shape estimated from SEM were 0.5 μm ~ 1 μm and 8×10^{7} /cm^{2}, respectively. The density of etch cone shape approach to GaN nucleation layer, hence we conjecture that the etch cone shape is the original seed layer of GaN nucleation layer. The peak wavelength of the V-LED also shows only a slight redshift of about 3.4 nm in the spectrum from 20 mA to 150 mA. The result indicates the relief of compressive strain and better heat dissipation in V-LED. Finally, the overall optical output power has shown significant 100 % enhancement under operating current 20 mA with this mechanical lift-off technique for fabrication the vertical-LED, and the mechanical lift-off process was proved to be available by regarding the HIP structures as a sacrificial layer at

high temperature during the wafer bonding process.

The 0.18 % of substrate mismatch from divergent thermal expansion coefficient during cooling down process from 400 °C to room temperature shows that GaN thin film between Si and Sapphire was under large strain and the HIP structures must play a sacrificial layer for mechanical lift-off process. SEM image of the HIP surface morphology shows only about 18 % of the contact area with the sapphire substrate. It implies that partially attached to the sapphire substrate of LT GaN HIP structures bear 5.5 times of stress. Therefore, the mechanical lift-off process was proved to be available by regarding the HIP structures as a sacrificial layer at high temperature during the wafer bonding process.

In the previous work, the quaternary material has been proved to be helpful to improve the internal quantum efficiency. However, it is more difficult to develop quite low indium composition in deep wavelength such as 365 nm UV LEDs for curing application.

In the future work, InAlGaN will match in optimized AlGaN barrier in low indium content 365 nm QWs for a fair investigation on the light output and efficiency current droop characteristics. The InGaN-based 365 nm UV LEDs structures are shown in Fig. 6.1.

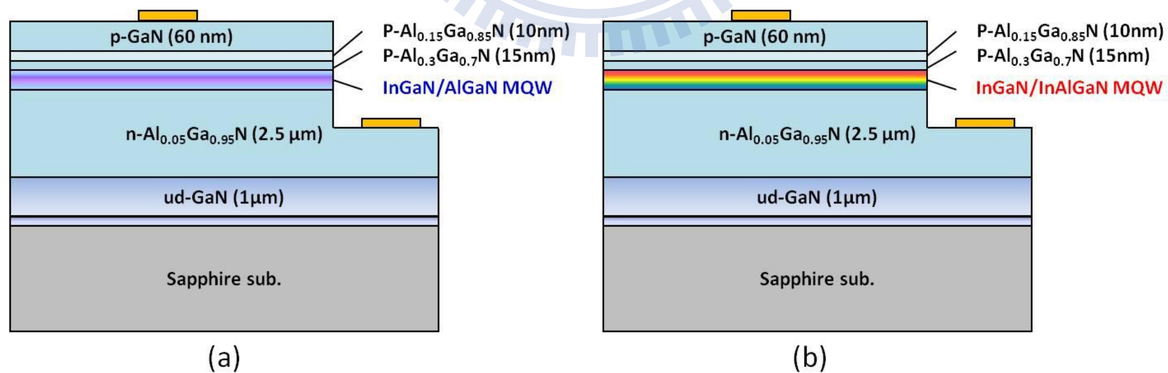

Fig. 6.1. Schematic structures of 365 nm UV LEDs with (a) $Al_{0.15}Ga_{0.85}N$ barrier and (b) $In_{0.02}Al_{0.18}Ga_{0.8}N$ barrier.

In order to achieve mass production of high quality V-LEDs, it is necessary to develop a stable lift-off process. Hence, we will use the porous SiO_2/GaN nanorod array as a sacrificial layer for chemical lift-off process. The entire process of flowchart and V-LEDs structure is

shown in Fig. 6.2.

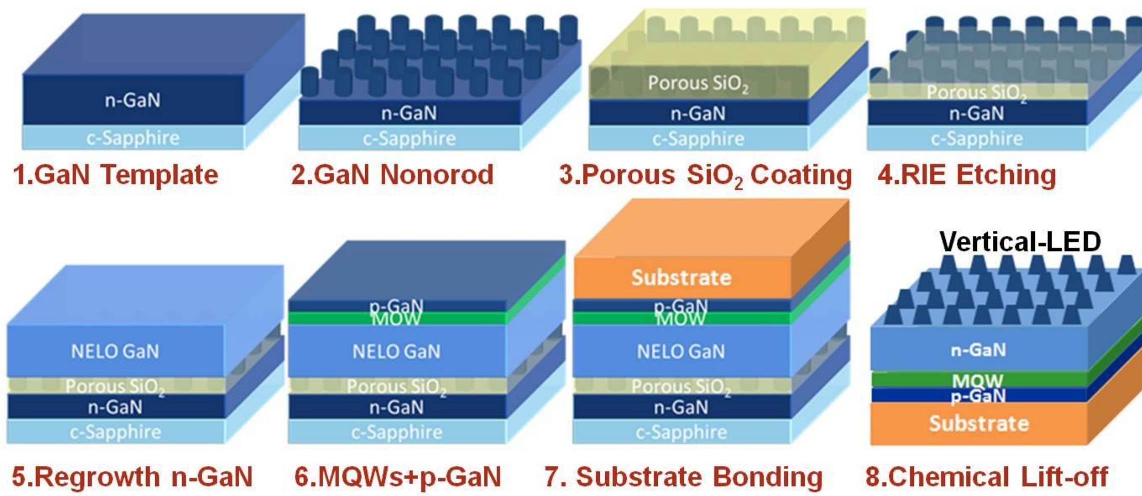

Fig. 6.2. The process flowchart for fabrication of V-LEDs by using the porous SiO_2/GaN nanorod array.

According to these advantages of quaternary InAlGaN and creative lift-off process, we expect near-UV LED can finally achieve the higher efficiency without droop in the future.

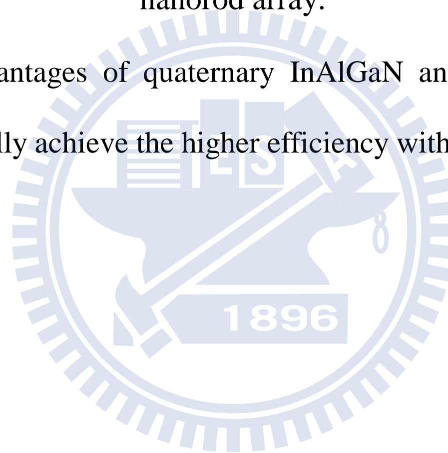

References

[1] S. Nakamura, T. Mukai, and M. Senoh, *Appl. Phys. Lett.* **64**, 1687 (1994).

[2] G. Y. Xu, A. Salvador, W. Kim, Z. Fan, C. Lu, H. Tang, H. Markoc, G. Smith, M. Estes, B. Goldberg, W. Yank, and S. Krishnankutty, *Appl. Phys. Lett.* **71**, 2154 (1997).

[3] T. G. Zhu, D. J. H. Lambert, B. S. Shelton, M. N. Wong, U. Chowdhury, H. K. Kwon, and R. D. Dupuis, *Electron Lett.* **36**, 1971 (2000).

[4] G. T. Dang, A. P. Zhang, F. Ren, X. A. Cao, S. J. Pearton, H. Cho, J. Han, J. I. Chyi, C. M. Lee, C. C. Chuo, S. N. G. Chu, and R. G. Wilson, *IEEE Trans. Electron Devices* **47**, 692 (2000).

[5] B. S. Shelton, D. J. H. Lambert, H. J. Jang, M. M. Wong, U. Chowdhury, Z. T. Gang, H. K. Kwon, Z. Liliental-Weber, M. Benarama, M. Feng, and R. D. Dupuis, *IEEE Trans. Electron Devices* **48**, 490 (2001).

[6] A. P. Zhang, J. Han, F. Ren, K. E. Waldrio, C. R. Abernathy, B. Luo, G. Dang, J. W. Johnson, K. P. Lee, and S. J. Pearton, *Electronchem. Solid-State Lett.* **4**, G39 (2001).

[7] S. Nakamura, M. Senoh, S. Nagahama, N.Iwasa, T. Yamada, T. Matsushita, Y. Sugimoto, and H. Kiyoku, *Appl. Phys. Lett.* **70**, 868 (1997).

[8] S. Nakamura, *Science* **281**, 956 (1998).

[9] Y. Arakawa, *IEEE J. Select. Topics Quantum Electron.* **8**, 823 (2002).

[10] S. Nakamura, M. Senoh, N. Iwasa, and S. Nagahama, *Jpn. J. Appl.Phys.* **34**, 797 (1995).

[11] T. Matsuoka, H. Okamoto, M. Nakao, H. Harima, and E. Kurimoto, *Appl. Phys. Lett.* **81**, 1246 (2002).

[12] H. Morkoc, *Nitride Semiconductors and devices*, (Springer-Verlag, Berlin, 1999).

[13] E. F. Schubert, Light-Emitting Diodes, 2nd ed., pp. 212. (Cambridge University Press, Cambridge, 2006).

[14] H. Morkoc, *Nitride Semiconductors and Devices (Spring Verlag, Heidelberg)* (1999).

[15] J. I. Pankove, E. A. Miller, and J. E. Berkeyheiser, *J. Lumin.* **5**, 84 (1972).

[16] H. Amano, N. Sawaki, I. Akasaki, and Y. Toyoda, *Appl. Phys. Lett.* **48**, 353 (1986).

[17] H. Amano, I. Akasaki, T. Kozawa, K. Hiramatsu, N. Sawaki, K. Ikeda, and Y. Ishii, *J. Lumin.* **40**, 121 (1988).

[18] H. Amano, N. Sawaki, I. Akasaki, and Y. Toyoda, *Jpn. J. Appl. Phys.* **28**, 2112 (1989).

[19] S. Nakamura, *Jpn. J. Appl. Phys.* **30**, 1705 (1991).

[20] S. Nakamura, T. Mukai, M. Senoh, and N. Jwasa, *Jpn. J. Appl. Phys.* **31**, 1258 (1992).

[21] S. Nakamura, T. Mukai, M, Senoh, S. Nagahama, and N. Jwasa, *Journal of Applied Physics* **74**, 3911 (1993).

[22] S. Nakamura, G. Fasol, Springer-Verlag, Berlin, (1997).

[23] J. I. Pankove, *Mater Sci Eng* **B61-62**, 305 (1999).

[24] A. Sandhu, *Nature Photonics* **1**, 38 (2007).

[25] Y. S. Tang, S. F. Hu, C. C. Lin, N. C. Bagkar, and R. S. Liu , *Appl. Phys. Lett.* **90**, 151108 (2007).

[26] Y. C. Chiu, W. R. Liu, C. K. Chang, C. C. Liao, Y. T. Yeh, S. M. Jang, and T. M. Chen, *J. Mater. Chem.* **20**, 1755 (2010).

[27] J. Han, M. H. Crawford, R. J. Shul, J. J. Figiel, M. Banas, L. Zhang, Y. K. Song, H. Zhou, and A. V. Nurmikko, *Appl. Phys. Lett*. **73**, 1688 (1998).

[28] T. Mukai, M. Yamada, and S. Nakamura, *Jpn. J. Appl. Phys*. **37**, 1358 (1998).

[29] T. Nishida, and N. Kobayashi, *Phys. Stat. Sol. A* **176**, 45 (1999).

[30] H. Hirayama, *J. Appl. Phys.* **97**, 091101 (2005).

[31] M. S. Shur and A. Zukauskas, Editors, *UV Solid-State Light Emitters and Detectors.* Proc. NATO ARW, Series II, Vol. 144, Kluwer, Dordrecht, ISBN 1-4020-2034-1, pp. 41-58 (2004).

[32] M. Kneissl, T. Kolbe, C. Chua, V. Kueller, N. Lobo, J. Stellmach, A. Knauer, H. Rodriguez, S. Einfeldt, Z. Yang, N. M. Johnson, and M. Weyers, *Semicond. Sci. Technol.* **26**, 014036 (2011).

[33] APSYS by Crosslight Software Inc, Burnaby, Canada: http://www.crosslight.com.

[34] W. S. Wong, T. Sands, N. W. Cheung, M. Kneissl, D. P. Bour, P. Mei, L.T. Romano, and N. M. Johnson, *Appl. Phys. Lett.* **75**, 1360 (1999).

[35] W. Y. Lin, D. S. Wuu, K. F. Pan, S. H. Huang, C.E. Lee, W.K. Wang, S. C. Hsu, Y. Y. Su, S. Y. Huang, and R. H. Horng, *IEEE Photonics Technol. Lett.* **17**, 1809 (2005).

[36] H. Goto, S. W. Lee, H. J. Lee, H.-J. Lee, J. S. Ha, M. W. Cho, and T.Yao, *Phys. Status Solidi. C* **5**, 1659 (2008).

[37] D. J. Rogers, F. Hosseini Teherani, A. Ougazzaden, S. Gautier, L. Divay, A. Lusson, O. Durand, F. Wyczisk, G. Garry, T. Monteiro, M. R. Correira, M. Peres, A. Neves, D. McGrouther, J. N. Chapman, and M. Razeghi, *Appl. Phys. Lett.* **91**, 071120 (2007).

[38] J. Park, K. M. Song, S. R. Jeon, J. H. Baek, and S. W. Ryu, *Appl. Phys. Lett.* **94**, 221907 (2009).

[39] H. Morkoç, *Handbook of Nitride Semiconductors and Devices* (Wiley, New York), Vol. 3. pp. 39 (2008).

[40] S. Nakamura, M. Senoh, and T. Mukai, *Appl. Phys. Lett.* **62**, 2390 (1993).

[41] E. F. Schubert, *Light-Emitting Diodes, 2nd ed.* (Cambridge University Press, Cambridge), pp. 146. (2006).

[42] E. F. Schubert, I. D. Goepfert, W. Grieshaber, and J. M. Redwing, *Appl. Phys. Lett.* **71**, 921 (1997).

[43] H. C. Yang, T. Y. Lin, M. Y. Huang, and Y. F. Chen, *J. Appl. Phys.* **86**, 6124 (1999).

[44] S. N. Lee, T. Sakong, W. S. Lee, H. S. Paek, J. K. Son, E. Yoon, O. H. Nam, Y. Park, *J. Cryst. Growth.* **261**, 249 (2004).

[45] E. Oh, H. S. Park, Y. Park, *Appl. Phys. Lett.* **72**, 70 (1998).

[46] M. G. Cheong, K. S. Kim, C. S. Kim, R. J. Choi, H. S. Yoon, N. W. Namgung, E. K. Suh, and H. J. Lee, *Appl. Phys. Lett.* **80**, 1001 (2002).

[47] M. Smith, G. D. Chen, J. Y. Lin, H. X. Jiang, A. Salvador, B. N. Sverdlov, A. Botchkarev, H. Morkoc, and B. Goldenberg, *Appl. Phys. Lett*. **68**, 1883 (1996).

[48] U. Kaufmann, M. Kunzer, M. Maier, H. Obloh, A. Ramakrishnan, B. Santic, and P. Schlotter, *Appl. Phys. Lett.* **72**, 1326 (1998).

[49] S. N. Lee, J. K. Son, T. Sakong, W. Lee, H. Paek, E. Yoon, J. Kim, Y. Cho, O. Nam, and Y. Park, *Journal of Crystal Growth.* **272**, 455 (2004).

[50] Kremzov R., private communications (2009).

[51] E. F. Schubert, *Light-Emitting Diodes, 2nd ed.*, pp. 86. (Cambridge University Press, Cambridge, 2006).

[52] A. Y. Kim, W. Götz, D. A. Seigerwald, J. J. Wierer, N. F. Gardner, J. Sun, S. A. Stockman, P. S. Martin, M. R. Krames, R. S. Kern, and F. M. Steranka, *Phys. Status Solidi A* **188**, 15 (2001).

[53] A. A. Efremov, N. I. Bochkareva, R. I. Gorbunov, D. A. Larinovich, Yu. T. Rebane, D. V. Tarkhin, and Yu. G. Shreter, *Semiconductors* **40**, 605 (2006).

[54] V. Rozhansky and D. A. Zakheim, *Phys. Status Solidi C* **3**, 2160 (2006).

[55] V. Rozhansky and D. A. Zakheim, *Phys. Status Solidi A* **204**, 227 (2007).

[56] K. Akita, T. Kyono, Y. Yoshizumi, H. Kitabayashi, and K. Katayama, *J. Appl. Phys.* **101**, 033104 (2007).

[57] M. F. Schubert, S. Chhajed, J. K. Kim, E. F. Schubert, D. D. Koleske, M. H. Crawford, S. R. Lee, A. J. Fischer, G. Thaler, and M. A. Banas, *Appl. Phys. Lett.* **91**, 231114 (2007).

[58] I.A. Pope, P.M. Smowton, P. Blood, J.D. Thomson, M.J. Kappers, and C.J. Humphreys, *Appl. Phys. Lett.* **82**, 2755 (2003).

[59] M. H. Kim, M. F. Schubert, Q. Dai, J. K. Kim, E. F. Schubert, J. Piprek, and Y. Park, *Appl. Phys. Lett.* **91**, 183507 (2007).

[60] I. V. Rozhansky and D. A. Zakheim, *Phys. Status Solidi A* **204**, 227 (2007).

[61] M.F. Schubert, J. Xu, J.K. Kim, E.F. Schubert,M.H. Kim, S. Yoon, S.M. Lee, C. Sone, T. Sakong, and Y. Park, *Appl. Phys. Lett.* **93**, 041102 (2008).

[62] K. J. Vampola, M. Iza, S. Keller, S. P. DenBaars, and S. Nakamura, *Appl. Phys, Lett.* **94**, 061116 (2009).

[63] K. Ding, Y. P. Zeng, X. C .Wei, Z. C. Li, J. X. Wang, H. X. Lu, P. P. Cong, X. Y. Yi, G. H.Wang, and J. M. Li, *Appl Phys B* **97**, 465 (2009).

[64] C. H. Wang, J. R. Chen, C. H. Chiu, H. C. Kuo, Y. L. Li, T. C. Lu, and S. C. Wang, *IEEE Photon. Technol. Lett.* **22**, 236 (2010).

[65] N.F. Gardner, G.O. Mueller, Y.C. Shen, G. Chen, and S. Watanabe, *Appl. Phys. Lett.* **91**, 243506 (2007).

[66] Y. C. Shen, G. O. Muller, S. Watanabe, N. F. Gardner, A. Munkholm, and M. R. Krames, *Appl. Phys. Lett.* **91**, 141101 (2007).

[67] K. A. Bulashevich and S. Y. Karpov, *Phys. Status Solidi C* **5**, 2066 (2008).

[68] A. David and M. J. Grundmann, *Appl. Phys, Lett.* **96**, 103504 (2010).

[69] B. Monemar and B. E. Sernelius, *Appl. Phys. Lett.* **91**, 181103 (2007).

[70] X.A. Cao, Y. Yang, and H. Guo, *J. Appl. Phys.* **104**, 093108 (2008).

[71] Y. Yang, X. A. Cao, and C. Yan, *IEEE Transactions On Electron Devices* **55**, 1771 (2008).

[72] A. A. Efremov, N. I. Bochkareva, R. I. Gorbunov, D. A. Lavrinovich, Yu. T. Rebane, D. V. Tarkhin, and Yu. G. Shreter, *Semiconductors* **40**, 605 (2006).

[73] Y. K. Kuo, J. Y. Chang, M. C. Tsai, and S. H. Yen, *Appl. Phys. Lett.* **95**, 011116 (2009).

[74] Hader, J. V. Moloney, B. Pasenow, S. W. Koch, M. Sabathil, N. Linder, and S. Lutgen, *Appl. Phys. Lett.* **92**, 261103 (2008).

[75] R. Davis, A. Roskowski, E. Preble, J. Speck, B. Heying, J. Freitas, E. Glaser, and W. Carlos, *Proc. IEEE* **90**, 993 (2004).

[76] S. L. Chuang and C. S. Chang, *Phys. Rev. B* **54**, 2491 (1996).

[77] I. Vurgaftman and J. R. Meyer, *J. Appl. Phys.* **94**, 3675 (2003).

[78] Y. P. Varshni, *Physica* **34**, 149 (1967).

[79] K. Osamura, S. Naka, and Y. Murakami, *J. Appl. Phys.* **46**, 3432 (1975).

[80] M. E. Aumer, S. F. LeBoeuf, F. G. McIntosh, and S. M. Bedair, *Appl. Phys. Lett.* **75**, 3315 (1999).

[81] C. G. Van de Walle and J. Neugebauer, *Nature* **423**, 626 (2003).

[82] V. Fiorentini, F. Bernardini, and O. Ambacher, *Appl. Phys. Lett.* **80**, 1204 (2002).

[83] J. P. Ibbetson, P. T. Fini, K. D. Ness, S. P. DenBaars, J. S. Speck, and U. K. Mishra, *Appl. Phys. Lett.* **77**, 250 (2000).

[84] S. F. Chichibu, A. C. Abare, M. S. Minsky, S. Keller, S. B. Fleischer, J. E. Bowers, E.Hu,U. K. Mishra, L. A. Coldren, S. P. DenBaars, and T. Sota, *Appl. Phys. Lett.* **73**, 2006 (1998).

[85] C. M. Caughey and R. E. Thomas, *Proc. IEEE* **55**, 2192 (1967).

[86] M. Farahmand *et al*. IEEE Trans. *Electron Devices* **48**, 535 (2001).

[87] I. H. Ho and G. B. Stringfellow, *Appl. Phys. Lett.* **69**, 2701 (1996).

[88] T. Mukai and S. Nakamura, *Jpn. J. Appl. Phys.* **38**, 5735 (1999).

[89] R. H. Horng, W. K. Wang, S. C. Huang, S. Y. Huang, S. H. Lin, C. F. Lin, and D. S. Wuu, *J. Cryst. Growth* **298**, 219 (2007).

[90] D. Morita, M. Yamamoto, K. Akaishi, K. Matoba, K. Yasutomo, Y. Kasai, M. Sano, S. i. Nagahama, and T. Mukai, *Jpn. J. Appl. Phys.* **43**, 5945 (2004).

[91] Q. Shan, Q. Dai, S. Chhajed, J. Cho, and E. F. Schubert, *J. Appl. Phys*. **108**, 084504 (2010).

[92] APSYS by Crosslight Software Inc., Burnaby, Canada: http://www.crosslight.com.

[93] J. J. Wu, X. X. Han, J. M. Li, H. Y. Wei, G. W. Cong, X. L. Liu, Q. S. Zhu, Z. G. Wang, Q. J. Jia, L. P. Guo, T. D. Hu, and H. H. Wang, *Optical Materials* **28**, 1227 (2006).

[94] S. Yamaguchi, M. Kariya, T. Kashima, S. Nitta, M. Kosaki, Y. Yukawa, H. Amano, and I. Akasaki, *Phys. Rev. B* **64**, 035318 (2001).

[95] S. Nakamura and G. Fasol, *The Blue Laser Diode:* GaN based Light Emitters and Lasers, Spring-Verlag, Berlin and Heidelberg (1997).

[96] E. F. Schubert, *Light Emitting Diodes*, 1st ed. (Cambridge University Press, Cambridge, 2003).

[97] J. Han, M. H. Crawford, R. J. Shul, J. J. Figiel, L. Zhang, Y. K. Song, H. Zhou, and A. V. Nurmikko, *Appl. Phys. Lett.* **73**, 1688 (1998).

[98] W. S. Wong, T. Sands, N. W. Cheung, M. Kneissl, D. P. Bour, P. Mei, L.T. Romano, and N. M. Johnson, *Appl. Phys. Lett.* **75**, 1360 (1999).

[99] W. Y. Lin, D. S. Wuu, K. F. Pan, S. H. Huang, C.E. Lee, W.K. Wang, S. C. Hsu, Y. Y. Su, S. Y. Huang, and R. H. Horng, *IEEE Photonics Technol. Lett.* **17**, 1809 (2005).

[100] H. Goto, S. W. Lee, H. J. Lee, H.-J. Lee, J. S. Ha, M. W. Cho, and T.Yao, *Phys. Status Solidi C* **5**, 1659 (2008).

[101] D. J. Rogers, F. Hosseini Teherani, A. Ougazzaden, S. Gautier, L. Divay, A. Lusson, O. Durand, F. Wyczisk, G. Garry, T. Monteiro, M. R. Correira, M. Peres, A. Neves, D. McGrouther, J. N. Chapman, and M. Razeghi, *Appl. Phys. Lett.* **91**, 071120 (2007).

[102] J. Park, K. M. Song, S. R. Jeon, J. H. Baek, and S. W. Ryu, *Appl. Phys. Lett.* **94**, 221907

(2009).

[103] M. H. Lo, P. M. Tu, C. H. Wang, C. W. Hung, S. C. Hsu, Y. J. Cheng, H. C. Kuo, H. W. Zan, S. C. Wang, C. Y. Chang, and S. C. Huang, *Appl. Phys. Lett.* **95**, 041109 (2009).

[104] D. D. Koleske, M. E. Coltrin, S. R. Lee, G. Thaler, K. C. Cross, and M. J. Russell, *Proc. SPIE* **6841**, 68410H (2007).

[105] P. Puech, F. Demangeot, J. Frandon, C. Pinquier, M. Kuball, V. Domnich, and Y. Gogotsi., *J. Appl. Phys.* **96**, 2853 (2004).

[106] S. Hearne, E. Chason, J. Han, J.A. Floro, J. Figiel, J. Hunter, H. Amano, and I.S.T. Tsong, *Appl. Phys. Lett.* **74**, 356 (1999).

[107] K. Kusakabe, A. Kikuchi, and K. Kishino, *Jpn. J. Appl. Phys.* **40**, L192 (2001).

[108] J. R. Chang, T. H. Yang, J. T. Ku, S. G. Shen, Y. C. Chen, Y. Y. Wong, and C.Y. Chang, *J. Cryst. Growth* **311**, 1997 (2009).

[109] A. Krost and A. Dadgar, *phys. stat. sol. (a)* **194**, 361 (2002).

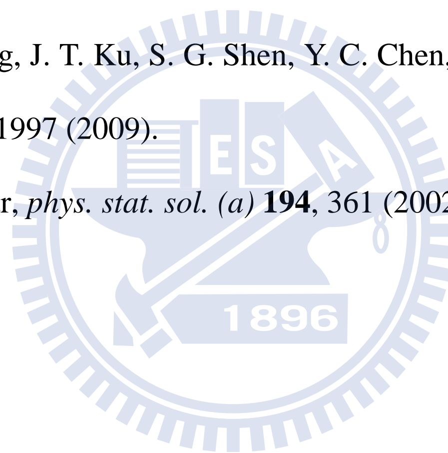

Publication list

Journal paper

[1] C. H. Chiu, **P. M. Tu**, S. P. Chang, C. C. Lin, C. Y. Jang, Z. Y. Li, H. C. Yang, H. W. Zan, H. C. Kuo, T. C. Lu, S. C. Wang, and C. Y. Chang, “Light Output Enhancement of GaN-Based Light-Emitting Diodes by Optimizing SiO2 Nanorod-Array Depth Patterned Sapphire Substrate,” *Jpn. J. Appl. Phys.* **51**, 04DG11 (2012).

[2] C. C. Chen, C. H. Chiu, **P. M. Tu**, M. Y. Kuo, M. H. Shih, J. K. Huang, H. C. Kuo, H. W. Zan, and C. Y. Chang, “Large Area of Ultraviolet GaN-Based Photonic Quasicrystal Laser,” *Jpn. J. Appl. Phys.* **51**, 04DG02 (2012).

[3] C. H. Chiu, C. C. Lin, **P. M. Tu**, S. C. Huang, C. C. Tu, J. C. Li, Z. Y. Li, W. Y. Uen, H. W. Zan, T. C. Lu, H. C. Kuo, S. C. Wang, and C. Y. Chang, “Improved Output Power of InGaN-Based Ultraviolet LEDs Using a Heavily Si-Doped GaN Insertion Layer Technique,” *IEEE J. Quantum Electron.* **48**, 175 (2012).

[4] **P. M. Tu**, C. Y. Chang, S. C. Huang, C. H. Chiu, J. R. Chang, W. T. Chang, D. S. Wuu, H. W. Zan, C. C. Lin, H. C. Kuo, and C. P. Hsu, “Investigation of efficiency droop for InGaN-Based UV Light-Emitting Diodes with InAlGaN Barrier,” *Appl. Phys. Lett.* **98**(21), 211107 (2011).

[5] T. C. Lu, T. T. Wu, S. W. Chen, **P. M. Tu**, Z. Y. Li, C. K. Chen, C. H. Chen, H. C. Kuo, S. C. Wang, H. W. Zan, and C. Y. Chang, “Characteristics of Current Injected GaN-Based Vertical-Cavity Surface-Emitting Lasers,” *IEEE J. Select. Topics Quantum Electron.* **17**, 1594 (2011). (*Invited Paper*)

[6] C. H. Chiu, **P. M. Tu**, C. C. Lin, D. W. Lin, Z. Y. Li, K. L. Chuang, J. R. Chang, T. C. Lu, H. W. Zan, C. Y. Chen, H. C. Kuo, S. C. Wang, and C. Y. Chang, “Highly Efficient and Bright LEDs Overgrown on GaN Nanopillar Substrates,” *IEEE J. Select. Topics Quantum Electron.* **17**, 971 (2011).

[7] B. S. Cheng, Y. L. Wu, T. C. Lu, C. H. Chiu, C. H. Chen, **P. M. Tu**, H. C. Kuo, S. C. Wang, and C. Y. Chang, "High Q microcavity light emitting diodes with buried AlN current apertures," *Appl. Phys. Lett.* **99**(4), 041101 (2011).

[8] T. C. Lu, S. W. Chen, T. T. Wu, **P. M. Tu**, C. K. Chen, C. H. Chen, Z. Y. Li, H. C. Kuo, and S. C. Wang, "Continuous wave operation of current injected GaN vertical cavity surface emitting lasers at room temperature," *Appl. Phys. Lett.* **97**(7), 071114 (2010).

[9] M. H. Lo, **P. M. Tu**, C. H. Wang, C. W. Hung, S. C. Hsu, Y. J. Cheng, H. C. Kuo, H. W. Zan, S. C. Wang, C. Y. Chang, and S. C. Huang, "High efficiency light emitting diode with anisotropically etched GaN-sapphire interface," *Appl. Phys. Lett.* **95**(4), 041109 (2009).

[10] M. H. Lo, **P. M. Tu**, C. H. Wang, Y. J. Cheng, C. W. Hung, S. C. Hsu, H. C. Kuo, H. W. Zan, S. C. Wang, C. Y. Chang, and C. M. Liu, "Defect selective passivation in GaN epitaxial growth and its application to light emitting diodes," *Appl. Phys. Lett.* **95**(21), 211103 (2009).

Conference paper

[1] **P. M. Tu**, J. R. Chang, S. C. Huang, S. K. Yang, Y. W. Lin, T. C. Hung, C. P. Hsu, and C. Y. Chang, "Investigation of efficiency droop for UV LED with N-type AlGaN layer," San Francisco California USA, *SPIE Photonics West 2012*, pp. 82781B-82781B-7.

[2] T. C. Hung, **P. M. Tu**, S. C. Huang, C. H. Shen, and C. P. Hsu, "Power enhancement of 380 nm UV-LED with hexagonal pyramid structures by AlN sacrificial layer," San Francisco California USA, *SPIE Photonics West 2012*, pp. 82780S-82780S-7.

[3] S. C. Huang, **P. M. Tu**, S. K. Yang, Y. W. Lin, and C. P. Hsu, "High performance 375 nm ultraviolet InGaN/AlGaN light-emitting diodes by using a heavily Si-doped GaN growth mode transition layer," San Francisco California USA, *SPIE Photonics West 2012*, pp.

826221-826221-7.

[4] C. H. Chiu, **P. M. Tu**, J. R. Chang, W. T. Chang, H. C. Kuo, and C. Y. Chang, “Reduction of efficiency droop in InGaN-based UV light-emitting diodes with InAlGaN barrier,” San Francisco California USA, *SPIE Photonics West 2012*, pp. 826222-826222-6.

[5] S. C. Huang, K. C. Shen, **P. M. Tu**, D. S. Wuu, H. C. Kuo, and R. H. Horng, “Improved performance of 375 nm InGaN/AlGaN light-emitting diodes by incorporating a heavily Si-doped transition layer,” San Francisco California USA, *SPIE Photonics West 2012* , pp. 82621L-82621L-7.

[6] Y. C. Chen, C. C. Tu, J. R. Chang, **P. M. Tu**, S. P. Chang, S. S. Yen, Y. C. Chen, H. C. Kuo and C. Y. Chang, “Investigation of Efficiency Droop for UV-LED with N-type AlGaN Layer,” *International Conference on Solid State Devices and Materials*, Nagoya, 2011, pp. 220-221.

[7] S. S. Yen, W. Y. Chen, J. R. Chang, S. P. Chang, **P. M. Tu**, Y. C. Hsu,Y. J. Li, Y. C. Chen, K. P. Sou, and C. Y. Chang, “A Novel Chemical Lift-Off Process based on Embedded Nano-rods Template,” *International Conference on Solid State Devices and Materials*, Nagoya, 2011, pp. 1401-1402.

[8] Y. L. Wu, B. S. Cheng, T. C. Lu, C. H. Chiu, C. H. Chen, **P. M. Tu**, H. C. Kuo, and S. C. Wang, “Optical Characteristics Improvement of High Q Microcavity Light Emitting Diodes with Buried AlN Current Blocking Apertures,” *2011 International Conference on Solid State Devices and Materials*, Nagoya, 2011, pp. 1143-1144.

[9] C. C. Chen, M. Y. Kuo, C. H. Chiu, **P. M. Tu**, M. H. Shih, S. P. Chang, J. K. Huang, H. C. Kuo, H. W. Zan, and C. Y. Chang, “Large Area of Ultraviolet GaN-based Photonic Quasicrystal Laser,” *2011 International Conference on Solid State Devices and Materials*, Nagoya, 2011, pp. 1141-1142.

[10] C. H. Chiu, **P. M. Tu**, C. Y. Chang, S. C. Huang, J. R. Chang, H. W. Zan, H. C. Kuo,

and C. P. Hsu, "Reduction of efficiency droop in InGaN-Based UV Light-Emitting Diodes with InAIGaN Barrier," *The 16th Opto-Electronics And Communications Conference, OECC 2011*, Kaohsiung, Taiwan, pp. 733-734.

[11] **P. M. Tu**, D. W. Lin, C. H. Chiu, C. C. Lin, Z. Y. Li, H. W. Han, K. L. Chuang, J. R. Chang, T. H. Yang, T.C. Lu, H.W. Zan, C. Y. Chao, H.C. Kuo, S.C. Wang, and C. Y. Chang, "Emission Efficiency Enhancement of GaN Light-emitting Diodes Grown on GaN Nano-pillar Template," *2010 Microoptics Conference*, MB3. (**Best Paper Award**)

[12] **P. M. Tu**, S. C. Hsu, M. H. Lo, H. W. Zan, H. C. Kuo, S. C. Wang, Y. J. Cheng, and C. Y. Chang, "GaN-based Vertical LEDs Fabrication by Mechanical Lift-off Technology," *2010 Microoptics Conference*,WP4.

[13] **P. M. Tu**, S. C. Hsu, M. H. Lo, H. W. Zan, H. C. Kuo, S. C. Wang, Y. J. Cheng, and C. Y. Chang, "High Quality Vertical LEDs Fabrication by Means of Mechanical Lift-off," *2010 International Conference on Solid State Devices and Materials*, Tokyo, 2010, pp. 405-406.

[14] K. L. Chuang, J. R. Chang, **P. M. Tu**, C. H. Chiu, Y. J. Li, H. W. Zan, H. C. Kuo, and C. Y. Chang, " An Investigation of GaN-Based LED with MBE Grown Nanopillars by MOCVD," *2010 International Conference on Solid State Devices and Materials*, Tokyo, 2010, pp. 403-404.

[15] K. L. Chuang, J. R. Chang, S. P. Chang, **P. M Tu**, Y. C. Hsu, W. T. Chen, H. W. Zan, T. C. Lu, H. C. Kuo, and C. Y. Chang, "Growth Mechanism of Nonpolar A-Plane GaN on Patterned M-Plane Sapphire," *2010 International Conference on Solid State Devices and Materials*, Tokyo, 2010, pp. 433-434.

[16] T. C. Lu, S. W. Chen, T. T. Wu, C. K. Chen, C. H. Chen, **P. M. Tu**, Z. Y. Li, H. C. Kuo, and S. C. Wang, "CW Current Injection of GaN-based Vertical Cavity Surface Emitting Laser with Hybrid Mirrors at Room Temperature," *Semiconductor Laser Conference*

*(ISLC), 2010 22nd IEEE Internationa*l, MB2, pp. 5-6.

Reports

[1] H. C Kuo, T. C. Lu, Z. Y. Li, T. T. Wu, **P. M. Tu**, C. H. Chiu, S. W. Chen, S. C. Wang, and C. Y. Chang, "Toward a high-performance, low-power microprojector with a surface-emitting blue laser," *SPIE Newsroom*, *DOI: 10.1117/2.1201205.004195*, 14 June (2012).

[2] **P. M. Tu** *et al.* "Quaternary barrier cuts droop in UV LEDs, *Compound Semiconductor, Volume 17 Number 5*, July (2011) pp. 37.

[3] **P. M. Tu** *et al.* "Investigation of efficiency droop for InGaN-based UV lightemitting diodes with InAlGaN barrier," *Physics Communications in Taiwan*, 11 Aug. (2011).

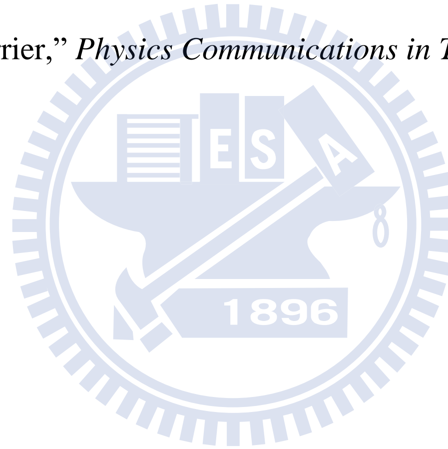

Vita

Po-Min Tu was born in Chiayi, Taiwan, on July 30, 1980. He received the B.S. degree in physics from Chung Yuan Christian University (CYCU), Chungli, Taiwan, and the M.S. degrees in physics from National Central University (NCU), Jhongli City, Taiwan, in 2002 and 2004, respectively. He is currently pursuing the Ph.D. degree with the Department of Photonics, Institute of Electro-Optical Engineering, National Chiao-Tung University (NCTU), Hsinchu, Taiwan.

In 2008, he joined the Eco-Electronics Research Group, NCTU, where he was engaged in research on III–V semiconductor materials by radio-frequency plasma-assisted molecular-beam epitaxy (RF-MBE) and metal organic chemical vapor deposition (MOCVD). His current research interests include GaN-based light emitting diodes (LEDs), vertical cavity surface emitting lasers (VCSELs), high electron mobility transistors (HEMTs), epitaxial growth of III–V materials, and optoelectronic devices.